Bethe-Salpeter Equation Approach for Calculations of X-ray Spectra

John Vinson

A dissertation
submitted in partial fulfillment of the
requirements for the degree of

Doctor of Philosophy

University of Washington

2012

Reading Committee:

John J. Rehr, Chair

Gerald T. Seidler

George F. Bertsch

Program Authorized to Offer Degree:
Physics

University of Washington

Abstract

Bethe-Salpeter Equation Approach for Calculations of X-ray Spectra

John Vinson

Chair of the Supervisory Committee:
Professor John J. Rehr
Physics

X-ray spectroscopy is a powerful and widely used tool for the investigation of the electronic structure of a large variety of solid-state materials, including crystals, liquids, amorphous solids, molecules, and extended states such as clusters or interfaces. The local nature of x-ray mediated electronic excitations, involving transitions to or from localized, atomic-like, core levels, makes them ideal probes of local electronic properties: bonding character, charge transfer, and local geometry. The interpretation of spectra relies on modeling the excitations accurately to provide a concrete connection between specific properties of a system and the resulting x-ray spectrum. As experimental techniques and facilities have improved, including third generation synchrotron sources and the advent of x-ray free-electron lasers, measurements have been taken on wider ranges of systems, exploring the effects of temperature and pressure, and at higher resolutions than before, but theoretical techniques have lagged. Our goal is to develop a first-principles theoretical framework capable of achieving quantitative agreement with x-ray absorption near-edge structure (XANES) experiments. This thesis aims to develop the Bethe-Salpeter equation (BSE), a particle-hole Green's function method, for describing the excited electronic state produced in core-level x-ray absorption and related spectroscopies. Building upon density functional theory along with self-energy corrections, our approach provides connection to experiment with minimal adjustable parameters, to both aid in interpretation and highlight unaccounted for physical processes. While a fully parameter-free method for calculating x-ray spectroscopy remains elusive, our method presented here allows for quantitative comparison to experiment without system-dependent fits. This method has been implemented in the OCEAN software package, and results are presented for both insulating and metallic materials, including *3d* transition metal and water systems.

TABLE OF CONTENTS

Page

List of Figures iii

List of Tables v

Glossary vi

Chapter 1: Introduction 1
1.1 Background 1
1.2 Goal of Dissertation 2
1.3 Conventions and Notation 3
1.4 X-ray spectroscopy: XAS, XES, and NIXS 3

Chapter 2: Quasi-Particle Theory 6
2.1 Density-Functional Theory 6
2.2 The use of pseudopotentials in DFT and the PAW formalism 8
2.3 Self-energy Corrections 10
2.4 The *GW* Approximation 12
2.5 The Many-Pole Self-Energy 13

Chapter 3: The Bethe-Salpeter Equation Approach 16
3.1 BSE and linear response 16
3.2 Considerations for core-level spectroscopy within a plane-wave basis 21
3.3 Direct 23
3.3.1 Core response 25
3.3.2 Short-range valence 26
3.3.3 Long-ranged valence 27
3.3.4 Convergence and approximations 28
3.4 Exchange 30
3.5 Spin-orbit 33
3.6 Inclusion of self-energy corrections 34

3.7 Limitations of our BSE approach . . . 35
3.8 Alternate approaches . . . 35

Chapter 4: Results: XANES of Selected Systems . . . 37
4.1 Introduction . . . 37
4.2 Salts: KCl, LiF, and MgO . . . 37
4.2.1 Introduction . . . 37
4.2.2 Results . . . 39
4.3 $L_{2,3}$ edges of *3d* transition metals . . . 43
4.3.1 Introduction . . . 43
4.3.2 Early transition metals . . . 44
4.3.3 Late transition metals . . . 51
4.4 Disordered systems: liquid and solid H_2O . . . 54
4.4.1 Introduction . . . 54
4.4.2 Ice Ih and VIII . . . 56
4.4.3 Liquid water . . . 59
4.5 Conclusions . . . 61

Chapter 5: Resonant Inelastic X-ray Scattering . . . 63
5.1 Theory . . . 63
5.2 Approach in OCEAN . . . 65
5.3 Excitonic effects and interference . . . 67
5.4 Diamond — C K edge . . . 69
5.5 CdS — S $L_{2,3}$ edge . . . 78
5.6 Conclusions . . . 80

Chapter 6: Conclusions . . . 81

Appendix A: OCEAN details . . . 83
A.1 OCEAN workflow . . . 83
A.2 Approximating the resolvent . . . 84
A.3 Sample Input . . . 86

Bibliography . . . 90

LIST OF FIGURES

Figure Number — Page

2.1 First order self-energy corrections to the one-electron Green's function 11

3.1 a) The two-particle Green's function G^2 in terms of the irreducible electron-hole interaction and b) the four-point irreducible electron-hole interaction I in our approximation 18
3.2 Second-order terms in the irreducible electron-hole interaction $I^{(2)}$ that are neglected by our approach 19
3.3 The convergence of the core-hole screening with respect to bands 28
3.4 The convergence of the core-hole screening with respect to radial cutoff 29

4.1 Fluorine K edge in LiF for both XAS and NIXS 38
4.2 The XAS K edges in KCl for both a) potassium and b) chlorine 40
4.3 The $L_{2,3}$-edge XANES of magnesium in MgO 42
4.4 $L_{2,3}$ edges of metallic Ca and Ca in CaF_2 46
4.5 Calculated XANES spectra for the Ti $L_{2,3}$-edge of $SrTiO_3$ 47
4.6 The $L_{2,3}$ edges of metallic V and M1 VO_2 51
4.7 The $L_{2,3}$ edge XAS of Fe, Co, and Ni metal 52
4.8 Calculations of the $L_{2,3}$ edge XAS of metallic Cu 53
4.9 The valence spectra of ice-Ih calculated using AI2NBSE 57
4.10 The calculated momentum-transfer dependence of the oxygen K edge for a) ice-Ih and b) ice-VIII 58
4.11 Valence spectra of liquid water 60
4.12 The XANES spectra for the O K edge in liquid water 61

5.1 The near-edge XES and XAS of the carbon K edge in diamond 70
5.2 RIXS of diamond compared with experiment 72
5.3 RIXS of diamond including incoherent contributions 73
5.4 Interacting RIXS map of the carbon K edge in diamond 74
5.5 Non-interacting RIXS map of the carbon K edge in diamond 75
5.6 The effect of interference between the two carbon site in the RIXS of diamond . . 77
5.7 The near-edge XES and XAS of the sulfur $L_{2,3}$ edge in CdS 78
5.8 RIXS map of the sulfur $L_{2,3}$ edge in CdS 79

A.1 Flowchart of the OCEAN package. 85

LIST OF TABLES

Table Number Page

4.1 Salts: Convergence Parameters 37
4.2 L3:L2 peak ratio vs. Z for selected *3d* transition metals 44
4.3 *3d* metals: Convergence Parameters 45
4.4 H_2O: Convergence Parameters 55

GLOSSARY

BSE: Bethe-Salpeter Equation

COHSEX: Coloumb Hole – Screened Exchange

DFT: Density Functional Theory

DOS: Density Of States

EXAFS: Extended X-ray Absorption Fine Structure

FSR: Final State Rule

GMRES: Generalized Minimal Residual method

LDA: Local Density Approximation

MD: Molecular Dynamics

MPSE: Many-Pole Self-Energy

NIXS: Non-resonant Inelastic X-ray Scattering

PAW: Projector Augmented Wave

RIXS: Resonant Inelastic X-ray Scattering

RPA: Random Phase Approximation

SCGW: Self-consistent *G*W

XANES: X-ray Absorption Near-Edge Spectroscopy

XAS: X-ray Absorption Spectroscopy

XES: X-ray Emission Spectroscopy

ACKNOWLEDGMENTS

I would like to thank Professor John J. Rehr for his guidance and instruction during the course of my doctorate. I am also indebted to Drs. Eric L. Shirley and David Prendergast and Professor Gerald T. Seidler, as well as my colleagues Fernando Vila, Josh Kas, Kevin Jorissen, Towfiq Ahmed, and Brian Mattern. I would also like to thank Alan Jamison, Raul Briceño, Liz Manrao, and Dan Benediktson.

DEDICATION

To my parents, Miriam and Tom

Chapter 1
INTRODUCTION

The overarching goal of theoretical physics is to create quantitative tools and a framework capable of describing the physical world. The guiding principles in this endeavor are accuracy and tractability, creating a theoretical framework that contains all the necessary complexity while at the same time making every reasonable approximation, every possible simplification.

1.1 Background

This thesis aims to model the electronic response of materials to x-ray photons, limited to the near-edge region within a few 10s to around 100 eV above the binding energy of a core-level electron. Our approach is based on the linear response of a condensed matter environment, either crystalline or disordered, with the photon field. The external perturbation of the incoming x-ray photon excites an electron from a core level in the atom up into the conduction bands where it forms a shortly-lived, bound excitonic state with the hole it left behind. In this energy region just above the threshold it has been found both empirically and theoretically that the excitation cross-section is highly sensitive to details of the chemical bonding and electronic structure of a material. X-ray spectroscopy then provides a useful tool for understanding the behavior of electrons in a condensed matter environment and for probing the structure and electronic properties of materials.

This thesis is concerned with x-ray spectroscopy of condensed matter systems. That is to say, we are looking at the response of materials to photons with energies between about 100-10000 eV. In this energy range, the primary response of a system will be from the core-level electrons absorbing enough energy from the photon to be excited up above the Fermi level. In general, the absorption as a function of energy will be decaying with energy with a series of sharp rises whose positions in energy are roughly constant for each element ($\pm$10 eV). These are referred to as the x-ray edges, and they correspond to the energy needed to excite a specific core level. The structure of the absorption after the edge can be divided in to two regions at

about 30 eV past the excitation; the near-edge and the extended fine structure. The extended fine structure is most readily understood as arising from interference effects of the photo-electron scattering off of neighboring atoms around the absorbing site, e.g., reference 1. Here we instead concern ourselves with the near-edge region which is more sensitive to local electronic structure.

1.2 Goal of Dissertation

In this thesis we will develop tools to implement the Bethe-Salpeter equation (BSE) approximation for calculating x-ray spectroscopy within the recently created OCEAN package (Obtaining Core-level Excitations using ABINIT and the NIST BSE solver) [2] . While there exists theoretical work on solving the Bethe-Salpeter equation in condensed matter systems [3–6], it has to date been primarily limited to exploration of valence-band UV or optical spectroscopies [7, 8]. The x-ray regime has been dominated by a variety of other approximations, such as the effective single-particle approximation [9, 10], time-dependent density functional theory (TDDFT) [11, 12], or model Hamiltonian-based solutions [13–15]. While these various approaches have had some success, quantitative agreement with experiment over a wide range of materials and core levels has remained elusive. Unique to our implementation is the inclusion of self-energy effects of the photo-electron, a reliable treatment of the screened core-hole potential, and the ability to treat hole-dependent broadening in spin-orbit split initial states. We find that our implementation of the BSE within OCEAN is in good agreement with experiment across a diverse variety of materials and provides a robust framework for near-edge x-ray spectroscopy calculations.

We will begin with a brief overview of the conventions and notations used in this work and touch on a few details of the interaction between photons and electrons. Then in chapter 2, we will present an overview of the theory necessary for calculating non-interacting single-particle wave functions to describe arbitrary condensed matter systems, which serve as basis functions for our treatment of the excited state. In chapter 3 we will cover the derivation and approximations of the BSE as well as further approximations made in our particular method of solving the BSE Hamiltonian. Results comparing the theoretical spectra to experiment will be discussed, covering a wide range of materials in chapter 4. Then, in chapter 5 an extension to our current approach for the calculation of resonant inelastic x-ray scattering will be outlined. Lastly, an outlook for future work, both theoretical and future implementation, will be given in chapter 6. The

appendix includes sections outlining the structure and running of OCEAN and a sample input.

1.3 Conventions and Notation

Throughout this dissertation Hartree atomic units will be used:

$$\hbar = 1,\ e = 1,\ m_e = 1,\ 4\pi\epsilon_0 = 1,\ c = \alpha^{-1} \approx 137. \tag{1.1}$$

Energies are measured in Hartree (equal to 2 Rydbergs or twice the binding energy of a 1*s* electron in hydrogen), and length is measured in Bohr (the average radius of the electron in hydrogen). Additionally second quantization will be used. In most chapters the second quantized operators will be assumed to be constructed from a basis of non-interacting single-particle wave functions determined via DFT. In this it should be assumed that $\hat{a}_i^\dagger\,(\hat{a}_i)$ creates (destroys) an electron above the Fermi level whose quantum numbers are labeled by the index i, or that conversely it destroys (creates) a hole below the Fermi level.

Throughout this work periodic boundary conditions will be assumed. This band structure approach means that the electrons are indexed by $i = n\mathbf{k}\sigma$ where the momentum $\mathbf{k}$ is limited to the first Brillouin zone, the spin σ is either up or down, and the band index n runs over all positive integers. At times the shorthand notation $(1) = (t, \mathbf{r}, \sigma)$ will be used to refer to the electrons' coordinates. The use of bold-face denotes 3-vectors, and, where it aids clarity, operators will have hats. Lastly, for diagrams, single, solid lines denote the non-interacting one-electron propagator, doubled lines the full propagator, saw-tooth the screened Coulomb interaction, dashed the unscreened Coulomb, and finally wiggly lines are photons.

1.4 X-ray spectroscopy: XAS, XES, and NIXS

In the non-relativistic regime we can write down the interaction between a photon and electron, following standard texts such as Gottfried and Yan [16], as

$$\begin{aligned} H_{\text{int}} &= \frac{1}{c}\left(\mathbf{p}_i \cdot \mathbf{A}(\mathbf{r}_i)\right) - \mu_i \cdot \mathbf{B}(\mathbf{r}_i) + \frac{1}{2c^2}|\mathbf{A}(\mathbf{r}_i)|^2 \\ &= H_1 + H_2\,, \end{aligned} \tag{1.2}$$

where H_2 contains only the $|\mathbf{A}|^2$ term. We have assumed the Coulomb gauge $\nabla \cdot \mathbf{A} = 0$, and $\mathbf{A}$ is the photon field operator acting at $\mathbf{r}_i$, the electron coordinate. The normalized photon field operators have the following forms:

$$\mathbf{A}(\mathbf{r},t) = \sum_{\mathbf{k}} \sqrt{\frac{\hbar c}{2Vk}} \left[e^{-i\omega t} e^{i\mathbf{k}\cdot\mathbf{r}} \hat{\mathbf{a}}_{\mathbf{k}} + \text{h.c.} \right]; \quad \mathbf{B} = \nabla \times \mathbf{A}; \quad \mathbf{E} = -\frac{1}{c}\frac{\partial \mathbf{A}}{\partial t}. \tag{1.3}$$

The interaction can be solved as a perturbative expansion of the system in the absence of electron-photon interactions, such that interactions of the form

$$H_{\text{int}} + H_{\text{int}} G_{el} H_{\text{int}} + \cdots \tag{1.4}$$

are also allowed. This expansion will be referred to as leading and second order in the interaction, respectively, though strict order of magnitude estimations show that the H_2 term enters in at the same order as the second-order H_1 contribution. At lowest order only the H_1 terms contribute to photon absorption or emission processes. X-ray absorption spectroscopy (XAS) and x-ray emission spectroscopy (XES) are complimentary techniques for measuring the unoccupied or occupied states of a system respectively. For x-ray absorption or emission the photon energy must be of the order of the binding energy of the core electron, i.e. the 1*s*,

$$\hbar c k = \hbar \omega \approx \frac{Z}{R}. \tag{1.5}$$

We then expand the exponential in the photon field operators in orders of $(\mathbf{k}\cdot\mathbf{r})$ where

$$\mathbf{k}\cdot\mathbf{r} \approx \frac{Z}{R\hbar c} R \approx \frac{Z}{137}. \tag{1.6}$$

For light nuclei this implies that the we can keep only the lowest order term, i.e., $e^{i\mathbf{k}\cdot\mathbf{r}} = 1 + \mathcal{O}[Z/137]$. This is referred to as the dipole limit or dipole approximation.

Grouping the H_1 term in powers of $(\mathbf{k}\cdot\mathbf{r})$ we can write the transition operator corresponding to either the absorption or emission of an x-ray as

$$D(\mathbf{q},\omega,\hat{\epsilon}) = \frac{1}{c}(\mathbf{p}_i \cdot \mathbf{A}(\mathbf{r}_i)) - \mu_i \cdot \mathbf{B}(\mathbf{r}_i) = E1 + M1 + \cdots. \tag{1.7}$$

The $E1$ term contains only the first-order $\mathbf{p}\cdot\mathbf{A}$ term since the coupling to magnetic field is of higher order in kr. This first order term is designated the electric dipole. The second order term is referred to as the magnetic dipole (M1) and contains both the first order of the magnetic moment term and the second order in $\mathbf{p}\cdot\mathbf{A}$. The E1 and M1 transitions share dipole selection rules for connecting angular momentum states; $|\Delta j| = 0, 1$ and $|\Delta m| = 0, 1$. They differ in that the magnetic moment is an axial vector and results in a parity flip. We consider both E1 and M1 terms in calculating x-ray absorption spectra.

Two-photon events require two photon field operators and enter in at first order in the interaction Hamiltonian via the $|\mathbf{A}|^2$ term in equation 1.2 and also in the second-order contributions from the H_1 terms. Experimentally these two contributions are easy to separate by tuning the x-ray beam. If the incident beam is near a core-level resonance contributions from the second-order H_1 terms lead to resonant inelastic x-ray scattering (RIXS) which will be discussed further in chapter 5. The $|\mathbf{A}|^2$ term determines what we call either non-resonant inelastic x-ray scattering (NIXS or NRIXS) or sometimes x-ray Raman scattering. The combination of two photon field operators results in an electron matrix element

$$H_{\text{int}} = (\hat{\epsilon}_i \cdot \hat{\epsilon}_f) e^{i\mathbf{q}\cdot\mathbf{r}} = \hat{\epsilon}_i \cdot \hat{\epsilon}_f \left[1 + i\mathbf{q}\cdot\mathbf{r} + \mathcal{O}[(qr)^2]\right], \tag{1.8}$$

where $\mathbf{q}$ is the momentum transfer from the incoming to outgoing photon. For small q this obeys the same selection rules as the E1, but for larger momentum transfers allows higher order transitions. Additionally, the energy transferred from the incoming photon can be decoupled from the momentum transfer, allowing an experimental probe that is not bound by the usual linear photon dispersion $E = \hbar c k$. Since the photon polarization vectors are only important relative to each other, the polarization dependence can be neglected in our calculations. For both XAS and NIXS the theoretical approach is the same, with only the form of the transition operator changing.

Chapter 2
QUASI-PARTICLE THEORY

In calculating the electronic response of (periodic) condensed matter systems we are interested in solving problems involving up to several hundred electrons. In deference to both accounting and tractability it is convenient to adopt a framework of quasi-particles. Excitations take the form of quasi-electrons or quasi-holes. These quasi-particles couple to the rest of the system, giving them a finite lifetime and screening interactions between quasi-particles. The problem is easily stated; in an interacting system no excitation can happen in isolation but instead is affected by the rest of the system. The solution is then to treat these many-body effects as perturbations of excitations of the non-interacting system.

2.1 Density-Functional Theory

Originated by Hohenberg and Kohn [17] and later extended by Kohn and Sham [18], density-functional theory (DFT) is one of the most successful computational tools in condensed matter and serves as a starting point for other, more involved theoretical approaches. As the name implies, DFT entails remapping the ground-state properties of a system onto functionals of the density alone. Kohn and Sham showed that, in principle, the ground-state density of a fictional system of non-interacting fermions with a proper, fictitious, density-dependent potential V_{xc} will exactly match that of the true, interacting system. This allows a Hamiltonian of the form

$$H = V_{\text{ext}} + \sum_i -\frac{1}{2}\nabla_i^2 + \int d\mathbf{r}' \frac{n(\mathbf{r}')}{|\mathbf{r}_i - \mathbf{r}'|} + V_{xc}[n]. \tag{2.1}$$

Since we are interested in the behavior of an electronic system in a condensed matter environment, the external potential contains the contributions from the ions which are treated as fixed, classical potentials. The next two terms are both the single particle analogues of expected many-body terms, a kinetic term and a modified Coulomb term known as the Hartree potential. The last term V_{xc} is known as the exchange-correlation potential. The exchange interaction arises

from the true Coulomb interaction, but is neglected in making the Hartree approximation. The correlation label arises from considering interactions as a perturbation to a non-interacting electron gas. While the non-interacting wave functions have a planewave form $e^{i\mathbf{q}\cdot\mathbf{r}}$ and hence no statistical correlation, the repulsion between the electrons will favor modified wave functions that maximize their distances from each other. The energy difference gained by including this effect is then called the correlation energy [19].

The exchange-correlation term V_{xc} contains both a correction to account for using the non-interacting kinetic term and the missing exchange and correlation. The exchange-correlation potential can be defined from the exchange-correlation energy,

$$V_{xc}[n] = \frac{\partial E_{xc}[n]}{\partial n}. \tag{2.2}$$

While an exact functional is not known, remarkably, approximate functionals have had excellent success for condensed matter systems. The most popular is the local density approximation (LDA) [20, 21], which utilizes the exchange and correlation energies from the free electron gas. That is to say, the exchange-correlation energy is fit to numerical calculations of the free-electron gas a varying densities n. The LDA has strong advantages over other formulations of the functional; it is free of system-dependent fitting parameters and is extremely efficient, depending only on the local density. A higher-order, but still *ab initio* density functional is the generalized gradient approximation (GGA) which depends on both the local density and its gradient [22–25].

DFT calculations are performed by self-consistently iterating the density. A trial density is created and from that the DFT Hamiltonian (eqn. 2.1). The eigenfunctions and energies of this Hamiltonian are then solved for, and the N orbitals with the lowest energies define the new ground-state density. When some ground state property (such as the total energy) is appropriately converged from one iteration to the next the calculation is complete. Since solving for the density requires diagonalizing the DFT Hamiltonian this method is formally $\mathcal{O}[N^3]$, limiting the applicability of DFT to smaller systems, but the search for approximations to bring the asymptotic scaling down is an ongoing area of research [26].

The success of density-functional theory is responsible for the abundance of *ab initio* ground-state calculations based on it. The LDA has proven to be a reliable approximation for calculating

properties such as lattice constants and bulk moduli, though excited state phenomena such as optical band gaps or photoemission spectra are not well reproduced. This is partly a failure of the approximations necessary for calculating within DFT and partly due to the fact that DFT is not a suitable method for looking at excitations such as the $N+(-)1$ system of (inverse) photoemission or the the excitonic excitations of optical absorption. A more appropriate method is based on the inclusion of the electron self-energy as outlined in section 2.3. There are a number of available codes used for DFT calculations; The ABINIT program [27–29] is used in this work.

2.2 The use of pseudopotentials in DFT and the PAW formalism

A common approximation made in DFT calculations is the use of pseudopotentials. The electrons in a system are partitioned into two classes based on energy: core and valence. The core levels are assumed to be deep enough that they are completely unaffected by the condensed environment such as the chemical bonding. E.g., the 1*s* is a core level of every atom starting with the second row. The core-level electrons are therefore frozen out of the calculation by adopting a pseudopotential V^{ps} that replaces the all-electron, ionic potential in the DFT Hamiltonian. In what follows the superscript *ps* will refer to quantities tied to the pseudopotential, and, correspondingly, *ae* will refer to those quantities in the all-electron system. Furthermore, the core electrons are neglected entirely in the subsequent DFT calculation. To make this concrete, consider the salt LiF with a two-atom unit cell. An all-electron calculation would involve twelve electrons while the pseudopotential-based calculation only involves eight. For a plane wave code, including core-level electrons and all-electron potentials requires a large number of plane waves. The use of pseudopotentials allows for a significant reduction in computational cost.

For ground-state properties and optical/UV spectroscopy calculations, the use of pseudopotentials is straightforward and well established, though evaluation of commutators with the Hamiltonian must explicitly account for any non-locality of the pseudopotentials used, e.g., Ref. 7. Extensive work has been done on optimizing psuedopotentials for transferability between different chemical environments and maximizing smoothness for efficient calculations [30–33]. In this work, psuedopotentials for all elements with *d*-type valence states include the same shell *s* and *p* states as valence as well. The inclusion of such semi-core states has been seen to improve the fidelity of the pseudopotentials, especially for states above the Fermi level [34]. The OPIUM

code has been used in this work to generate appropriate pseudopotentials [35].

Generically, pseudopotentials are constructed such that outside of some critical radius r_c, the psuedo and all-electron wave functions will be the same. Inside this radius however, they will differ dramatically as the all-electron wave functions will have nodes and be orthogonal to the core-level wave functions. In this work we are interested in transitions from, and interactions with, the core-level electrons, and we therefore require a method for transforming from pseudo- to all-electron wave functions. The projector augmented wave (PAW) formalism of Blöchl [36] defines a straightforward and accurate method for transforming between psuedo and all-electron wave functions. We will briefly summarize the method here.

The PAW method is used to transform an arbitrary wave function ψ_i^{ps} that is a solution to the psuedopotential-based DFT Hamiltonian with the corresponding all-electron wave function ψ_i^{ae}. As stated above, the pseudopotentials are constructed such that the wave functions only differ inside some sphere with radius r_c, and therefore a local basis is used to transform to the all-electron wave functions. The local basis consists of radial functions $\{R_{\nu l}\}$ and spherical harmonics Y_{lm}. The index ν allows multiple functions per principle angular quantum number l, and m is the standard azimuthal quantum number. Radial functions for both the all-electron and psuedopotential are determined by solving the radial Schödinger equation for the DFT Hamiltonian,

$$\left[-\frac{1}{2r^2}\frac{d}{dr}\left(r^2\frac{d}{dr}\right)+\frac{l(l+1)}{2r^2}+V_{\text{ion}}^{ps/ae}+V_{xc}[n^{ps/ae}(r)]\right]R_{\nu l}^{ps/ae}(r)=E_{\nu l}R_{\nu l}^{ps/ae}(r). \qquad (2.3)$$

The set of energies $\{E_{\nu l}\}$ are parameters that define the corresponding radial functions. The energies are chosen to ensure that the PAW basis is complete for the bands of interest. In practice this is done by stepping through a set of energies, solving the above radial equation, and adding an additional element ν to the basis when it can no longer adequately transform the psuedo to all-electron states. For the OCEAN code we are interested in states ranging from the occupied valence bands to several Hartree above the Fermi level, generally requiring between 4 and 8 basis functions per angular momentum state.

The above definition of the radial functions (eqn. 2.3) does not enforce orthogonality, and

hence it is necessary to define projectors for the radial functions:

$$\langle p_{\nu l} | R^{ps}_{\nu' l'} \rangle = \delta_{\nu,\nu'}. \tag{2.4}$$

We can then equate the all-electron and psuedo wave functions by taking the overlap between each projector and the psuedo wave function. This coefficient gives the amount of a particular psuedo character which must be subtracted off while the corresponding all-electron character is added on.

$$\phi^{ae}_i(\mathbf{r}) = \phi^{ps}_i(\mathbf{r}) + \sum_{\nu l m} \left[\left(R^{ae}_{\nu l}(x) Y_{lm}(\hat{x}) - R^{ps}_{\nu l}(x) Y_{lm}(\hat{x}) \right) \int_{r_c} d^3\mathbf{x}\; p_{\nu l}(x) Y_{lm}(\hat{x}) \phi^{ps}_i(\mathbf{x} + \tau_\alpha) \right], \tag{2.5}$$

where $x = \mathbf{r} - \tau_\alpha$, the position vector with respect to the site of the ion. The overlap integral is bounded by r_c, outside of which the psuedo and all-electron radial functions are, by design, indentical. In principle this should be done for every ion α in the unit cell, but for this work we are only interested in the all-electron wave functions centered at one site, i.e., the core site absorbing or scattering the x-ray, and so for notational simplicity this has been dropped.

Our use of pseudopotential DFT requires a separate calculation of the core-level wave functions. The pseudopotential approximation explicitly assumes that the core levels are unaffected by the chemical environment, and hence we can solve for an isolated atomic system. This is done using an atomic DFT code developed by Dr. Eric Shirley which incorporates relativistic corrections to the LDA to solve for the isolated atom [37, 38].

2.3 Self-energy Corrections

In the solid state it is convenient to adopt a quasi-particle picture of the system, and, treating the many-body states as perturbations of the non-interacting system, divide the many-body Hamiltonian into a single-particle and an interaction term:

$$H = H^0 + \Sigma. \tag{2.6}$$

Σ is the electron self-energy operator and contains information about all interactions between the electron and the rest of the electrons in the system, and H^0 is the non-interacting Hamiltonian,

$$H^0 = -\frac{1}{2}\nabla^2 + V_{\text{ext}} + \int d\mathbf{r}' \frac{n(\mathbf{r}')}{|\mathbf{r} - \mathbf{r}'|}, \tag{2.7}$$

which includes the kinetic energy, external potentials, and a Hartree term. Self-energy calculations are often carried out using the Kohn-Sham orbitals as a basis for the non-interacting Green's function. In such cases the contribution from the exchange-correlation potential V_{xc} are an approximation to the interactions and must be subtracted out. In general the self-energy will be non-local and non-Hermitian, and its imaginary component is identifiable with the finite lifetime of the quasi-particle.

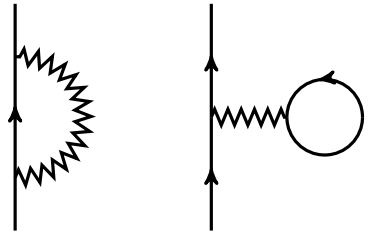

Figure 2.1: First order self-energy corrections to the one-electron Green's function

Contributions to the self-energy can be determined from diagrammatic analysis by expanding the Green's function to various orders in the Coulomb interaction. The first order corrections can be seen in figure 2.1. The self-energy can be simplified by considering only the proper self-energy, defined to be those self-energy diagrams that can not be separated by cutting a single G^0 line. Using the shorthand notation $(1) = (t_1, \mathbf{r}_1, \sigma_1)$, we can express the full Green's function as the solution to a Dyson's equation,

$$G(1,2) = G^0(1,2) + G^0(1,3)\,\Sigma(3,4)\,G(4,2), \tag{2.8}$$

which then includes all improper self-energy contributions.

Instead of explicitly enumerating high-order corrections to the proper self-energy, they can be accounted for by adopting a set of coupled equations, formulated by Hedin [39, 40]. We can

write down a set of equations for the self-energy involving the screened Coulomb operator W, a dressed vertex function Γ, and the polarization P:

$$\begin{aligned}
\Sigma(1,2) &= i\hbar \int d(3,4)\, G(1,4)\, W(1,3)\Gamma(4,2;3) \\
W(1,2) &= v(1,2) + \int d(3,4)\, W(1,3)\, P(3,4)\, v(4,2) \\
P(1,2) &= -i\hbar \int d(3,4)\, G(2,3)\, G(4,2+)\Gamma(3,4;1) \\
\Gamma(1,2;3) &= \delta(1,2)\,\delta(1,3) + \frac{\delta\Sigma(1,2)}{\delta V(3)}.
\end{aligned} \tag{2.9}$$

These four equations along with equation 2.8 are collectively known as the Hedin equations, and by starting from $G = G^0$ this system of equations can be iterated to any order.

2.4 *The GW Approximation*

An often-used simplification of Hedin's equations (eqns. 2.8 & 2.9) is to take only the zeroth order of the vertex function: $\Gamma(1,2;3) = \delta(1,2)\delta(1,3)$. The resulting approximation is referred to as the GW approximation due to the form of the self-energy $\Sigma = i\hbar\, GW$. Despite dropping from five to four coupled equations, calculations of the self-energy are computationally expensive and a variety of methods are adopted to reduce computational costs. Within a planewave-based code, the most straightforward approximation is to truncate the basis to some lower energy cutoff than the orbitals being used for G^0 and the ground-state density. The non-diagonal ($G \neq G'$) elements of the dielectric matrix $\epsilon_{GG'}$ (and hence the screened Coulomb attraction W) are referred to as the local fields. Their importance is directly related to inhomogenity of the system, i.e., the dependence of the screening on both coordinates $\mathbf{r}$ and $\mathbf{r}'$ and not merely the distance between them $|\mathbf{r} - \mathbf{r}'|$ [41]. While the dimension of $\epsilon_{GG'}$ is necessarily bounded by the wave functions' plane-wave cutoff, for many systems it can be much smaller without loss of accuracy.

In principle a full GW calculation would iterate both G and W until the results converge, but in practice one of two further approximations are often made. The first is the G^0W^0 approximation, also referred to as a single-shot self-energy. Here the Hedin equations are only evaluated once using the single-particle Green's function, and the screening is calculated within the random phase approximation (RPA), $P^0(1,2) = -i\hbar\, G^0(1,2)\, G^0(2,1)$. A second often used approximation

is G^0W, where the energies are updated self-consistently, re-evaluating the screening at each iteration based on the corrected energies. For both of these two approximations, the Kohn-Sham orbitals are assumed to be good approximations to the quasi-particle wave functions.

A large part of the cost of quasi-particle calculations comes from the convolution over energy and momentum in the definition of the self-energy. This requires the evaluation of the polarization or equivalently the inverse dielectric function at a range of energies and momenta. A simplification for this is the use of model dielectric functions such as the Lundqvist single-plasmon pole-model [42] ,

$$\epsilon(\mathbf{q},\omega) = 1 - \frac{\omega_{pl}^2}{\omega^2 - \omega^2(q)}. \tag{2.10}$$

Here $\omega_{pl} \equiv \sqrt{4\pi n_0}$ is the plasmon frequency defined by the average electron density n_0, and the momentum dependence is approximated by $\omega^2(q) \equiv 2E_F q^2/3 + q^4/4$, which depends on the Fermi energy E_F. In particular, this model only accounts for plasmon-like contributions to the polarization, neglecting particle-hole contributions. There are a variety of other models that can also be used [41, 43–45] some of which include an approximation to excitonic contributions and contributions from the off-diagonal local fields.

2.5 The Many-Pole Self-Energy

Even making a significant approximation for the screening, GW calculations of Σ remain expensive. For systems where a G^0W approximation is expected to be good, we use the many-pole self-energy (MPSE) of Kas *et al.* [46]. This method is an extension of the Lundqvist plasmon-pole model. In the MPSE a series of poles are used to represent the long-wavelength, $q = 0$ loss function $\epsilon^{-1}(\omega)$. The loss function can be calculated using the valence-band BSE code AI2NBSE [8], allowing for the inclusion of excitonic effects at the BSE level. The momentum dependence is included following the Lundqvist plasmon pole model (eqn. 2.10) which only depends on the magnitude of the momentum, reducing that integral to just one dimension. Additionally, the expression for the self-energy utilizes the electron-gas Green's function, making the calculation of the MPSE extremely fast once an appropriate loss function has been calculated.

Following Kas *et al.* we start from the definition of Σ within the GW approximation as a

convolution of G and W, and we replace G by its electron gas representation, giving

$$\Sigma(\mathbf{k},\omega) = i\int \frac{d^3\mathbf{q}}{(2\pi)^3}\int \frac{d\omega'}{2\pi}\frac{\epsilon^{-1}(\mathbf{q},\omega')}{|\mathbf{q}|^2}\frac{1}{\omega-\omega'-E_{\mathbf{k}-\mathbf{q}}+i\eta\, sgn(|\mathbf{k}-\mathbf{q}|-k_F)}. \tag{2.11}$$

For the homogenous electron gas the local fields are explicitly zero, allowing us to use a diagonal representation of the dielectric function ϵ. The cost is that this self-energy is a function of energy only and averaged over the whole system. Using the plasmon-pole form of the dielectric function from equation 2.10 the integral in equation 2.11 can be broken in to two terms [42], the first has no dependence on ω_{pl}^2 and can be evaluated analytically, giving the static Hartree-Fock exchange,

$$\Sigma_{\mathrm{HF}}(k) = -\frac{k}{\pi}\left[1+\frac{k_F^2-k^2}{2kk_F}\ln\left|\frac{k_F+k}{k_F-k}\right|\right]. \tag{2.12}$$

The second term is the dynamically screened exchange-correlation term, denoted by $\Sigma_d(\mathbf{k},\omega;\omega_{pl})$. The form of ϵ^{-1} with its single pole allows the integral over frequency to be performed analytically. Additionally, the dielectric and Green's functions only depend on the magnitude of the momentum, allowing the integral over solid angle to be performed analytically as well and leaving a single one-dimensional integral over momentum. Extending the single-pole model to a many-pole leads to re-expressing this dynamic self-energy in terms of a series of contributions,

$$\Sigma_d(k,\omega) = \sum_i g_i \Sigma_d(\mathbf{k},\omega;\omega_i), \tag{2.13}$$

with weights g_i and pole frequencies ω_i. As noted above, the determination of the weights and pole locations is determined by a calculation of the loss function and chosen to obey appropriate sum rules of the first and first-inverse moments of the loss function as outline in reference 46.

Since the MPSE is a G^0W method, its effects are limited to modifications of the DFT energies, and its use is only appropriate for systems where the DFT wave functions are a good approximation for the quasi-particle ones. For systems involving d-band electrons at the Fermi level, the LDA can break down, underestimating the on-site repulsion between these highly localized electrons, and therefore full GW calculations are necessary. The addition of the complex self-energy results in a generic stretch and dampening of the final spectra and is seen to improve agreement

with experiment. The inclusion of self-energy corrections will touched on briefly in section 3.6 while the implementation details of the OCEAN code will be covered in appendix A.

Chapter 3
THE BETHE-SALPETER EQUATION APPROACH

The Bethe-Salpeter equation governs the time evolution of an electron-hole pair, and it was originally formulated for the case of relativistic particles [47]. In a condensed matter system an excited electron and the hole it left behind, referred to collectively as an exciton, move through a sea of all the other electrons and a background of the much heavier ions. Commonly the ionic motion is treated as fully decoupled from that of the electrons, which is justified by the difference in time scales since the ions are several orders of magnitude heavier. The Bethe-Salpeter equation will be developed with respect to the one-electron Green's function, and the availability of a usable, one-electron Green's function will be assumed.

The wide-spread use of the Bethe-Salpeter equation to calculate linear response in condensed matter systems has been hampered by issues of poor scaling with system size. There has been significant success for some systems using computationally less demanding techniques such as effective one-electron codes, which treat the core hole as a fixed potential, or the adiabatic time-dependent local density approximation, in which the direct term is replaced by the LDA exchange-correlation. The reputation of the BSE as being too expensive comes somewhat from historical limitations in computational power and from realities of a valence-band, UV/optical code. For core-level spectroscopies the hole is well-localized in a small region of space, allowing approximations to be made that limit the scaling of the problem with systems size while maintaining accuracy. In the sections addressing the interaction terms that make up the BSE we will also comment on how such terms scale with increasing system size.

3.1 BSE and linear response

We learn about a system by probing or perturbing it. In the case of spectroscopy a photon is incident on the system carrying with it some energy and momentum which can be transferred to the system through absorption or scattering. The energy of the photon will determine the excitations available as well as their probabilities, and a certain amount of phenomenology is

useful in partitioning the calculation. For this work we will be considering the ions as completely fixed, and only look at the electronic response. The problem of electronic response is treated by standard texts on condensed matter field theory such as that by Fetter and Walecka [48].

The linear response of a system can be defined in terms of the dielectric function ϵ as

$$V_{tot}(\mathbf{r},\omega) = \int d^3\mathbf{r}'\, \epsilon^{-1}(\mathbf{r},\mathbf{r}',\omega)\, V_{ext}(\mathbf{r}',\omega). \tag{3.1}$$

The total potential arises both from the externally applied potential and from the response of the system itself. The dielectric response varies widely from system to system, and it is helpful to introduce the polarization operator P where

$$\epsilon(\mathbf{r},\mathbf{r}',\omega) = \delta(\mathbf{r},\mathbf{r}') + \int d^3\mathbf{r}''\, v(\mathbf{r},\mathbf{r}'')\, P(\mathbf{r}'',\mathbf{r}',\omega), \tag{3.2}$$

and v is the Coulomb potential. The polarizability operator by definition is a measure of how charge in a material adjusts to the presence of an external field. For metals at low frequencies the polarizability is strong and negative, and the electrons near the Fermi level have high mobility and move to counteract an applied field. The ground state consists of a completely filled Fermi sea, and hence the polarization is the result of electronic excitations. The simplest expression for the polarizability is the random phase approximation (RPA),

$$P(\mathbf{r},\mathbf{r}',\omega) = -i \int \frac{d\omega'}{2\pi} G^0(\mathbf{r},\mathbf{r}',\omega') G^0(\mathbf{r}',\mathbf{r},\omega-\omega') = \sum_{ij} (f_i - f_j) \frac{\psi_i(\mathbf{r})\psi_j^*(\mathbf{r})\psi_j(\mathbf{r}')\psi_i^*(\mathbf{r}')}{\omega - (E_j - E_i) + i\eta}, \tag{3.3}$$

where G^0 is the single-electron Green's functions. The terms f_i are Fermi factors (θ-functions at zero temperature), E_i are the single-electron energies, and ψ_i are the electron orbitals.

To relate the external potential to the total potential, we are interested in the inverse dielectric matrix, which can be expressed as

$$\epsilon^{-1}(\mathbf{r},\mathbf{r}',\omega) = \delta(\mathbf{r},\mathbf{r}') + \int d^3\mathbf{r}''\, v(\mathbf{r},\mathbf{r}'')\, \chi(\mathbf{r}'',\mathbf{r}',\omega), \tag{3.4}$$

where χ is the reducible polarizability or the density response function, which is in turn related

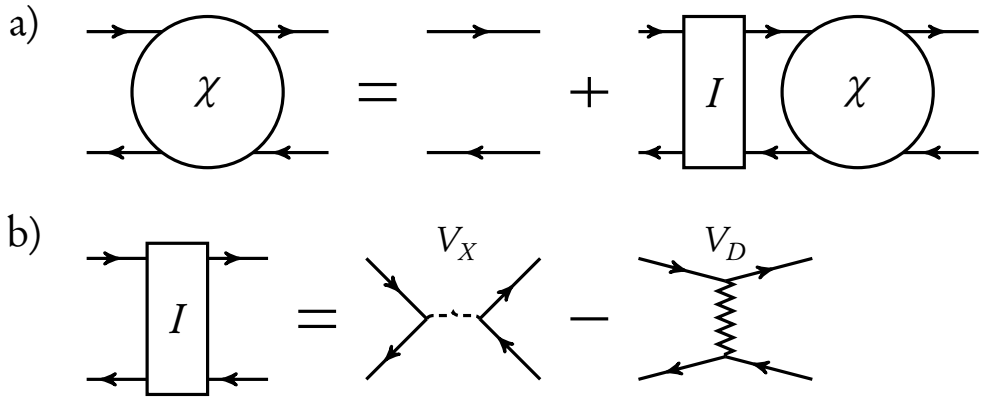

Figure 3.1: a) The two-particle Green's function G^2 in terms of the irreducible electron-hole interaction and b) the four-point irreducible electron-hole interaction I in our approximation.

to the two-particle Green's function,

$$\chi(1,2) = G_2(1,1';2,2') \equiv G_2^0(1,1';2,2') + G_2^0(1,1';3,3')\, I(3,3';4,4')\, G_2(4,4';2,2'), \tag{3.5}$$

where the non-interacting two-particle Green's function is the product of the non-interacting electron and hole propagators ($G_2^0(1,1';2,2') \equiv G^0(1',2')G^0(2,1)$), and I is the four-point irreducible electron-hole interaction. For our Bethe-Salpeter equation (BSE) formulation we will keep only the lowest-order interaction terms, the direct and the exchange, which correspond to setting

$$I(1,1';2,2') = \delta(1,1')\,\delta(2,2')\,v(1,2) - \delta(1,2)\,\delta(1',2')\,W(1,1'), \tag{3.6}$$

where W is the screened Coulomb term $W(1,2) \equiv \epsilon^{-1}(1,3)\,v(3,2)$. Diagrammatically this is shown in figure 3.1. This has the side effect of truncating the diagram expansion somewhat haphazardly, including some terms to all orders while dropping others, e.g., an infinite series of ladders are included. In the original paper by Bethe and Salpeter this is justified physically for weak coupling by arguing that the probability of two simultaneous interaction terms may be low, but the probability that a bound exciton with a long lifetime will interact several times subsequently is much larger [47]. Next order, neglected terms are illustrated in figure 3.2.

We start by considering the equation of motion of an electron-hole pair creation operator, i.e.,

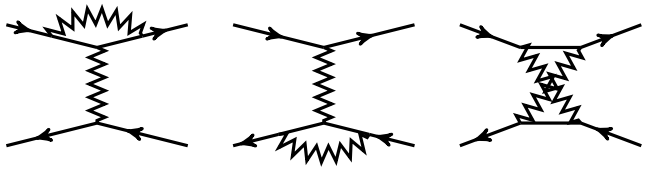

Figure 3.2: Second-order terms in the irreducible electron-hole interaction $I^{(2)}$ that are neglected by our approach.

a destruction operator acting on an occupied core or valence state and a creation operator acting on a conduction-band state. Using explicit states where $|\Psi_0\rangle$ is the many-body ground state with energy set to 0 and $|\Psi\rangle$ is an excited state with energy E, we can make the following statement:

$$\langle\Psi|\left[H,\hat{a}_i^\dagger\hat{a}_j\right]|\Psi_0\rangle = E\langle\Psi|\hat{a}_i^\dagger\hat{a}_j|\Psi_0\rangle. \tag{3.7}$$

Here H is the full many-body Hamiltonian and the subscripts $\{i,j\}$ contain the necessary quantum numbers to fully describe the set of single-electron states with i denoting a conduction state above the Fermi level and j a valence or core state below the Fermi level. In a band-structure formalism the set of states $\{i\}$ refers to $\{n\mathbf{k}\sigma\}$, where n is the band index, $\mathbf{k}$ is the crystal momentum, and σ labels the spin. We can see that we are only considering a singly excited state. That is to say, Ψ differs from the ground state by only one electron-hole pair. To make this approximation more explicit, we can say that our excited state wave function is defined by

$$|\Psi\rangle = \sum_{i,j} C_{ij}\hat{a}_i^\dagger\hat{a}_j|\Psi_0\rangle, \tag{3.8}$$

where $\left\{C_{ij}\right\}$ are the normalized coefficients, $|i,j\rangle = \hat{a}_i^\dagger\hat{a}_j|\Psi_0\rangle$ denotes a single electron-hole pair, and correspondingly our ground state is

$$|\Psi_0\rangle = \prod_j \hat{a}_j^\dagger|\text{vacuum}\rangle. \tag{3.9}$$

This is equivalent to saying that we are considering the ground state to be made up of a single Slater determinant. In section 3.7 the effects of this approximation will be expanded on. Equation

3.7 can be expanded to give,

$$\sum_{i,j} C_{ij} \left(E_i - E_j - E \right) = -\sum_{i',j'} \langle i, j | (V_X - V_D) | i', j' \rangle, \tag{3.10}$$

where E_i (E_j) are the single-particle energies of unoccupied (occupied) states. The two interaction terms both involve Coloumbic operators and are called the direct and exchange, where the exchange enters in with the opposite sign due to interchange of fermion propagators (see fig. 3.1).

We can write down the transition rate

$$\Gamma_O(\omega, \mathbf{q}) = 2\pi \sum_F |\langle I | \hat{O}(\omega, \mathbf{q}) | F \rangle|^2 \, \delta(\omega + E_I - E_F) \, \delta(\mathbf{q} + \mathbf{k}_I - \mathbf{k}_F), \tag{3.11}$$

where O is the many-body electron-photon interaction. By summing over all the possible excited states of the system the transition probability or cross section can be determined. The determination and summation over all final states is cumbersome, and in fact the same quantity can be determined without explicit final states. Instead, we exploit the completeness of the sum over all final states.

$$\begin{aligned} \Gamma_O(\omega, \mathbf{q}) &= 2\pi \sum_F \langle I | \hat{O}(\omega, \mathbf{q}) | F \rangle \langle F | \hat{O}^\dagger(\omega, \mathbf{q}) | I \rangle \, \delta(\omega + E_I - E_F) \, \delta(\mathbf{q} + \mathbf{k}_I - \mathbf{k}_F) \\ &= -\operatorname{\mathfrak{Im}} \left[\langle I | \hat{O}(\omega, \mathbf{q}) G_2(\omega, \mathbf{q}) \hat{O}^\dagger(\omega, \mathbf{q}) | I \rangle \right], \end{aligned} \tag{3.12}$$

where G_2 is the two-particle Green's function as defined by equations 3.5 and 3.6. We use this definition of G_2 to define our our effective BSE Hamiltonian,

$$\begin{aligned} G_2 &= \left[\omega - H_{\text{BSE}} \right]^{-1} \\ H_{\text{BSE}} &= H_e - H_h + V_X - V_D, \end{aligned} \tag{3.13}$$

where the H_e and H_h are the single-particle electron and hole Hamiltonians respectively. The direct and exchange terms, V_D and V_X, will be covered in sections 3.3 and 3.4. The hole Hamiltonian,

$$H_h = E_h - i\Gamma_j + \chi_j, \tag{3.14}$$

contains the hole binding energy E_h as well as the spin-orbit splitting χ and life-time broadening Γ which both depend on the total angular momentum state j. The inclusions of these two terms will be covered briefly in section 3.5. The electron Hamiltonian is built up of Kohn-Sham orbitals as discussed in chapter 2 and so includes all of the solid-state effects. H_e also includes self-energy effects either directly, through diagonalizing a DFT+GW Hamiltonian, or by adding a complex self-energy correction to the single-particle energies (see sec. 3.6).

3.2 Considerations for core-level spectroscopy within a plane-wave basis

The approach used in this thesis and the OCEAN package is dependent upon determining the ground-state wave functions from a band-structure, pseduopotential-based DFT code. The single-electron wave functions are written as

$$\phi_j^{ps} = \phi_{n\mathbf{k}\sigma}^{ps}(\mathbf{r}) = e^{i\mathbf{k}\cdot\mathbf{r}} \sum_{\mathbf{G}} C_{\mathbf{G}}^{n\mathbf{k}\sigma} e^{i\mathbf{G}\cdot\mathbf{r}}, \tag{3.15}$$

where $\mathbf{k}$ is restricted to be in the first Brillouin zone, $\mathbf{r}$ is restricted to the unit cell, and the set of vectors $\{\mathbf{G}\}$ are integer units of a reciprocal lattice vector. The *ps* superscript denotes that these wave functions are solutions to the Kohn-Sham equations in which the true (or all-electron) ionic potential V_{ion}^{ae} has been replaced with a pseudopotential V_{ion}^{ps}. The psuedopotential is designed to implicitly include core-level states, and it therefore has two main advantages over the true potential: it is less deep and the system has fewer electrons. The pseudo wave functions are solutions to a system that explicitly has no core-level electrons and so must be transformed to the corresponding all-electron wave functions before transitions from or interactions with the core hole are meaningful. The PAW prescription of Blöchl is suitable for such a transformation and is summarized in section 2.2.

Specifically looking at absorption, the transition operator is $e^{i\mathbf{q}\cdot\mathbf{r}}\,\hat{e}\cdot\mathbf{r}$. Within our singly-excited-state approximation the many-body transition can be simplified as a single-particle transition from the core level to a conduction-band state. Following the work of Shirley [38] and dropping spin indices, the transition matrix element connecting the ground state to a singly ex-

cited state can be written as,

$$\langle \alpha, n\mathbf{k}; \mathbf{q} | e^{i\mathbf{q}\cdot\mathbf{r}} \hat{e}\cdot(\mathbf{r}-\tau_\alpha)|0\rangle = N^{-1/2}\sum_{\mathbf{R}}^{N} e^{i\mathbf{k}\cdot\mathbf{R}} \langle \phi_{n\mathbf{k}+\mathbf{q}} | e^{i\mathbf{q}\cdot\mathbf{r}} \hat{e}\cdot(\mathbf{r}-\tau_\alpha)|\phi_{\alpha,\mathbf{R}}\rangle, \tag{3.16}$$

where the sum over $\{\mathbf{R}\}$ reflects the transitions from core-hole sites in every unit cell. Within a given cell the core-hole site is centered at τ_α. The sum over every site is constructed to conserve crystal momentum with the absorption of a photon of momentum $\mathbf{q}$ only resulting in transitions from a core-hole Bloch state of momentum $\mathbf{k}$ to a conduction-band state of momentum $\mathbf{k}+\mathbf{q}$. The single-particle matrix element can then be rewritten:

$$\langle \phi_{n\mathbf{k}+\mathbf{q}} | e^{i\mathbf{q}\cdot\mathbf{r}} \hat{e}\cdot(\mathbf{r}-\tau_\alpha)|\phi_{\alpha,\mathbf{R}}\rangle = e^{-i\mathbf{k}\cdot\mathbf{R}} \langle \phi_{n\mathbf{k}+\mathbf{q}} | e^{i\mathbf{q}\cdot\mathbf{r}} \hat{e}\cdot(\mathbf{r}-\tau_\alpha)|\phi_{\alpha,\mathbf{R}=0}\rangle. \tag{3.17}$$

Then, shifting the coordinate system $\mathbf{r} = \mathbf{r} - \tau_\alpha$ and changing from bra-ket notation to explicit wave functions, the transition matrix element becomes

$$e^{-i\mathbf{k}\cdot\mathbf{R}} \int d^3\mathbf{r}\, \phi^*_{n\mathbf{k}+\mathbf{q}}(\mathbf{r}+\tau_\alpha)\, e^{i\mathbf{q}\cdot(\mathbf{r}+\tau_\alpha)} (\hat{e}\cdot\mathbf{r})\, \phi_{\alpha\mathbf{R}=0}(\mathbf{r}+\tau_\alpha). \tag{3.18}$$

To evaluate this integral it is convenient to consider the projection of the valence and conduction states onto a localized basis,

$$\phi_{n\mathbf{k}+\mathbf{q}}(\mathbf{r}+\tau_\alpha) = e^{i(\mathbf{k}+\mathbf{q})\cdot(\mathbf{r}+\tau_\alpha)} \sum_{\mathbf{G}} C^{n\mathbf{k}+\mathbf{q}}_{\mathbf{G}} e^{i\mathbf{G}\cdot(\mathbf{r}+\tau_\alpha)} \approx \sum_{\nu lm} A^{n\mathbf{k}}_{\nu lm} R_{\nu l}(r) Y_{lm}(\hat{r}), \tag{3.19}$$

for $r < r_c$, some cutoff radius within which the localized basis is defined. This cutoff is justifiable so long as the core wave function is suitably localized within it. From this we can see that the expansion coefficient A is defined by

$$\begin{aligned} A^{n\mathbf{k}+\mathbf{q}}_{\nu lm} &= \sum_{\mathbf{G}} \int_{|x|<r_c} d^3\mathbf{x}\, e^{i\mathbf{k}\cdot(\mathbf{x}+\tau_\alpha)} C^{n\mathbf{k}\sigma}_{\mathbf{G}} e^{i\mathbf{G}\cdot(\mathbf{x}+\tau_\alpha)} R_{\nu l}(x) Y_{lm}(\hat{x}) \\ &= 4\pi i^l \sum_{\mathbf{G}} C^{n\mathbf{k}\sigma}_{\mathbf{G}} e^{i(\mathbf{G}+\mathbf{k}+\mathbf{q})\cdot\tau_\alpha} Y^*_{lm}(\mathbf{G}+\hat{\mathbf{k}}+\mathbf{q}) \int_0^{r_c} dr\, r^2 j_l(|\mathbf{G}+\mathbf{k}+\mathbf{q}|r) R_{\nu l}(r). \end{aligned} \tag{3.20}$$

With this we can easily move between an excitonic wave function expressed as occupations of

extended, Kohn-Sham planewave states and occupations of the localized basis. It is also useful to define the core wave function as the product of a radial and angular contribution,

$$\phi_{\alpha\mathbf{R}=0}(\mathbf{r}+\tau_\alpha) = R_\alpha(r)Y_{LM}(\hat{r}), \tag{3.21}$$

where L and M refer to the principle and azimuthal angular momentum quantum numbers of the core level, and non-zero values of $\mathbf{R}$ would necessitate shifts in the position vector $\mathbf{r}$.

To this point the radial functions have been an arbitrary, but complete set. By choosing these radial functions to be those prescribed by the PAW formalism we are able to consider transitions from the core levels to the corresponding valence or conduction bands of our pseudized system (sec. 2.2). Lastly, the matrix elements in equations 3.16-8 can be written as

$$e^{i\mathbf{q}\cdot\tau_\alpha}\sum_{\nu lm}(A^{n\mathbf{k}+\mathbf{q}}_{\nu lm})^*\int d^3\mathbf{r}\, R^{ae}_{\nu l}(r)Y^*_{lm}(\hat{r})\,e^{i\mathbf{q}\cdot\mathbf{r}}(\hat{e}\cdot\mathbf{r})R_\alpha(r)Y_{LM}(\hat{r}). \tag{3.22}$$

The interaction terms, V_X and V_D, in the BSE Hamiltonian are divided into short and long-range parts with the short-range parts evaluated using this same localized basis.

3.3 Direct

The direct interaction is the screened Coulomb scattering between the excited electron and hole

$$V_D = \hat{a}^\dagger_c(\mathbf{r},\sigma)\hat{a}_b(\mathbf{r}',\sigma')\,W(\mathbf{r},\mathbf{r}',\omega)\hat{a}_c(\mathbf{r},\sigma)\hat{a}^\dagger_b(\mathbf{r}',\sigma'). \tag{3.23}$$

The screening of this interaction is determined by the dielectric response of the system,

$$W(\mathbf{r},\mathbf{r}',\omega) = \int d^3\mathbf{r}''\,\frac{\epsilon^{-1}(\mathbf{r},\mathbf{r}'',\omega)}{|\mathbf{r}''-\mathbf{r}'|}. \tag{3.24}$$

The dielectric response ϵ^{-1} is related to the polarizability χ which can itself be determined by the irreducible polarizability χ^0 according to

$$\begin{aligned}\epsilon^{-1} &= 1+v\chi \\ \chi &= (1-\chi^0 v)^{-1}\chi^0,\end{aligned} \tag{3.25}$$

where v is the bare Coulomb interaction. For this work we will adopt several approximations in the determination of the screening. In this section we will outline the approach used in the OCEAN package, and then at the end we will address the limitations and likely sources of error from the approximations made. In OCEAN we adopt a hybrid approach in calculating the core-hole screening, using both a direct calculation of the dielectric function and a model function which is parameterized by two properties of the system being studied: the average electron density and macroscopic dielectric constant ϵ_∞ [3]. The response is divided in to three regimes: core, short-ranged valence, and long-ranged valence.

We only consider spherically symmetric screening, that is to say the calculated screened potential is a function only of the radius from the core hole which allows our calculation of χ to be carried out at fewer points. The higher-order multipole terms are not neglected entirely, but because they are much shorter range (around the core-hole density) the screening response of the valence electrons is assumed to be slight. This is to say we make the following approximation,

$$\begin{aligned} W(\mathbf{r},\omega) &= \int d^3\mathbf{r}' \rho_c(\mathbf{r}') \int d^3\mathbf{r}'' \, \epsilon^{-1}(\mathbf{r},\mathbf{r}'',\omega) \sum_{l=0}^{\infty} P_l(\hat{r}'\cdot\hat{r}'') \left[\frac{r_<^l}{r_>^{l+1}} \right]_{\mathbf{r}'',\mathbf{r}'} \\ &\approx \int d^3\mathbf{r}' \rho_c(\mathbf{r}') \int d^3\mathbf{r}'' \left[\frac{\epsilon^{-1}(\mathbf{r},\mathbf{r}'',\omega)}{(r_>)_{\mathbf{r}'',\mathbf{r}'}} + \sum_{l=1}^{\infty} P_l(\hat{r}'\cdot\hat{r}'') \left[\frac{r_<^l}{r_>^{l+1}} \right]_{\mathbf{r}'',\mathbf{r}'} \right] \\ &\approx W_0 + \sum_{l=1}^{\infty} W_l, \end{aligned} \tag{3.26}$$

where all higher-order multipole terms are unscreened. Instead they are scaled by the same factor as the exchange term (sec. 3.4) to account for neglected multi-configurations in the atomic calculation.

The first approximation we make in the calculation of W_0 is to consider only the static response. By integrating against the core-hole density we can express the direct term (eqn. 3.23) as a function of only the photo-electron coordinate. We can then write the screened Coulomb operator as the sum of the core potential, and short and long-ranged valence response:

$$W_0(r) = \Delta V_c(r) + W_v^{(1)}(r) + W_v^{(2)}(r). \tag{3.27}$$

At distances larger than 10 a.u. we make a further approximation that the dielectric response is equal to the macroscopic response, i.e., $\epsilon(\mathbf{r},\mathbf{r}') = \epsilon_\infty$. We then replace equation 3.27 with

$$W_0(r > 10) = \epsilon_\infty^{-1}/r\,. \tag{3.28}$$

The physical argument for the division of the valence response comes from the screening behavior of condensed matter systems. The core hole has a total charge $+e$ which at very long range r should give a potential that goes as $e/\epsilon_\infty r$. This is due to the polarizability of the electronic system, and for metals leads to a very short-ranged potential. We have the freedom to break the core-screened core-hole potential in to two parts. The short-ranged part is given by

$$V^{(1)}(r) = \Delta V_c(r) - \Theta(R-r)/R - \Theta(r-R)/r, \tag{3.29}$$

where Θ is the Heavyside step function, and the long-ranged is correspondingly

$$V^{(2)}(r) = \Theta(R-r)/R + \Theta(r-R)/r. \tag{3.30}$$

This is to say we have added a neutralizing shell of charge $-e$ to the short-ranged potential at radius R while adding the oppositely charged shell to the long-ranged potential. The advantage is that now the valence response to V_1 is also short-ranged, while the response to V_2 can be treated using a dielectric model. Obviously in the limit that $R \to \infty$ this entails no approximation.

3.3.1 Core response

First, as may be expected with our psuedopotential-based methodology, we divide the screening response in to core and valence. A core-hole pseudopotential is constructed by removing an electron from the core level of interest and relaxing the other $N-1$ electrons in the atom. The core response is calculated by determining the difference between the potential of the standard ion and the $N-1$ version. This gives the fully-relaxed, core-only, screened core hole which we can denote by ΔV_c. Next we calculate the response of the valence electrons to this core-screened potential. This is done neglecting the contributions of the core electrons.

3.3.2 Short-range valence

The short-range, valence dielectric response is calculated within the random phase approximation (RPA) [49, 50]. This is determined by approximating the polarization χ from the RPA irreducible polarizability,

$$\chi^0(\mathbf{r},\mathbf{r}'\omega) = \int d\omega'\, G^0(\mathbf{r},\mathbf{r}',\omega')\, G^0(\mathbf{r}',\mathbf{r},\omega+\omega'), \tag{3.31}$$

where G^0 here is the single-particle, non-interacting Green's function which can be expressed as

$$G^0(\mathbf{r},\mathbf{r}',\omega) = \sum_i \frac{\psi_i^*(\mathbf{r})\psi_i(\mathbf{r}')}{\omega - E_i + i\eta\, sgn(E_i - E_F)}. \tag{3.32}$$

The evaluation of G^0 relies on explicit sums over the Kohn-Sham states, thereby neglecting the already accounted for core response. Limiting ourselves to the static approximation and assuming that the system obeys time-reversibility (this precludes magnetic systems), we can make the simplification that

$$G^0(\mathbf{r},\mathbf{r}',\omega) = G^0(\mathbf{r}',\mathbf{r},\omega), \tag{3.33}$$

and hence that

$$\chi^0(\mathbf{r},\mathbf{r}',\omega=0) = \int d\omega' \left[G^0(\mathbf{r},\mathbf{r}',\omega')\right]^2. \tag{3.34}$$

The integration can be then extended to the complex plane and shifted from along the real axis to along the imaginary axis. This is advantageous because it allows us to avoid the poles of the Green's functions along the real axis at the energies of the single-electron states. The integral along imaginary frequencies in fact converges quickly and only requires evaluation at a few points.

To fully avoid any poles we center the integral along the Fermi level E_F giving a final expression for the RPA irreducible polarizability

$$\chi^0(\mathbf{r},\mathbf{r}',\omega=0) = \int dt \left[G^0(\mathbf{r},\mathbf{r}',E_F+it)\right]^2. \tag{3.35}$$

A finite smearing term is applied to metallic systems to avoid the divergence from having states at the Fermi level. For systems lacking time-reversal symmetry (ferromagnetic or anti-ferromagnetic) the approximation made in equation 3.33 is not valid. Instead the Green's function must be sep-

arately calculated at each $\{\mathbf{r},\mathbf{r}'\}$. The result is a factor of 2 increase in computational time; both are coded within OCEAN allowing a speed-up for non-magnetic systems.

The short-range RPA response is calculated within a sphere centered around the atomic site. The grid of points $\{\mathbf{r},\mathbf{r}'\}$ was determined using 32 Gauss-Legendre points for the radial points and, for each, a 36-point angular coordinate set [51]. Following equation 3.26 we can obtain the short-ranged dielectric response $\epsilon^{(1)}$. This is then used to screen the short-ranged potential given in equation 3.29 yielding the short-ranged screened Coulomb potential

$$W_v^{(1)}(r) = \int d^3\mathbf{r}' \frac{1}{\epsilon^{(1)}(\mathbf{r},\mathbf{r}')} V^{(1)}(r'). \tag{3.36}$$

3.3.3 Long-ranged valence

The screening of the long-ranged potential $V^{(2)}$ is determined using an extension to the Levine-Louie model dielectric function [52]. Following the prescription of Shirley *et al.* [3, 53] we add in dependence on inhomogeneities by approximating the reducible polarizability using the model function

$$\chi_M(\mathbf{r},\mathbf{r}') = \nabla\cdot\nabla' \left(\frac{n(\mathbf{r})+n(\mathbf{r}')}{2n_0}\right)\left(\int \frac{d^3\mathbf{q}}{(2\pi^3} e^{i\mathbf{q}\cdot(\mathbf{r}-\mathbf{r}')} \frac{\epsilon_{\mathrm{LL}}^{-1}(q,n_0;\epsilon_\infty)-1}{4\pi}\right), \tag{3.37}$$

where the $\epsilon_{\mathrm{LL}}^{-1}$ is the Levine-Louie dielectric function which depends on both the average electron density and the macroscopic dielectric constant. The original formulation of Levine and Louie was in terms of the band gap, but within the model the band gap has a definite relation to ϵ_∞. The value of ϵ_∞ is usually take from experiment, though it can be calculated using the valence BSE package AI2NBSE or approximated by picking a reasonable value based on the band gap of the system. This is not entirely cavalier since the crossover radius between calculated and model dielectric must be chosen so that the calculated response begins to already resemble the less exact model response. We can then evaluate the spherically symmetric response to the long-ranged potential,

$$W_v^{(2)}(r) = \int d^3\mathbf{r}' \int d^3\mathbf{r}'' v(\mathbf{r}',r) v(\mathbf{r}'',R) \chi_M(\mathbf{r}',\mathbf{r}''). \tag{3.38}$$

This is combined with the earlier results to give the full, screened Coulomb interaction $W_0(r)$. With its long-range tail, the calculation of W_0 presents a problem for scaling to large systems. However, it can be expected that the excited electron will be reasonably localized around the core hole. In the future an approximation based on this assumption for use with large unit cells may be necessary, and the success of finite-cluster [54] or super-cell techniques [10] suggests that such a real-space cutoff will be feasible.

3.3.4 Convergence and approximations

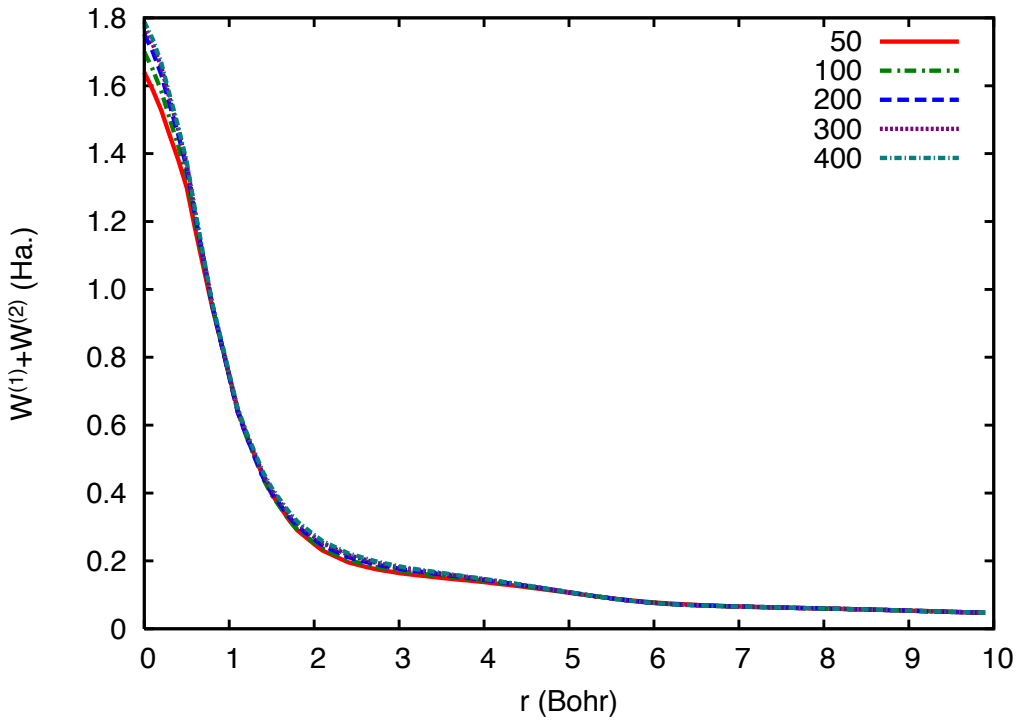

Figure 3.3: The convergence of the core-hole screening with respect to the number of bands. This example is showing the screening of a F 1*s* hole in LiF, and at around 300 bands the calculation can be considered well converged. The number of bands included in a calculation corresponds to including wave functions up to some energy above the Fermi level in the Green's function (eqn. 3.32).

In principle, the spectral representation of the Green's function involves a sum over all unoccupied states, which must then be truncated at some finite band index. In practice, the calculation

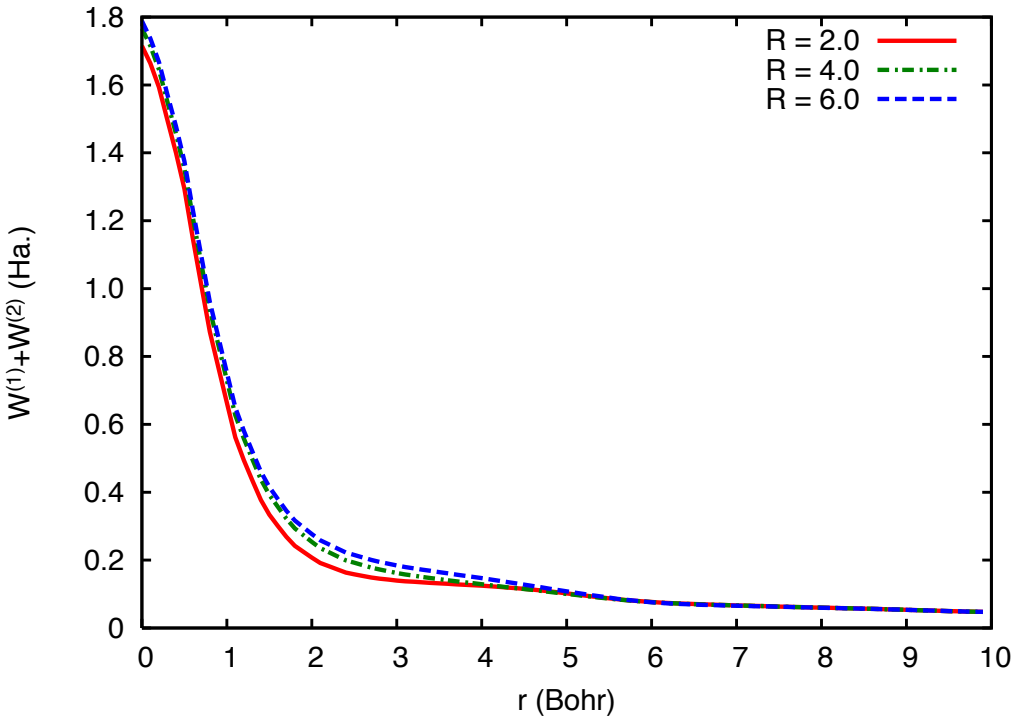

Figure 3.4: The convergence of the core-hole screening with respect to the radial cutoff (R). This radius sets the crossover between RPA and model dielectric screening. This example is showing the screening of a F 1*s* hole in LiF, and by 5 or 6 Bohr the screening is converged.

of χ^0 converges within approximately 10 to 15 Ha. of the Fermi level. The convergence of the screened potential W_0 with respect to the number of bands can be easily checked and is shown in figure 3.3 for a fluorine 1*s* hole in LiF. For all of the calculations presented here and later a 2×2×2 **k**-point grid was used to sample the Brillouin zone in the construction of the χ^0 (eqn. 3.32). In a band-structure approach, the real-space information contained in a given sampling is related to the Fourier transform of the momentum-space variables. The **k**-point sampling transforms to a super-cell, but by switching to model dielectric response at long distances, we limit the need for dense **k**-point sampling.

The crossover R between calculated and model screening is a very controlled approximation, and can be checked explicitly as in figure 3.4. More important is the approximation of spherical response. Higher-order terms in the multipole expansion of the direct are allowed, but they are assumed to be both short-range and have a screening that is relatively insensitive to the specifics

of the system as will be discussed in the next section on the exchange interaction. Systems with strong inhomogeneity, such as planar systems, will have strong anisotropy in the screening. As an example, in graphite the screening along the plane should be quite different than out of the plane, and our current approach will average these two contributions, leading to an underestimation of in-plane screening and vice versa. This approximation could be checked by expanding the response in a multipole expansion and calculating the higher-order terms, but this has not yet been done.

Some words should be said justifying the use of a statically screened potential W for the direct term. In principle the screening term depends on the binding energy of the created exciton, and the BSE Hamiltonian should itself have an energy dependence. Additionally, the finite lifetime of the exciton also influences the strength of the screened interaction. In the near-edge region, below the main plasmon peak, the static screening should be reliable, whereas at higher energies the effect of the core-hole potential on the spectra is less pronounced, allowing cruder approximations. In systems such as the $L_{2,3}$ edges in the *3d* transition metals (or $M_{4,5}$ in the *4d*) where the plasmon excitations in the valence band are of similar energies to the spin-orbit splitting of the core level there may be a need to go to dynamic screening. The effect of this approximation has not been well tested.

The RPA only includes the so-called bubble contributions, though by inverting χ^0 these are included to all orders. As a next step the screening of the valence electrons could instead be calculated at a BSE level, including the Coulomb interactions between the electron-hole pairs in the bubble diagrams. At higher orders we also expect cross-terms whereby the screening excitations interact with the exciton (see fig. 3.2). The inclusion of such terms may be necessary to capture the effects of the so-called charge-transfer satellite excitations seen in some materials such as NiO.

3.4 Exchange

Not simply just the other side of the same coin, the exchange interaction differs from the direct in an important physical way; it couples a core-hole state at $\mathbf{r}$ to one at $\mathbf{r}'$. This coupling through the exchange is primarily responsible for the mixing of L_2 and L_3 edges in the *3d* transition metals, and its neglect, the corresponding failure of one-electron models to account for $L_{2,3}$-edge

spectroscopy. Computationally, the direct term is a much simpler quantity to describe since it relies on the unscreened Coulomb interaction and is implicitly more localized. The exchange interaction,

$$V_X = \hat{a}_c^\dagger(\mathbf{r},\sigma)\hat{a}_b(\mathbf{r}',\sigma')\frac{1}{|\mathbf{r}-\mathbf{r}'|}\hat{a}_c(\mathbf{r}',\sigma)\hat{a}_b^\dagger(\mathbf{r},\sigma'), \tag{3.39}$$

involves core-hole operators at both $\mathbf{r}$ and $\mathbf{r}'$ and is therefore limited to a finite region due to the local nature of the core hole. In what follows we will drop the σ dependance, but it should be remembered that in the four-point operator V_X there are implicit Dirac deltas in the spins.

To exploit this local nature, we treat all of the exchange interactions in a localized basis around the core-hole site, denoted by the subscript α. This basis is then made up of radial functions with corresponding spherical harmonics $R_{\nu l}(r)Y_{lm}(\hat{r})$, where we allow multiple radial functions ν for a given angular momentum l. The maximum angular index of the basis needed is limited by both the falloff in contribution from the exchange interaction with that basis function and the overlap between the basis functions and the valence-band electrons. Current studies have been limited to materials with, at most, d-type occupied states, allowing us to truncate the local basis at $l = 3$. The construction of this basis is done via the projector augmented wave (PAW) formalism of Blöchl (see sec. 2.2). Of importance is that a small number of radial functions can be sufficiently complete for a finite band of energy around the Fermi level (within 100 eV), and therefore this local basis is quite compact and efficient.

The matrix elements of the exchange interaction between the core hole and local basis in principle involve scattering between arbitrary angular momenta,

$$\begin{aligned} V_X &= \langle LM,\nu lm|\frac{1}{|\mathbf{r}-\mathbf{r}'|}|LM',\nu' l'm'\rangle \\ &= \int d^3\mathbf{r}\, d^3\mathbf{r}'\, R_\alpha(r)Y^*_{LM}(\hat{r})R_{\nu l}(r')Y_{lm}(\hat{r}')\frac{1}{|\mathbf{r}-\mathbf{r}'|}R_\alpha(r')Y^*_{LM'}(\hat{r}')R_{\nu' l'}(r)Y_{l'm'}(\hat{r}), \end{aligned} \tag{3.40}$$

where the only limitation placed on the above expression is that the core hole is confined to be a set angular momentum L and also is defined by a single radial function R_α. In general the following could be worked out for a fully arbitrary combination of initial and final angular momentum states [55]. It is advantageous to expand the Coulomb interaction in terms of Legendre

polynomials in the familiar form,

$$\frac{1}{|\mathbf{r}-\mathbf{r}'|}=\sum_{k=0}^{\infty}\frac{r_<^k}{r_>^{k+1}}P_k\left(\cos(\theta)\right), \tag{3.41}$$

where θ is then the angle between $\mathbf{r}$ and $\mathbf{r}'$. Furthermore, the additive theorem of spherical harmonics allows us to replace the Legendre polynomial and its clumsy dependance on θ with spherical harmonics that separately depend on only one of the two coordinates:

$$P_k\left(\cos(\theta)\right)=\frac{4\pi}{2k+1}\sum_{m_k=-k}^{k}Y^*_{km_k}(\hat{r}')\,Y_{km_k}(\hat{r}). \tag{3.42}$$

Inserting this expression above in equation 3.40 we can now group and separately evaluate the angular parts of both integrands. Setting $\Omega\equiv\hat{r}$,

$$V_X=\sum_{k=0}^{\infty}\frac{4\pi}{2k+1}\sum_{m_k=-k}^{k}\left[\int d\Omega\, Y^*_{LM}(\Omega)Y_{l'm'}(\Omega)Y_{km_k}(\Omega)\right]\left[\int d\Omega'\, Y_{LM'}(\Omega')Y^*_{lm}(\Omega')Y^*_{km_k}(\Omega')\right]\times$$
$$\times\int d\,r\,d\,r'\,r^2(r')^2\,\frac{r_<^k}{r_>^{k+1}}R_\alpha(r)R_{\nu l'}(r)R_\alpha(r')R_{\nu l}(r'). \tag{3.43}$$

The integrals over angle lead to selection rules and can be recognized as related to the Wigner *3j* symbols,

$$\int d\Omega\, Y^*_{LM}(\Omega)Y_{l'm'}(\Omega)Y_{km_k}(\Omega) \tag{3.44}$$
$$=\sqrt{\frac{(2L+1)(2l'+1)(2k+1)}{4\pi}}\begin{pmatrix}L & l' & k\\ 0 & 0 & 0\end{pmatrix}\begin{pmatrix}L & l' & k\\ -M & m' & m_k\end{pmatrix},$$

which leads to the following selection rules in Eqn. 3.43:

$$\begin{aligned} -M+m'+m_k&=0 & \qquad M'-m-m_k&=0\\ |L-l'|\le k\le L+l' & & |L-l|\le k\le L+l&\\ L+l'+k&=2n & \qquad L+l+k&=2n \end{aligned} \tag{3.45}$$

where n is an integer, constraining the sum of the angular momenta to be even. This provides an important constraint on the number of terms that must be evaluated since only a few values of k will be allowed. Simplifying the above constraints leads to

$$M + m = M' + m, \quad m_k = M' - m, \quad l = l'. \tag{3.46}$$

To aid in computation, the integrals are precomputed and stored for each basis function in a matrix of dimension $4 \times (2L+1) \times (2l+1) \times N_v$ where the 4 arises from the core and valence spins. The action of the exchange interaction on an arbitrary vector of the core-valence exciton can then be determined by transforming this vector from the $\{n, \mathbf{k}\}$ space to the $\{l, m\}$ space, performing the matrix-vector multiplication, and then reversing the transformation,

$$\begin{aligned}
\psi^{\sigma s}_{\nu lmM} &\Leftarrow \sum_{n\mathbf{k}} A^{n\mathbf{k}}_{\nu lm} \psi_{n\mathbf{k}\sigma;Ms} \\
\tilde{\psi}^{\sigma s}_{\nu lmM} &\Leftarrow \sum_{\nu' m' M'}{}^{\nu lmM} V_X^{\nu' lm' M'} \psi^{\sigma s}_{\nu' lm' M'} \\
\tilde{\psi}_{n\mathbf{k}\sigma;Ms} &\Leftarrow \sum_{\nu lm} A^{n\mathbf{k}}_{\nu lm} \tilde{\psi}^{\sigma s}_{\nu lmM},
\end{aligned} \tag{3.47}$$

where it should be understood that the spin indices σ and s are diagonal in this interaction. This calculation is relatively efficient and presents no unique challenge for scaling up in systems size. The matrix operations are only performed on the local basis set and the cost only increases linearly with the number of Kohn-Sham states included in the calculation. An identical procedure is used for the $l > 0$ multipole parts of the direct interaction.

3.5 Spin-orbit

The core-hole states are represented in an $\{m_l, \sigma\}$ basis, but the spin-orbit interaction is diagonal in a separate $\{j\}$ basis which is the total angular momentum ($\hat{J} \equiv \hat{L} + \hat{S}$). Briefly, the spin-orbit term,

$$H_{SO} = \frac{1}{2r^3} \hat{S} \cdot \hat{L}, \tag{3.48}$$

commutes with neither $\hat{S}$ nor $\hat{L}$, but instead can be written as

$$H_{SO} = \frac{1}{2r^3}\left(\hat{J}^2 - \hat{L}^2 - \hat{S}^2\right). \tag{3.49}$$

This means that for a given edge the spin-orbit term χ_j is a matrix in the $\{m_l, \sigma\}$ space.

Edges that are split by the spin-orbit interaction ($l > 0$), also have different core-hole lifetimes for the two different j-states. To simulate this we add a j-dependent broadening term Γ_j to our hole Hamiltonian (eqn. 3.14). The values of Γ are fitted to match the experimentally observed core-hole broadening. We can split this broadening into a term diagonal in the $\{m_l, \sigma\}$ basis and an off-diagonal term. Since each core level is split in to at most two spin-orbit levels we can label these two j states as 1 and 2, yielding

$$\begin{aligned}
\Gamma_\alpha &= \frac{\Gamma_2 - \Gamma_1}{\langle \hat{L}\cdot\hat{S}\rangle_2 - \langle \hat{L}\cdot\hat{S}\rangle_1}(\hat{L}\cdot\hat{S})_{m\sigma;m'\sigma'} \\
\Gamma_\beta &= \frac{\Gamma_2\langle \hat{L}\cdot\hat{S}\rangle_1 - \Gamma_1\langle \hat{L}\cdot\hat{S}\rangle_2}{\langle \hat{L}\cdot\hat{S}\rangle_1 - \langle \hat{L}\cdot\hat{S}\rangle_2}\,\delta(m,m')\delta(\sigma,\sigma').
\end{aligned} \tag{3.50}$$

3.6 Inclusion of self-energy corrections

Within OCEAN there are several ways in which self-energy corrections can be included. The first is to utilize corrected wave functions that are solutions to the Hamiltonian including the self-energy operator (eqn. 2.6). Alternatively, when the self-energy corrections take the form of energy-only corrections, such as in the MPSE (see sec. 2.5), the self-energy can be applied in an approximate way by convoluting with the final spectra [46]. This approximation relies on the dispersion-less nature of the core hole and assumes that the self energy is independent of momentum and smooth in energy. When looking at spin-orbit–split core states, the post-convolution is not usable and the energy corrections must be added in to the BSE Hamiltonian. The MPSE prescription assigns a complex self-energy correction as a function of excitation energy such that the correct electron energy for state i has the form,

$$E_i = E_i^{\mathrm{KS}} + \Delta\Sigma_{MPSE}(E_i^{\mathrm{KS}} - E_F). \tag{3.51}$$

When complex-valued energies are used in solving the BSE care must be taken since the Hamiltonian used is no longer Hermetian. Physically this is expected since the excited states have finite lifetimes, but the computational method for evaluating the resolvent (eqn. 3.13) must be modified. Details are provided in appendix A.

3.7 Limitations of our BSE approach

At this point it is worth mentioning some of the inherent limitations of our BSE formulation of x-ray spectroscopy. This is fully independent of the numerical approximations that are in practice necessary to carry out BSE-based calculations. Our formalism here limits the electronic response to that of a single particle-hole pair, and interactions with the rest of the spectator electrons in the system are limited to the mean-field, static screening of the core-hole potential. This excludes coupling to other excitation modes in the system such as plasmon or phonon excitations. It also excludes secondary, excitonic-like excitations such as charge-transfer satellite terms where a localized, valence-band particle-hole pair can dynamically screen the primary core-conduction exciton.

While the approach outlined above explicitly avoids treating the ions in the system as anything but fixed potentials, at finite temperature phonon coupling can be important. Phonons are the bosonic vibrational modes of a crystal and tend to be low energy, with excitations in the meV range. They can be strongly anisotropic, and final-state dependent coupling can lead to large differences in broadening of the measured spectra, e.g. the differences in width of the e_g and t_{2g} peaks of the Ti $L_{2,3}$ edge in $SrTiO_2$ have been attributed to phonon coupling [56]. Inclusion of phonon effects is important for quantitative comparison between experiment and theory. Unaccounted-for broadening can point to a variety of failures in the calculation including an incorrect density of states (DOS) in the DFT calculation or insufficient screening of the core-hole potential.

3.8 Alternate approaches

Other than BSE calculations, there are two main approaches to excited-state spectroscopy for extended condensed matter systems: real-space multiple-scattering [1] and time-dependent density functional theory (TDDFT) [57]. Real-space multiple-scattering solves for the x-ray spectra

by considering the path expansion of the photo-electron around a central core hole [54]. The maximum photo-electron path that can contribute to the cross section is limited by the core-hole lifetime, and this approach converges for real-space clusters of around 100 atoms. TDDFT replaces the BSE interactions with the DFT exchange-correlation potential, e.g., the TDLDA uses the LDA form of V_{xc}. The efficiency of a local expression for the electron-hole interactions, like that provided by TDLDA, makes TDDFT an attractive approach for spectroscopy, but it is currently limited by poor approximations to the exchange-correlation potential that limit agreement with experiment.

For small clusters or molecules, other techniques such as configuration interaction, which rely on re-diagonalizing a Hartree-Fock Hamiltonian including explicit single, double, and &c. excitations, are used with excellent results, but these scale poorly with electron number [58]. There has also been recent work on coupling model Hamiltonian approaches to configuration interaction approaches which have seen moderate success [14, 15]. This method can give highly accurate results, but the computational cost precludes its use on clusters of more than a handful of atoms. At present, however, many model Hamiltonian calculations using the charge transfer multiplet formalism rely on a parameterized fitting of the experimental spectra [13].

Chapter 4
RESULTS: XANES OF SELECTED SYSTEMS

4.1 Introduction

The primary goal of the OCEAN code is to provide a platform for x-ray calculations, primarily in the near-edge region, of a wide variety of materials and systems. This includes insulating and metallic, periodic and semi-disordered, and systems with both localized and itinerant electronic states. To that end we have investigated a variety of well-characterized systems to explore the range of OCEAN's applicability. As hinted at in earlier chapters, we are mostly constrained to systems for which DFT gives a reasonable starting point and ones in which secondary excitations do not form a significant contribution of the measured response. The three sections in this chapter sketch out the reasonable limits of our current code.

4.2 Salts: KCl, LiF, and MgO

4.2.1 Introduction

As a proof of concept we investigated the K edges two diatomic salts, KCl and LiF, and the $L_{2,3}$ edge of MgO [2]. These ionic compounds are marked by strong, ground-state charge transfer from the cation to anion and *s-p* hybridization of the valence electrons, and all three of these salts crystalize in the rock-salt structure. These elements all have well-separated valence and core

Table 4.1: Salts: Convergence Parameters

System	**k**-mesh	conduction bands	approx. bandwidth (eV)	plane-wave cutoff (Ha.)	screening bands
LiF	10×10×10	56	110	50	60
MgO	10×10×10	40	80	100	200
KCl	10×10×10	42	40	80	180

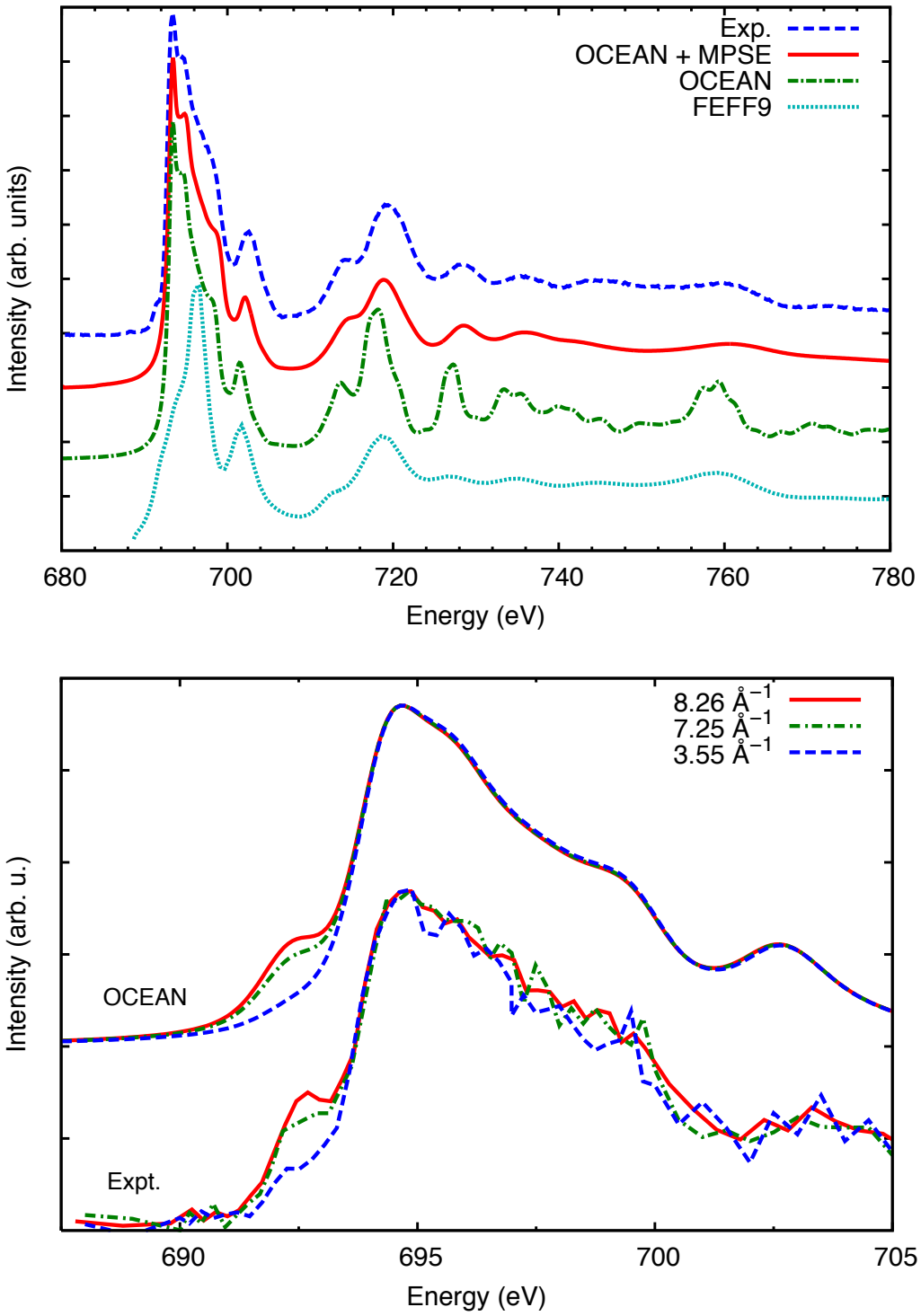

Figure 4.1: Fluorine K edge in LiF compared to experiment for both XAS and NIXS. In a) the XAS calculated with OCEAN both with and without self-energy effects from the MPSE is compared to both experiment [59] and the FEFF9 code, and in b) the momentum dependence of the near edge is compared between OCEAN and experiment [60] with the momentum transfer $\mathbf{q}$ given in inverse Å. The plots have been normalized to match each other and offset vertically for clarity.

levels, making the pseudopotential approximation more easily applicable, though, for potassium, semi-core states were also included. Due to low photon energies at all of these edges, XAS of these ions is well represented within the dipole approximation. NIXS can break these dipole selection rules, but, except for MgO, the near-edge region has little *d*-type DOS and so only *s*- and *p*-type states are probed. The lack of *d*-type states makes these systems very useful for benchmarking the OCEAN approach, removing uncertainty about the fidelity of the DFT ground-state calculation.

These diatomic salts all have quite small unit cells, making them ideal for **k**-space calculations which explicitly enforce periodic boundary conditions. Taking advantage of the cheaper computational cost of the small unit cells that describe these three salts, we calculated final states up to 100 eV beyond the Fermi level, showcasing OCEAN's accuracy over a large energy range. At large energies past the edge, alternative approaches that do not depend on the explicit calculation of unoccupied states are more efficient. For example, the FEFF9 code excels at EXAFS calculations [54]. The numerical convergence parameters used for the three systems are summarize in table 4.1.

For K-edge spectroscopy the BSE approach outlined here can be seen to be formally equivalent to the final state rule (FSR) [61]. The FSR approximates the XAS process with a one-electron golden rule expression, and hence the problem can be expressed in terms of states in the presence of a core hole [62]. This is because the 1*s* electrons are degenerate in spin and well isolated both in energy from other levels of the atom and also spatially from possibly equivalent states on neighboring atoms. The end result is that the core-hole dynamics are unimportant, and only the screened core-hole potential affects the final spectrum. Therefore differences in spectra between BSE and FSR approaches arise from the approximations made in the calculation of the core-hole potential. In our approach we are assuming linear response within the RPA while FSR often uses a fully relaxed, DFT-screened core hole.

4.2.2 Results

LiF has a relatively small dielectric constant ϵ_∞ of 1.92 which leads to weak screening of the core hole and correspondingly strong excitonic features. The experimental lattice constant of 4.03 Å was used in the calculation. In figure 4.1 we see the OCEAN results for XAS and NIXS of the fluorine K edge of LiF. Overall we see very good agreement between our calculation and exper-

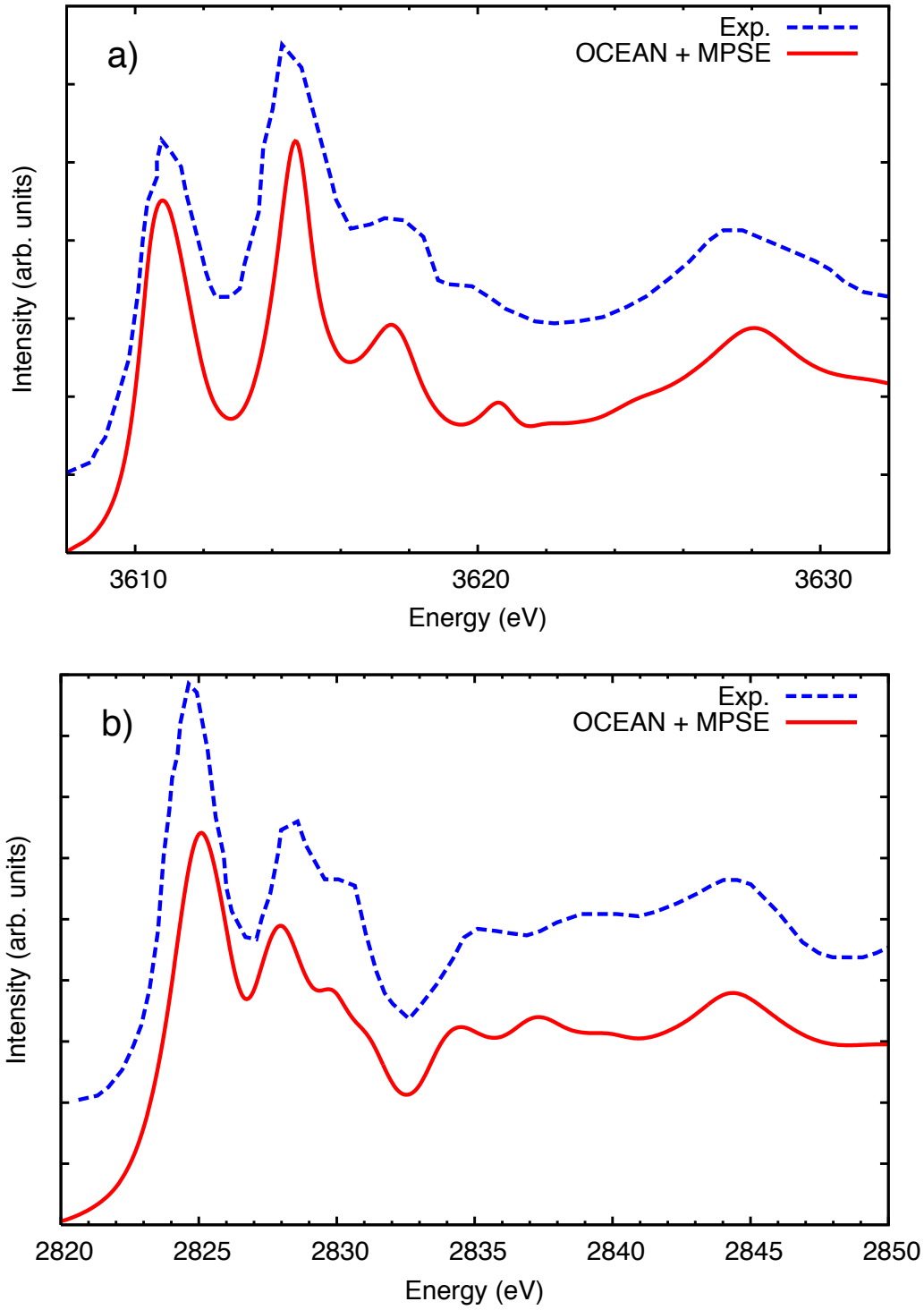

Figure 4.2: The XAS K edges in KCl for both a) potassium and b) chlorine as calculated in OCEAN compared to experiment [63]. For both the many-pole self-energy correction has been included. The spectra have been scaled to match each other and offset vertically for clarity.

iment both for peak positions and relative strengths. The fluorine K edge XAS showcases the dampening provided by the MPSE. The only *ad hoc* broadening included is the approximate core-hole lifetime and is constant across the whole energy scale, and therefore the observed smoothing at higher energies results entirely from the MPSE. The self-energy correction also provides an energy-dependent stretch to the calculated spectrum, improving agreement of the peak positions, e.g., 720 eV and above. The FEFF9 calculation is in excellent agreement with experiment as well except in the near-edge region. This is likely the result of the spherical potential, muffin tin approximation that is used in FEFF.

In the bottom panel of figure 4.1 we show the momentum dependence of the pre-edge feature. The disappearance of this feature at low $\mathbf{q}$ is the result of the exciton being dipole forbidden, while larger momentum transfer allows transitions from the 1*s* to *s*-type final states. The growth of the pre-edge feature in LiF shows excellent agreement between OCEAN and experiment. Momentum-dependent NIXS calculations are less common than dipole-limited XAS due in part to difficulties of conserving crystal momentum in non–reciprocal-space codes. The ease of performing a calculation for arbitrary momentum transfer is a strength of the OCEAN package.

Potassium chloride has a slightly smaller bandgap than LiF, a dielectric constant of 2.19, and an experimental lattice constant of 6.29 Å. For these calculations we included semi-core states in the potassium pseudopotential: *3s* and *3p*. As we see in figure 4.2, the agreement between OCEAN and experiment is excellent for both the potassium and chlorine K edges. We do see minor disagreement in peak positions at approximately 10 eV above both edges, 3620 eV for the potassium and 2835 eV for the chlorine.

For MgO we looked at the magnesium $L_{2,3}$ edge which, at 50 eV, is quite shallow. The spin-orbit splitting between the L_2 and L_3 edges in magnesium is also quite small, and is masked by the lifetime broadening and conduction band width. MgO has a dielectric constant of 2.95 and lattice constant of 4.21 Å. To ensure that the pseudopotentials were not influencing the fidelity of the calculation a very high cutoff of 200 Ry. was adopted. Better optimization could have resulted in softer potentials for the same quality of calculation, but for small test systems this was not necessary. The calculation (shown in fig. 4.3) is in reasonable agreement for peak positions, but the relative strengths are less well represented. Additionally the excitonic peak at 53 eV is too strong and too low in energy in comparison to the next major peak near 57 eV. This is likely the

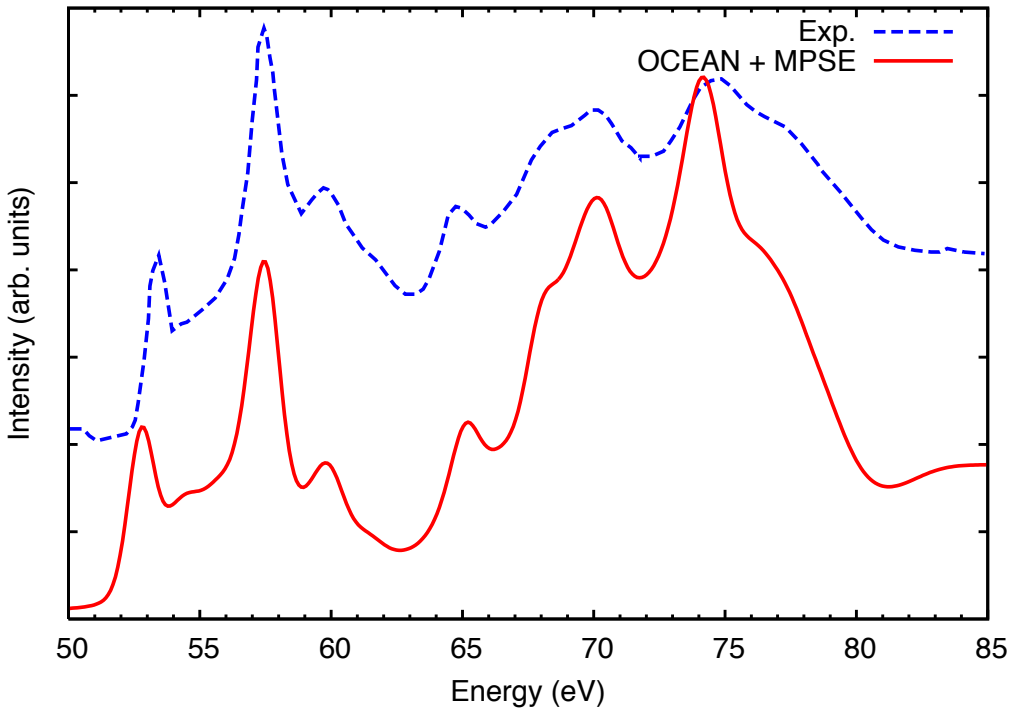

Figure 4.3: The $L_{2,3}$-edge XANES of magnesium in MgO as calculated by OCEAN compared with experiment [64].

result of insufficient screening of the core-hole potential. Other BSE-based calculations of MgO also show a strong enhancement of this exciton [5].

With the exception of MgO, OCEAN is in very strong agreement with experiment. This includes both dipole limited XAS as well as **q**-dependent NIXS. The results for MgO are also promising, though the reasons for disagreement, especially the overestimation of spectral weight around 75 eV are not known. for these systems OCEAN does an excellent job reproducing both the pre-edge and near-edge structures as well as the mid-range spectral features, 30-80 eV past the edge. At higher energies it is not expected that the pseudopotential approximations will remain good, especially in regards to reproducing scattering states so far above the Fermi level. This breakdown has not been observed because the calculation of explicit final states becomes arduous for energies far past the edge, and therefore the limit of our approach for calculated spectra far above the edge is a practical rather than theoretical one.

4.3 $L_{2,3}$ edges of 3d transition metals

4.3.1 Introduction

The $L_{2,3}$ edges of *3d* transition metals are dominated by the so-called "white lines." These are strong, narrow transitions from the occupied, spin-orbit split *2p* states to unoccupied *d*-type states. Experimentally it was seen that the L_3:L_2 ratio deviated significantly from the expected, statistical value of 2:1, instead varying from 0.8 to above 2.0[65]. The ratios are relatively constant for a specific element in different chemical environments and increase with increasing atomic number. This effect is best understood as atomic in origin, arising primarily from the large overlap between the *3d* valence orbitals and the *2p* core levels [13].

The spin-orbit splitting of the *3d* transition metals increases across their range from less than 4 eV for potassium to around 20 eV for copper. The bandwidths of the unoccupied, *3d* states tend to be small, of the order of a few electron Volts, and so for the transition metals the L_2 and L_3 edges are well separated in energy. On the other hand, these tightly bound core states are spatially confined and have correspondingly large exchange interactions. It is the interplay between the core-hole *p* and photo-electron *d* states via the exchange interaction the leads to the anomalous $L_{2,3}$ ratios. A less well examined, but equally important effect of the exchange interaction in the final state is the re-weighting of crystal-field split, unoccupied *d* bands. Similar to the L3:L2 ratio not being an accurate indicator of initial *2p* occupancies (which should always be 2:1), the ratio of unoccupied *d* states is not a true measure of their ground-state occupancies, nor is it necessarily constant between L3 and L2 edges.

The L3:L2 ratio can be estimated by comparing the relative peak intensity of the two white lines. For the elemental *3d* transition metals, the white lines are the dominant feature in the $L_{2,3}$-edge spectra. This has been done for experiment results in reference 66 and we compare to our own calculations in table 4.2. For the elements in the table we used the calculation of the metallic, elemental system to estimate the ratios, and the uncertainty is within ± 0.1.

Historically, model Hamiltonian approaches, specifically multiplet-based solutions have been used to calculate $L_{2,3}$-edge spectra [13]. This method treats the solid state environment as a perturbation of an atomic Hamiltonian, including both potentials and explicit states to simulate nearest neighbor interactions. More recently, *ab initio* configuration interaction calculations have been

Table 4.2: L3:L2 peak ratio vs. *Z* for selected *3d* transition metals

Atom	Z	Expt[66]	OCEAN	Atom	Z	Expt	OCEAN
Ca	20	0.8	0.8	Co	27	2.3	2.0
V	23	1.0	1.1	Ni	28	2.4	2.0
Fe	26	2.0	1.8	Cu	29	0.9	0.8

carried out to calculate the appropriate parameter set to use with the model Hamiltonian, making these calculations first-principles based [14, 15]. This approach, however, suffers from poor scaling and is unsuitable for large systems with more complex structures or unit cells. Other approaches such as time-dependent density functional theory (TDDFT) [11, 12], multi-channel multiple scattering [67, 68], and BSE based approaches [3–5] have been used as well, focusing primarily on the early transition metals. None of these approaches successfully accounts for the $L_{2,3}$ spectra across the full range of *3d* transition metals.

The OCEAN calculations include self-energy corrections using the MPSE except where noted. The MPSE relies on a UV/optical calculation of the loss function which was carried out using AI2NBSE. The transition metals exhibit markedly different core-hole lifetimes between the $2p^{1/2}$ and $2p^{3/2}$ core states. These widths were fit to match experiment for our calculations. In addition, Gaussian broadening was added to all the calculations to simulate experimental broadening. The numerical convergence parameters used for the transition metals are summarized in table 4.3. As for the salts, a 2×2×2 **k**-space grid was used for the screening calculation with the exception of VO_2 which utilized the same wave functions for the screening and BSE calculations, and hence used an unnecessarily large number of bands for the BSE calculation.

4.3.2 Early transition metals

The early *3d* transition metals, from potassium to chromium, have mostly unoccupied *d* bands and are often well described within DFT. We have investigated Ca, Ti, and V in both the elemental, metallic form (Ca and V only) and in the ionic compounds CaF_2, $SrTiO_3$, and VO_2. We find good agreement with experiment for all three as well as agreement with previous BSE calculations of CaF and $SrTiO_3$ [3, 4].

CaF_2 is the prototypical fluorite structure, or $Fm\bar{3}m$ space group, with a lattice constant of

Table 4.3: *3d* metals: Convergence Parameters

System	**k**-mesh	conduction bands	approx. bandwidth (eV)	plane-wave cutoff (Ha.)	screening bands
CaF_2	12×12×12	28	35	100	200
Ca	8×8×8	80	75	100	200
$SrTiO_3$	8×8×8	50	40	100	400
VO_2^*	4×4×4	480	130	100	480
V	20×20×20	25	65	145	200
Fe	8×8×8	16	70	100	240
Co	8×8×8	32	70	165	200
Ni	16×16×16	16	60	225	160
Cu	10×10×10	30	90	180	200

* See text for details on VO_2 calculation.

5.45 Å [69]. Metallic calcium forms a face-centered cubic crystal with sides of 5.58 Å [70]. Both have an almost completely unoccupied *3d* band. Our calculations can be seen in figure 4.4. In CaF_2 there is a clear splitting in the unoccupied *d* states, while in metallic calcium the calculation shows a small splitting that is hidden by final-state broadening. The presence of additional features below the L_3 edge in CaF_2 is attributed to *s*-type excitonic states, though OCEAN does not accurately place these. Of note in both spectra is the incorrect spin-orbit splitting which is calculated to be about 0.2 eV too large. This failure for calcium is common across several independent BSE implementations [3, 4]. Our calculation does an excellent job reproducing the ratio of the white lines, though the weighting between the split *d* bands in CaF_2 too strongly favors the higher energy states. Comparison is provided to the FEFF code both using a static core-hole potential and using TDDFT within the local density approximation (LDA) [11]. While the TDDFT calculation shows good agreement for the edge ratio, the overall spectral weight is still off, due either to issues with the spherical approximations made in the FEFF code, or inherent limitations in the LDA functional.

Strontium titanate $SrTiO_3$ forms a cubic perovskite crystal structure with a lattice constant of 3.91 Å [73]. The crystal-field splitting apparent in the titanium *d* states is due to the proximity

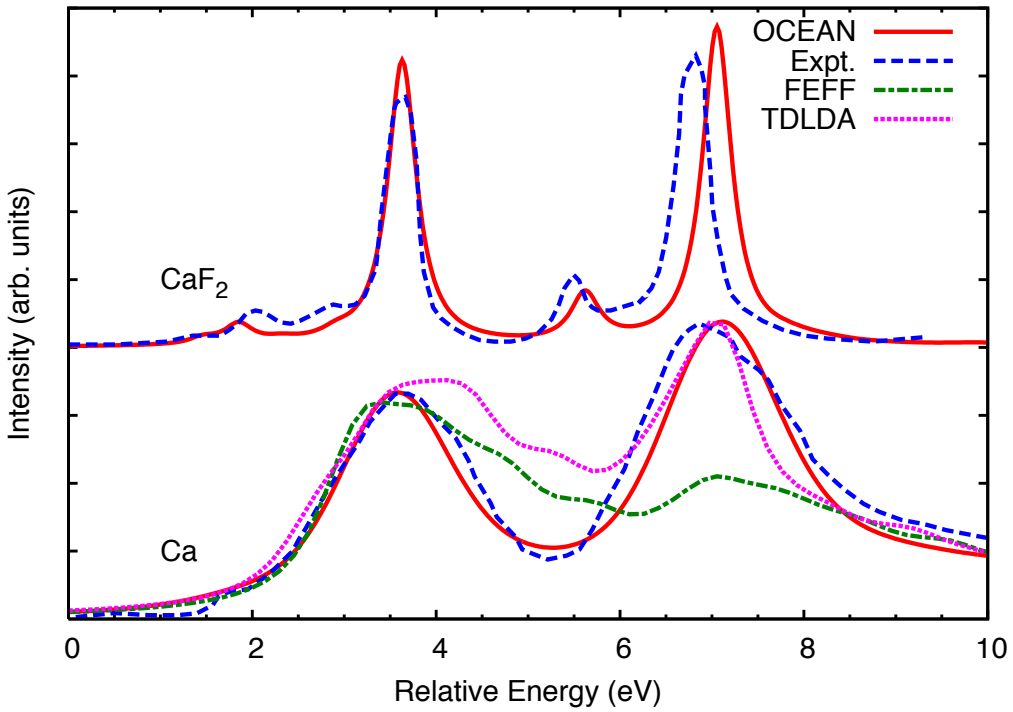

Figure 4.4: Calculated $L_{2,3}$ edges of (bottom) metallic Ca [71], and (top) Ca in CaF_2 [72] compared with experiment. The alignment of the metallic and insulating compounds was chosen to match at the L_3 edge, and the two materials have been offset for clarity. The metallic spectra show larger broadening than CaF_2 due in part to a small splitting of the *d*-type states in the metal and larger final-state broadening, which which is typical of metallic systems. For elemental Ca, calculations using the FEFF code are also included. The green, dash-dotted line shows the effects of a static core-hole potential, with the characteristic 2:1 edge ratio, while the pink, dotted line shows the improvement of using TDDFT (within the LDA).

of the oxygen atoms and is slightly larger than the splitting seen in CaF_2. With the octahedral arrangement of the oxygen the *d* states group in to two symmetry states: t_{2g} and e_g. The e_g states can also be written as d_{z^2} and $d_{x^2-y^2}$, and they are lower in energy than the t_{2g} because they minimize overlap with the oxygen *2p* states. The Ti $L_{2,3}$-edge of $SrTiO_3$ has been investigated theoretically using a variety of methods including BSE [4], *ab-initio* charge-transfer multiplets in finite clusters [74], and multi-channel multiple scattering calculations in finite clusters [75]. All of these approaches including that of our work account for the observed multiplet splittings in $SrTiO_3$ reasonably well, but tend to underestimate the broadening observed in experiment. This is due in part to the neglect of final-state-dependent phonon-broadening effects [56, 76].

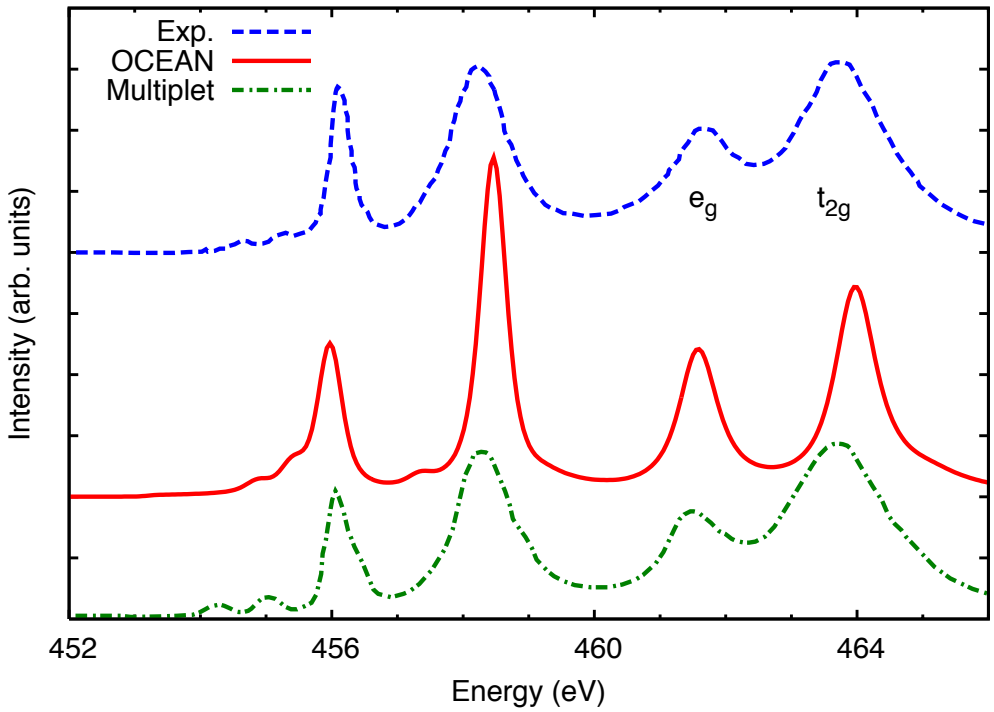

Figure 4.5: Calculated XANES spectra for the Ti $L_{2,3}$-edge of $SrTiO_3$ compared to experimental data and a multiplet calculation [77]. The calculated spectra have been offset for clarity and the broadening in our calculation neglects solid-state Coster-Kronig and phonon effects.

In our calculation, shown in figure 4.5, the splitting between the t_{2g} and e_g peaks is overestimated with the e_g peak about 2.5 eV lower than the t_{2g}. Correspondingly, the double-peaked pre-edge feature at 455 eV, which is attributed to transitions into *s*-type final states, is too close to the e_g peak. These are both symptoms of an over-binding of the e_g-like final states. This is potentially a result of the spherical approximation made in the screening of the direct interaction, such that both symmetries experience the same screening strength. The edge ratio, however, is in good agreement with experiment as is the relative weighting between t_{2g} and e_g. For comparison, figure 4.5 also includes results from a charge-transfer multiplet calculation, which is in excellent agreement with experiment but includes several free parameters, making it more suitable for analysis of experimental spectrum than prediction.

The third light transition metal we have investigated is vanadium, both in its elemental form and in VO_2. Metallic vanadium crystalizes in a body-centered-cubic structure, and the calculation

for vanadium metal shows good agreement with experiment (fig. 4.6). Vanadium has a small unit cell with a lattice constant of 3.02 Å. There is a slight overestimation of the L3:L2 ratio in OCEAN. Additionally, the experiment shows an asymmetry in broadening which is likely due to the excitation of valence-band electron-hole pairs. This is inadequately accounted for in our current approach, and more detail will be given in the next section on the later transition metals where this effect is more prominent.

Vanadium dioxide provides an opportunity to look at a material for which conventional DFT fails. At high temperatures, above 340 K, VO_2 is a conductor with a rutile crystal structure. Below this temperature the vanadium atoms dimerize, and the crystal is an M1 monoclinic insulator. It is this low-temperature phase that DFT (within the LDA) incorrectly determines to be a conductor. To correct for this we utilize the self-consistent *GW* (SCGW) method proposed by Gatti *et al*. who showed that iteratively calculating the self-energy within the *GW* correction leads to an insulating system in reasonable agreement with experiment for both the gap and low energy loss [78]. Following their prescription we were able to obtain corrected Kohn-Sham orbitals using a frequency and momentum dependent self-energy which successfully opened a gap in the ground state. With OCEAN, our hybrid *GW*/BSE scheme allows for first-principles x-ray calculations of materials that are beyond the reach of traditional DFT.

To calculate the XANES for M1 VO_2 we first calculated the LDA Kohn-Sham orbitals on a $4\times4\times4$ shifted **k**-point grid yielding 16 points in the irreducible Brillouin zone. The use of a highly symmetric set of **k**-points was necessary to reduce computational time, in contrast, typical OCEAN calculations use a symmetry breaking shift to ensure all the **k**-points are unique. The unit cell contains four formula units, and, including semi-core states, has 50 occupied bands. 186 bands were included in the *GW* calculation, using 160 unoccupied and excluding the bottom 24 valence states which are composed of vanadium *3s* and *3p*. The other Kohn-Sham states in the calculation were used in their unmodified form, but a static self-energy shift was applied to all the conduction states above band 210 to avoid a kink where the *GW* corrections were truncated. As stated above, the calculation was broken into two sections. First we iterated within the static COHSEX approximation until convergence was reached. Second, since COHSEX calculations tend to give incorrect energies, specifically overestimating band gaps, we did a full *GW* calculation using a frequency-dependent screening and numerical evaluation of the frequency integral.

The COHSEX approximation comes from writing the screened interaction in terms of a spectral function [39],

$$W(\mathbf{r},\mathbf{r}',\omega) = v(\mathbf{r},\mathbf{r}') + \int_0^\infty d\omega' \frac{2\omega' B(\mathbf{r},\mathbf{r}',\omega')}{\omega^2 - (\omega' - i\eta)^2}, \tag{4.1}$$

where η is a positive infinitesimal. Taking the Lehmann representation of the independent-particle Green's function,

$$G^0(\mathbf{r},\mathbf{r}',\omega) = \sum_i \frac{\psi_i(\mathbf{r})\psi_i^*(\mathbf{r}')}{\omega - E_i}, \tag{4.2}$$

the real part of the self-energy can be written as the sum of two terms which are called the Coulomb hole (COH) and screened exchange (SEX), which are then

$$\begin{aligned}
\Sigma^{COH}(\mathbf{r},\mathbf{r}',\omega) &= \sum_i \psi_i(\mathbf{r})\psi_i^*(\mathbf{r}')\, \mathscr{P}\left[\int_0^\infty d\omega' \frac{B(\mathbf{r},\mathbf{r}',\omega'}{\omega - E_i - \omega'}\right] \\
\Sigma^{SEX}(\mathbf{r},\mathbf{r}',\omega) &= -\sum_i^{occ} \psi_i(\mathbf{r})\psi_i^*(\mathbf{r}')\, \mathfrak{Re}\left[W(\mathbf{r},\mathbf{r}',\omega - E_i)\right].
\end{aligned} \tag{4.3}$$

The static approximation arises from taking the statically screened Coulomb interaction $W(\mathbf{r},\mathbf{r}',0)$ from which it can be seen that the COHSEX approximation reduces to

$$\begin{aligned}
\Sigma^{COH}(\mathbf{r},\mathbf{r}') &= \frac{1}{2}\delta(\mathbf{r}-\mathbf{r}')\left[W(\mathbf{r},\mathbf{r}',0) - v(\mathbf{r},\mathbf{r}')\right] \\
\Sigma^{SEX}(\mathbf{r},\mathbf{r}') &= -\sum_i^{occ} \psi_i(\mathbf{r})\psi_i^*(\mathbf{r}')\left[W(\mathbf{r},\mathbf{r}',0)\right].
\end{aligned} \tag{4.4}$$

The computational savings is clear; the self-energy is reduced to an energy independent quantity that relies only on the static dielectric function and a sum over occupied orbitals. Using the static approximation is only justifiable for energies below the plasmon energy for an insulating system, but for VO_2 we are interested primarily in correcting the states near the Fermi level that erroneously lead to a metallic ground state.

The self-consistent COHSEX calculation was iterated twelve times and the full-frequency calculation was run for five at which point the energies and wave functions were converged. Since the DFT starting point had a very incorrect, metallic character, the quasi-particle density

mixing was set to 20% to prevent spurious oscillations during convergence. The full-frequency *GW* calculation was carried out by calculating the screening for 5 imaginary energy points and for 60 real energies selected utilizing a tangent function spacing determined by setting the midpoint to 30 eV and the maximum to 200 eV. For both calculations the dielectric matrix $\epsilon(\mathbf{r}, \mathbf{r}')$ was calculated within the RPA using a truncated plane-wave basis with a 4 Ha. energy cutoff. For the self-energy an energy cutoff of 60 Ha. was used, which was necessary in part to ensure that the self-consistent iterations did not introduce errors. While the COHSEX approximation yields quasi-particle corrections that are explicitly real, the full *GW* calculation also gives the imaginary component of the self energy. This was incorporated in the BSE calculation by allowing the electron energies to be complex. The SCGW-corrected wave functions were also used to calculate the screening of the core-hole potential.

The XANES for the vanadium $L_{2,3}$ edge in VO_2 were calculated using both the LDA and the SCGW-corrected wave functions. The core-hole screening was also calculated using both approximations, as the change from semi-metal to insulator is expected to affect the strength of the potential. The results are shown in figure 4.6 for two orthogonal incoming x-ray polarizations, labeled with respect to the axes of the rutile phase. Surprisingly, the SCGW calculation has relatively little effect on the calculated x-ray spectra. For the polarization perpendicular to the *c* axis, the SCGW appears to improve agreement with experiment by increasing the energy separation between the *d* states as well as shifting spectral weight lower, but for the parallel polarization no such improvement is observed. As for $SrTiO_3$, the spherical approximation of the screened core-hole potential may be limiting the calculated, excited-state splitting of the unoccupied *d* states.

The calculations of early transition metals show good agreement with experiment both in terms of L3:L2 ratios and fine structure at the edge. There are slight disagreements for the spin-orbit splitting of calcium and the symmetry splitting of $SrTiO_3$. We attribute the discrepancy in the spacing of the Ti $L_{2,3}$-edge white lines to limitations of our spherically averaged screening of the core-hole potential. The over-estimation of the Ca L3-L2 splitting appears to be a shortcoming common to several approaches. The agreement between BSE calculations and experiment is excellent for the vanadium systems, and surprisingly, the LDA appears to adequately describe the XAS of VO_2 despite its failure to reproduce ground-state properties for this system, e.g., band gaps, and &c.

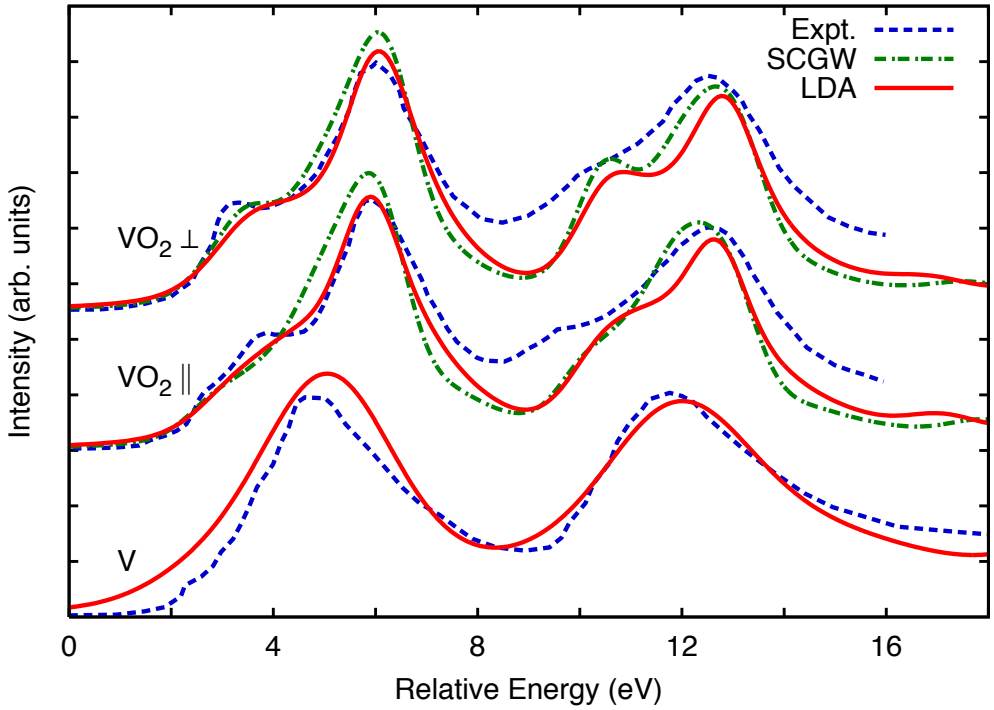

Figure 4.6: Calculated $L_{2,3}$ edges of metallic V [79] and M1 VO_2 [80], compared with experiment. The alignment of the metallic and insulating compounds was chosen to match at the L_3 edge. The VO_2 spectra are polarization dependent, shown with respect to the *c*-axis of the rutile phase, and calculated using wave functions and energies from both the LDA (red, solid line) and self-consistent *GW* (green, dashed line) as input to the BSE.

4.3.3 Late transition metals

The late transition metals are characterized by mostly filled *d* bands. Even in strongly ionic compounds, the metals retain several occupied *d* orbitals which can greatly complicate both the ground-state picture and the excited-state spectroscopy. Famously, the LDA both fails to sufficiently localize *d* or *f* electrons and underestimates the strength of the Coulomb repulsion between electrons of opposite spin in the same orbital. This has lead to DFT calculations failing to predict both Mott-Hubbard and charge-transfer type insulators. In the excited system, the presence of localized electronic states, both occupied and unoccupied, around a deep, localized core hole can lead to charge-transfer excitations. In this subsection we will look at elemental iron, cobalt, nickel, and copper $L_{2,3}$ edges.

The group-VIII metals, iron, cobalt, and nickel, all show similar features in their L-edge

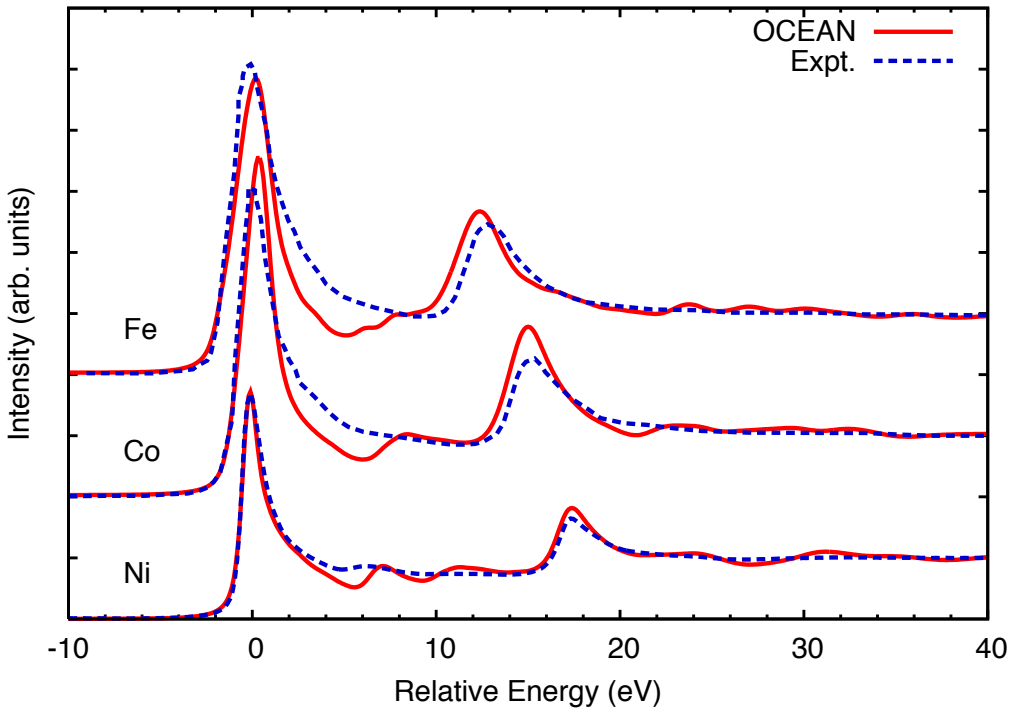

Figure 4.7: Calculations of the $L_{2,3}$ edge XAS of Fe, Co, and Ni metal compared with experiment [81, 82]. The calculations are scaled to match the high energy tails, and all the spectra are aligned at the L_3 edge to show the evolution of the spin-orbit splitting.

XANES. As the *d* band fills up, the white lines decrease and the L3:L2 ratio increases. For all three of these metals we have used the local spin density approximation to calculate the Kohn-Sham wave functions. All three exhibit ferro-magnetic ground states, and it is important to include this effect in the calculated spectra. Specifically, the difference in occupations for spin-up versus spin-down can have a strong effect on the exchange interaction. There has been recent work on these metals going beyond DFT, such as dynamical mean field theory calculations that show that these metals exhibit a large spin dependence in the self-energy and a shift of the minority-spin densities of state down toward the Fermi level [83]. As for most of our calculations in this work, we use the MPSE approximation for quasi-particle corrections, and so such spin-dependent effects on the single-particle wave functions are beyond our current approach.

In figure 4.7 we show our calculations of Fe, Co, and Ni compared with experimental XAS. The three sets of spectra are aligned at the L_3 edge to showcase the evolution of the spin-orbit

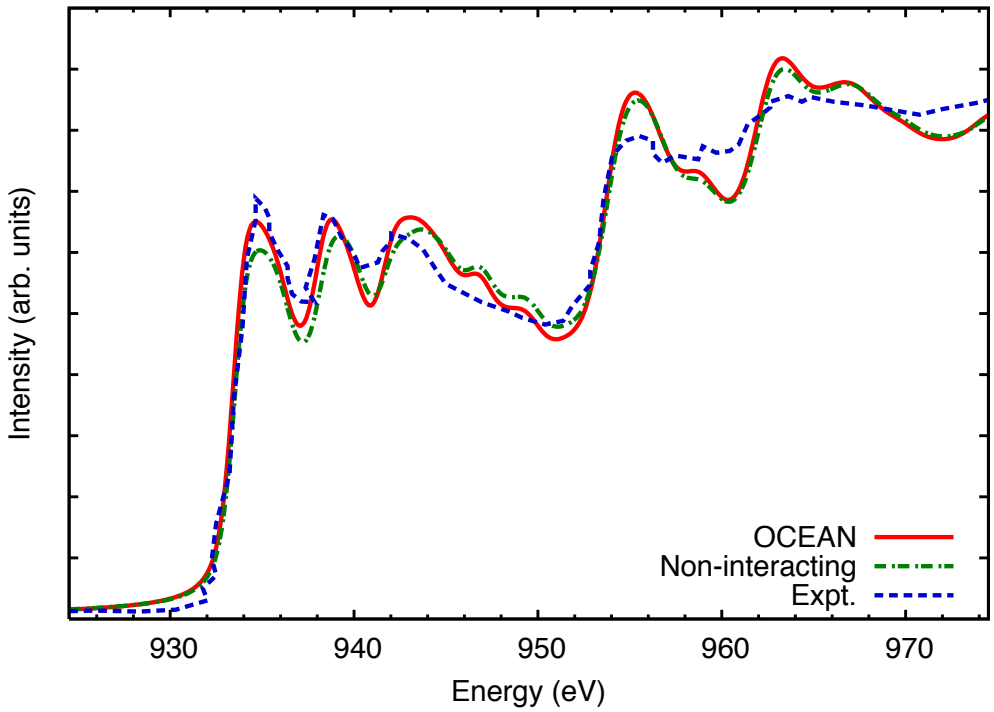

Figure 4.8: Calculations of the $L_{2,3}$ edge XAS of metallic Cu with and without electron-hole interaction terms compared to experiment [86].

splitting. We see relatively good agreement for L3:L2 ratios, but a systematic underestimation of spectral weight approximately 6 eV above the L3 edge. This we attribute to low-energy, valence-band electron-hole excitations that are neglected in our BSE approach. In contrast, the feature at 7 eV in Ni (higher in Co and Fe) appears in calculations neglecting electron-hole interactions (not shown) and has been attributed in previous work to a band-structure effect [84]. Also apparent in the experimental data is an asymmetry in the white lines which is a hallmark of a Fano line shape. Including vertex corrections, or re-expressing the self energy using the cumulant formalism, this asymmetry can be identified with the slope of the quasi-particle lifetime [85]. In this work this effect is simulated by applying a constant 5% asymmetry via convolution to all three group-VIII metals. This serves as an estimate of the magnitude of the terms neglected in our current approach.

Copper is distinct from the other transition metals by having a completely occupied *d* band with a nominal valence electronic configuration of $4s^1 4d^{10}$. The lack of empty *d*-type final states

manifests itself in an absence of white lines in the $L_{2,3}$-edge spectra. The combination of weak exchange interactions and efficient screening results in reasonable agreement between experiment and a non-interacting calculation — a calculation in which both exchange and direct terms have been ignored. As can be seen in figure 4.8 our BSE calculation, including the direct and exchange interactions, shows slightly better agreement than the non-interacting results near the L_3 edge where the core-hole is not completely screened, leading to slight excitonic enhancement. The differences between the BSE and non-interacting calculations are, however, small.

4.4 Disordered systems: liquid and solid H_2O

4.4.1 Introduction

There has been substantial effort in modeling and understanding the local structure of liquid water. Much of the interest is driven by a desire to understand chemical and biological systems that exist in aqueous environments. Molecular dynamics and other simulations of water are compared to bulk properties, but local, finite-temperature fluctuations are less well understood. Recently, many attempts to understand the connection between the spectra and local structure of both liquid and ice H_2O have been undertaken [87–103]. Despite these efforts, quantitative agreement between experiment and theory is still lacking. Our efforts to understand and model the optical and x-ray spectra of water and ice have been written up in reference 104.

Difficulties abound in understanding disordered systems like ice and water. Part of this arises from experimental limitations such as growing single-crystal ice to avoid contributions from grain boundaries or edge effects from confining liquid samples. Theoretical treatments require large super-cell methods to adequately treat proton disorder and fluctuations. Configurational averaging is necessary to adequately represent the disorder in the physical systems. The low mass of the hydrogen atom leads to a large amount of zero-point motion, and even low temperature ices exhibit large amounts of disorder. Molecular dynamics simulations that treat the ions as classical, point potentials will fail to adequately represent the behavior of the hydrogens.

A variety of approximations have been used to date to reduce the computational complexity of the problem. These include the use of transition-state potentials, effective one-electron approaches, and self-consistent DFT super-cell approaches, and the variety of methodologies has

Table 4.4: H_2O: Convergence Parameters

System	**k**-mesh	conduction bands	approx. bandwidth (eV)	plane-wave cutoff (Ha.)	screening bands
ice-Ih	4×4×4	400	45	50	900
ice-VIII	10×10×10	126	75	60	900
liquid	4×4×4	300	45	50	400

produced an equally diverse set of results. These previous calculations have been used as a tool for understanding the local geometry of water, and, based on fitting of experimental x-ray spectra to calculations, controversial claims about the nature of hydrogen bonding in water have been made [91, 102]. The connection between structure and calculated spectra is quite sensitive to the approximations made in the calculation, especially in regards to the core-hole screening, and other approaches have not reached the same conclusions, e.g., [101]. In this section we will show how the BSE approach in the OCEAN package succeeds in reproducing the main features and trends in the spectra across a range of H_2O phases, including ice phases with well-specified structures. We have carried out calculations of two ice phases as well as liquid water, and the numerical convergence parameters are summarized in table 4.4.

The x-ray spectroscopy of disordered systems like water introduces a new complication for our approach: the existence of nonequivalent atomic sites. Each oxygen is in a slightly different chemical environment, and the 1*s* states will feel different electric potentials from the valence electrons and other ions. To approximate this we introduce a site-dependent core-hole binding energy correction,

$$E_\alpha^{1s} = E_0^{1s} + V^{\mathrm{KS}}(\tau_\alpha) + 1/2 W_C(\tau_\alpha). \tag{4.5}$$

Here V^{KS} is the Kohn-Sham potential and W_C the valence electron response that screens the core hole, identical to that calculated for the direct interaction. Both are evaluated at the core-hole coordinate τ_α. The absolute binding energy is not calculated and the shift E_0 is used to align the calculated spectra with experiment as for all OCEAN calculations.

4.4.2 Ice Ih and VIII

With at least 15 distinct crystalline phases and several amorphous phases, solid H_2O has a rich phase diagram. Complicating this picture is the question of proton ordering. The only stable, accessible phase of ice with proton ordering is ice-VIII. However, recent XANES at the O K edge of both ice-VIII and the related, proton-disordered ice-VII showed no effect on the spectra coming from this transition [105]. Even at low temperatures, the zero-point motion of the hydrogen atoms is significant and is poorly captured by approaches that treat the ions as classical particles. It has been suggested in other theoretical approaches that the inclusion of disorder from zero-point motion has a significant effect on x-ray spectra, specifically stretching out the unoccupied states in energy and improving agreement with experiment for the overall width of the x-ray absorption features [102]. The current implementation of OCEAN is limited to cells of moderate size, precluding the inclusion of proton disorder in our ice cells while maintaining no net dipole moment.

We investigated two phases of solid H_2O: Ih and VIII. Ice-VII is stable below 273 K and in pressures ranging from 2 to 50 GPa, while ice-Ih is the common, hexagonal ice stable under ambient pressure. Our ice-Ih cell contains 16 molecules and was constructed by enforcing the experimental density and following the ice rules for hydrogen placement. The O-H bond length was fixed at 1.01 Å with an H-O-H angle of 106°. A more realistic simulation would allow for hydrogen disorder around these average values. The ice-VIII unit cell contains only 4 molecules with anti-ferroelectric hydrogen ordering, using the experimental lattice constants determined at a pressure of 2.4 GPa. [107]. Due to the pressure requirements of ice-VIII, experiments are performed in diamond anvil cells, and optical and soft x-ray measurements can not be carried out. However, NIXS, with its much higher photon energy, is compatible with the setup.

For ice-Ih both valence and O K-edge XANES spectra were calculating using the AI2NBSE and OCEAN packages respectively. The valence calculation is shown in figure 4.9 and was carried out both using the MPSE corrections and using a simple scissor-operator shift to illustrate the effects of the self-energy on the spectra. The calculated excitonic peaks at 8 and 10 eV are significantly stronger than those measured. Between 10 and 20 eV the absorption is also too strong and too thinly peaked compared to experiment which exhibits additional broadening past 15 eV. These

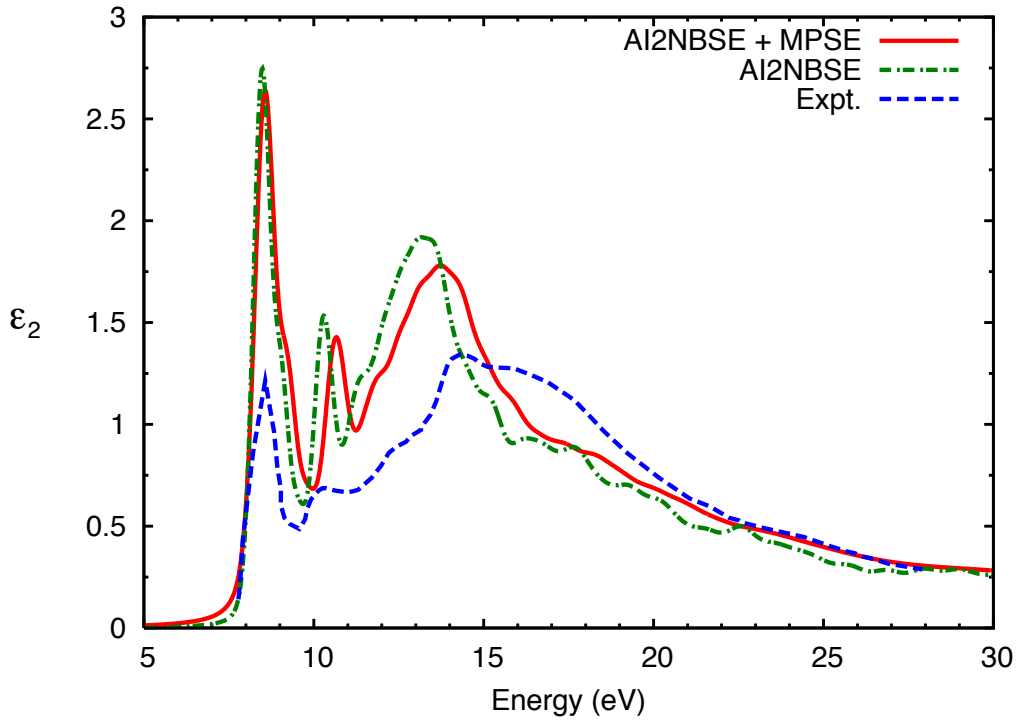

Figure 4.9: The imaginary part of the dielectric constant of ice-Ih calculated using AI2NBSE with the MPSE correction (solid red) and with a only static energy shift (dashed-dotted green). For comparison an experimental measurement of ice-Ih is shown (dashed blue) [106].

discrepancies are partly due to the lack of disorder in our model structure and point to the need to consider more elaborate models that can account for such disorder. The effect of the MPSE is seen as a stretch of the spectra together with energy dependent broadening. Coupling between electronic excitations and phonons is expected to provide small additional broadening, but is not included in this work. Previous BSE-based studies of the valence spectrum of hexagonal ice yielded qualitative agreement with experiment [108].

In figure 4.10 we present the oxygen K-edge XANES for both ice-Ih and ice-VIII for zero and finite momentum transfer. To simulate these spectra the results were averaged over orthogonal photon polarization (momentum transfer) directions for XAS (NIXS). Both ices show a strong pre-edge feature that grows with increasing momentum transfer that has been attributed to an *s*-type exciton [105]. The growth, and hence the fraction that is *s*-type instead of *p*-type, is overestimated by OCEAN for both phases. This could arise from a failure of the DFT exchange-

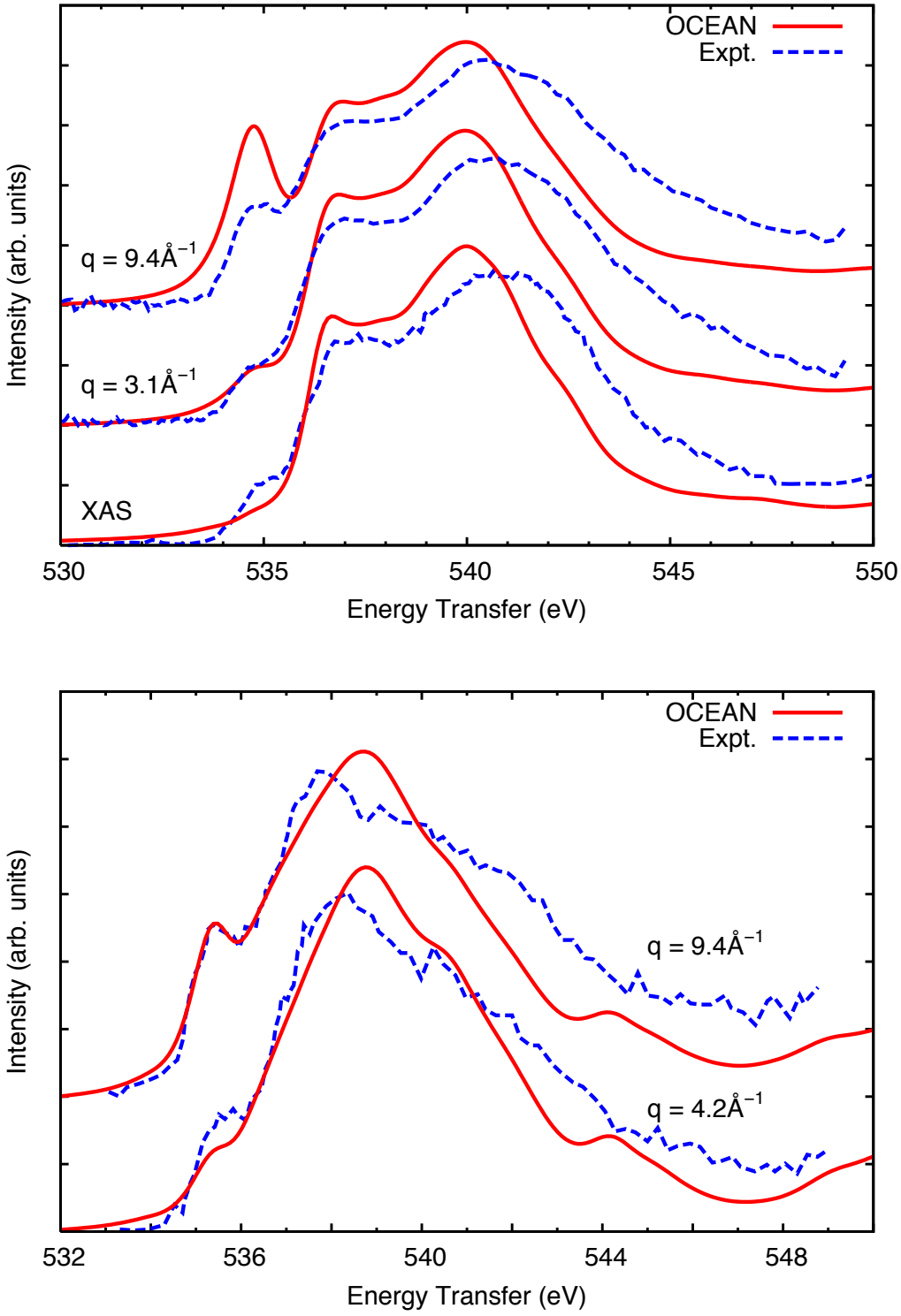

Figure 4.10: The calculated momentum-transfer dependence of the oxygen K edge for a) ice-Ih and b) ice-VIII. For comparison experimental results for XAS [109] and NIXS [105] are also shown. The pre-edge feature in both phases shows strong growth with increasing momentum transfer **q**.

correlation potential to accurately describe these molecular-like low-lying conduction orbitals or a lack of disorder in the hydrogen bonds that would distort the *s*-character of the lowest unoccupied molecular orbital. Additionally, calculations of both ices give an overly narrow edge which is reminiscent of the failure of the valence-band calculation to give adequate spectra weight above 15 eV. We propose that this failure is due in part to lack of disorder in our simulation structures. Our calculated x-ray spectra of ice-VIII shows improved agreement with experiment compared to previous work that relied on a DFT super-cell based method [110].

4.4.3 Liquid water

For liquid water we used 17-molecule cells based on molecular dynamics (MD) calculations of Garbuio *et al*. [111]. While quite small, these cells already exhibit a large amount of disorder and show reasonable agreement with experimental pair-distribution functions [104, 111]. However, the small size leads to unphysically large net dipole moments which vary from 14 to 28 Debye. Bulk water is fully disordered with a net dipole moment of 0, and the individual water molecules in the liquid phase have an average dipole moment of 2.9 D [112].

The valence spectra calculated with AI2NBSE shows excellent agreement with experiment (fig. 4.11). Only a single MD snapshot was selected for the valence calculation, and, as for the ice-Ih optical spectra, the calculation was carried out both using the MPSE and a static shift. In general the agreement for both peak spacing and overall spectral weight is excellent. Unlike for ice, the MPSE appears to over-stretch the spectra, yielding slightly worse agreement with experiment. The energy dependence of our MPSE introduces a stretch in the spectrum of approximately 5% in the range of 10 to 20 eV, while Garbuio *et al*. reported the *GW* energy correction to be almost constant across the low-lying conduction bands for water. The discrepancy between these two *GW* results arises from the approximations made in each, but more accurate investigations of the self-energy of liquid water systems to resolve this difference have not yet been carried out. The improved agreement in feature width and spectral weight from ice (fig. 4.9) to water (fig. 4.11) may be in part due to the natural disorder that any water structure must have in contrast to our completely ordered ice-Ih and ice-VIII cells.

While the screened core-hole potential was found to be quite similar between different oxygen sites, reflecting the molecular nature of liquid water, the K-edge XANES shows remarkable

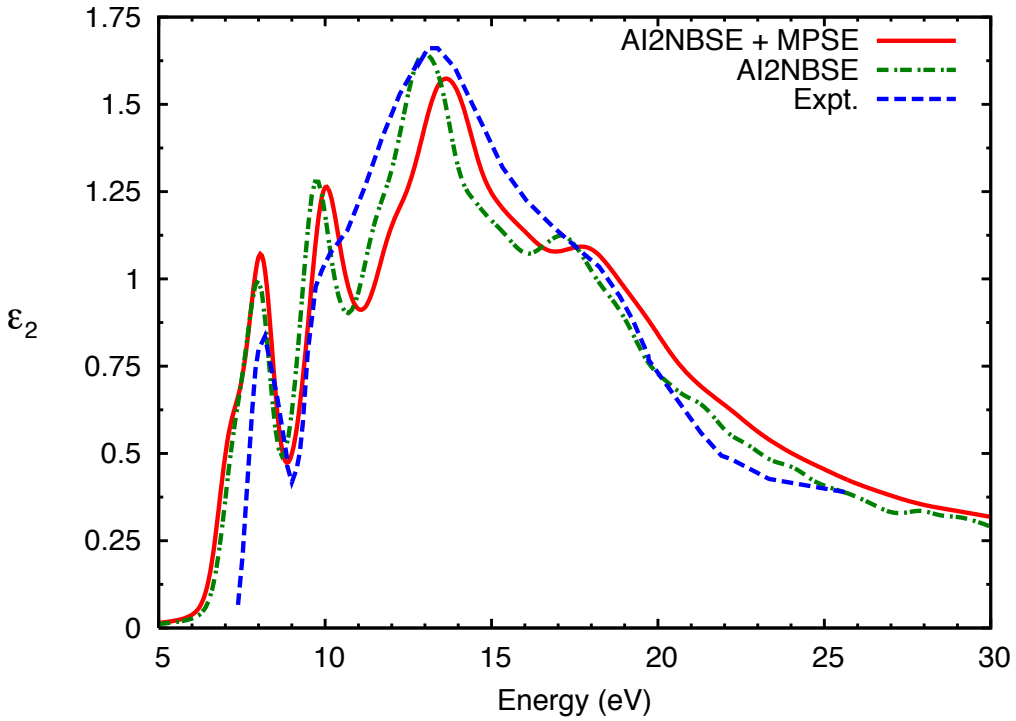

Figure 4.11: Calculated ϵ_2 spectra for a single MD snapshot of a 17-molecule water cell using the MPSE (solid red) and a static energy shift (dot-dashed green) compared to experiment (dashed blue) [113].

variation between sites and cells. For the OCEAN calculation eight MD snapshots were selected, and in figure 4.12 we show both the averaged XANES as well as error bars representing the rms variation between cells. As for the ice x-ray results (fig. 4.10), the overall edge feature is too narrow, though the water results are only too narrow by about 1 eV. The main peak at 537 eV is stronger than in experiment, and while the shoulder at 541 eV is evident in our calculations it is too weak. The strength and positioning of the pre-edge peak at 535 eV agrees quite will between OCEAN and experiment.

We find that the unphysical dipole moments of the the small unit cells in this study have a systematic effect on the calculated spectra (inset of fig. 4.12). That is, the two main peaks of the calculated O K edge at 537 eV and 540 eV exhibit shifts in intensity and position that loosely correlate with dipole moment, i.e., the local, static electric field felt by each water monomer in the ground state. At higher values of the dipole moment the main-edge features shift to lower

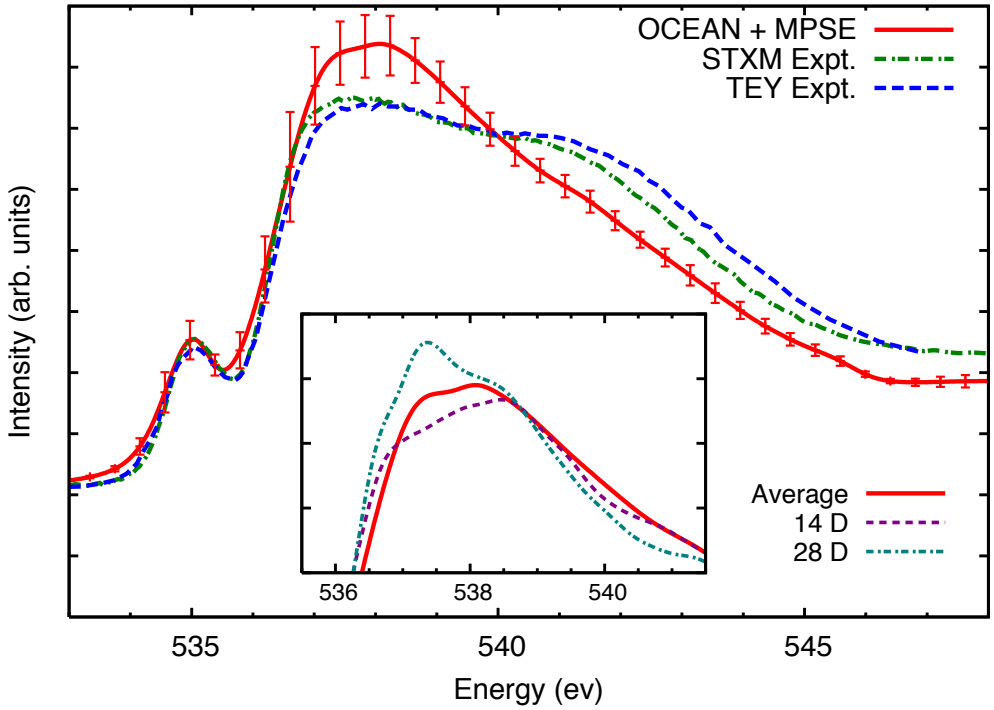

Figure 4.12: The XANES spectra for the O K edge in water. The OCEAN results, including the many-pole self-energy, are compared with recent Scanning Transmission X-ray Microscopy (STXM) [114] and Total Electron Yield (TEY) experiments [115]. The error-bars for the calculation represent the rms variation between the 8 different MD snapshots, showing reasonable similarity between the spectra from different geometries sampled by the MD despite the limited cell size. Inset: The main edge for the MD snapshots with the lowest and highest dipole moments compared to average (solid). With decreasing dipole moment the first peak intensity decreases with a slight shift to higher energies, a trend consistent with a decrease in the discrepancy with experiment as the net dipole moment approaches zero (see text).

energies, increasing discrepancy with experiment. This again points to the need for simulations with larger cells that more accurately characterize the model structure and properties.

4.5 Conclusions

In this chapter we have demonstrated OCEAN's utility for calculating the XANES of a wide variety of crystalline and semi-disordered materials. Using the OCEAN package we find good agreement with experimental results for both metallic and insulating systems and for both K and L edges. Combined with the valence BSE code AI2NBSE we are able to calculate *ab initio*

electronic response to photons at UV through x-ray energies. We also demonstrated OCEAN's applicability to finite momentum transfer NIXS. Cells of up to 500 Å or some 200 valence-band electrons are feasible, allowing the calculation of semi-disordered systems or systems with large, complex unit cells.

Chapter 5
RESONANT INELASTIC X-RAY SCATTERING

Resonant inelastic x-ray scattering (RIXS) is a photon-in/photon-out spectroscopy which arises from expanding the electron-photon interaction to second order. Unlike NIXS, there is a contribution from the intermediate excited state, making RIXS computations more complicated. RIXS requires measurement of the response as a function of both incoming and outgoing energy, and hence has a much lower count rate than XAS or XES. It has only become readily experimentally accessible in the last decade due both to increases in x-ray source flux and detector capabilities [116–118]. RIXS is divided into two types: direct and indirect. In direct RIXS the absorbed x-ray excites a core electron up into the conduction band and a second photon is emitted when a state below the Fermi level fills the initial core hole, leaving behind a shallower hole in the final state. In indirect RIXS the excited electron falls back into the core hole, and it is secondary excitations caused by the core-hole potential such as charge transfer, d-d^*, or phonon excitations that lead to energy and momentum transfer. We are constraining ourselves to the investigation of direct, valence-band RIXS, where the final-state hole is contained in the valence band, as opposed to a second, shallower core hole. Because RIXS is dependent on both the incoming and outgoing x-rays, the spectra are sometimes displayed as a 3-dimensional data set, with the cross section as a function of both photon energies. We will refer to this construction as a RIXS map.

5.1 *Theory*

Splitting the electron-photon Hamiltonian into an interacting and non-interacting part, to second-order the full cross section will be of the form

$$\sigma \propto \sum_F \left| \langle F|H_{\text{int}}|I\rangle + \sum_N \frac{\langle F|H_{\text{int}}|N\rangle\langle N|H_{\text{int}}|I\rangle}{\tilde{E}_I - \tilde{E}_N} \right|^2 \delta(\tilde{E}_F - \tilde{E}_I), \tag{5.1}$$

where H_{int} was defined in equation 1.2 and the tildes indicate the energies should include both electron and photon contributions, though the intermediate state may or may not contain an

x-ray photon. It is important to note that the intermediate state N includes the effects of electron-electron interactions such as the core-hole potential. Restricting ourselves to photon-in/photon-out spectroscopy, we would expect contributions from both the $|\mathbf{A}|^2$ term at first-order in the interaction and from the terms arising from the second order contribution of H_1 (from eqn. 5.1) to be of the same order of magnitude. The second-order contributions to the cross-section yield three terms,

$$\sigma \propto \frac{\omega'}{\omega} \sum_F \left| \frac{1}{2c^2} \langle F|\mathbf{A}\cdot\mathbf{A}'|I\rangle + \frac{1}{c}\sum_N \left[\frac{\langle F|H_1'|N\rangle\langle N|H_1|I\rangle}{E_I+\omega-E_N+i\Gamma} + \frac{\langle F|H_1'|N\rangle\langle N|H_1|I\rangle}{E_I-E_M-\omega'} \right] \right|^2 \delta(E_F-E_I+\omega'-\omega), \quad (5.2)$$

where the the primes refer to the outgoing photon and the energies refer to the electronic system, not counting the photon energies ω or ω'. These three contributions are referred to as NIXS, RIXS, and the anomalous scattering. Tuning the x-ray to near a core-level resonance the denominator of the second term can be quite small, enhancing its contribution and allowing us to drop the first and third terms entirely. Furthermore the $|\mathbf{A}|^2$ term includes a dot product between polarization vectors of the incoming and outgoing photons. In experiment this term can be suppressed by setting the detectors normal to the incident beam. Using the earlier definition of D (eqn. 1.7), we can now write the RIXS cross section,

$$\sigma(\omega,\omega') \propto \sum_F \left| \sum_N \frac{\langle F|D'|N\rangle\langle N|D|I\rangle}{\omega+E_I-E_N+i\Gamma} \right|^2 \delta(E_F-E_I+\omega'-\omega). \quad (5.3)$$

The dependence on momentum and polarization has not been made explicit.

The RIXS process does not contain a core hole in the final state. This allows the measurement of XAS without core-hole broadening through a technique called high-resolution x-ray florescence. The energy dependence of the absorption (integrating the cross section over the emission energy) is broadened only by the final-state exciton lifetime [119]. Additionally, there is no explicit measurement of which atom absorbed the incoming photon, and hence the initial core-hole excitation and corresponding excitonic state should be a superposition of excitations from every atom in the unit cell. This allows interference between contributions from equivalent

ions in the cell which must be taken into account in the calculation.

5.2 *Approach in* OCEAN

In principle the calculation of RIXS requires a double sum over two different types of excited states, one set with a valence hole and one with a core hole. We start by setting the initial electronic energy to zero and defining the intermediate, excitonic state created by the incoming photon,

$$|Y(\omega)\rangle = \sum_N \frac{|N\rangle\langle N|}{\omega - E_N + i\Gamma} D|I\rangle. \tag{5.4}$$

As for the XAS case, we assert that our many-body electronic states can be expressed as a single excited electron and hole,

$$|y(\omega)\rangle = \sum_{c\alpha\ c'\alpha'} |c\alpha\rangle\langle c\alpha| \frac{1}{\omega - H_{\mathrm{BSE}} + i\Gamma_\alpha} |c'\alpha'\rangle\langle c'|d|\alpha', \omega\rangle, \tag{5.5}$$

where d is the single-particle electron-photon coupling, exciting an electron from core state α to conduction state c, e.g., the dipole operator. We have also explicitly written the core-hole lifetime broadening term Γ_α, which physically limits the resolution of the intermediate state and computationally ensures that the resolvent is not singular. The BSE Hamiltonian is in general not diagonal in the electron-hole basis. Taking equations 5.3 and 5.4 we can write the cross section as

$$\begin{aligned}\sigma(\omega, \omega') &\propto \sum_F \left|\langle F|D'|Y(\omega)\rangle\right|^2 \delta(E_F + \omega' - \omega) \\ &\propto \mathfrak{Im}\left[\sum_F \langle Y(\omega)|D'|F\rangle \frac{1}{\omega - \omega' - E_F} \langle F|D'|Y(\omega)\rangle\right].\end{aligned} \tag{5.6}$$

Taking the approximation that each final state can be constructed out of a single Slater determinant, we insert a complete set of valence-conduction electron-hole pairs and this formula becomes

$$\sigma(\omega, \omega') \propto \sum_{vc\ v'c'} \mathfrak{Im}\left[\langle y(\omega)|d'|vc\rangle\langle vc| \frac{1}{\omega - \omega' - H^v_{\mathrm{BSE}}} |v'c'\rangle\langle v'c'|d'|y(\omega)\rangle\right]. \tag{5.7}$$

Here the Hamiltonian H^v_{BSE} is the valence-band formulation of the BSE since the final state is

a valence-hole–conduction-electron exciton [8]. Throughout, we have neglected the polarization vector and momentum of the x-ray photons. Momentum conservation is carried out explicitly with each $\{vc\}$ pair constrained such that the momentum difference between them is $\mathbf{q} = \mathbf{k} - \mathbf{k}'$, i.e., the momentum transferred to the system by the x-rays. The polarization dependence is accounted for in the evaluation of the matrix elements of d and d'.

Lastly, it is convenient to also define the vector $|x(\omega)\rangle$ which serves as the seed vector for computing the loss,

$$|x(\omega)\rangle \equiv \sum_{vc} C_{vc}|vc\rangle = \sum_{vc}\sum_{\alpha}|vc\rangle\langle v|d'|\alpha\rangle\langle\alpha c|y(\omega)\rangle. \tag{5.8}$$

The vector $|x\rangle$ can then be inserting into equation 5.7 above giving

$$\sigma(\omega,\omega') \propto \mathfrak{Im}\left[\langle x(\omega)|\frac{1}{\omega-\omega'-H^{v}_{\mathrm{BSE}}}|x(\omega)\rangle\right]. \tag{5.9}$$

It is equation 5.7 that we solve using the OCEAN code, necessitating first a solution for an excitonic wave function $|y\rangle$ at every ω. Despite the need to solve for a new exciton at each incoming photon energy (and momentum and polarization) the dimension of the BSE Hamiltonian is such that an approximate method is preferable to full diagonalization. For this we left multiply equation 5.5 by the matrix $(\omega - H_{\mathrm{BSE}})$ to get

$$(\omega - H_{\mathrm{BSE}})\,y(\omega) = B(\omega), \tag{5.10}$$

where the vector $B(\omega) \equiv \sum_{c\alpha}|c\alpha\rangle\langle c|d|\alpha\rangle$. This amounts to solving the coupled linear equations $Ax = b$, and the generalized minimal residual method (GMRES) is used [7, 120]. Only around 100 iterations are necessary to get the solution, though the speed of convergence depends on both the intrinsic core-hole width and the dimension of the BSE Hamiltonian.

Having solved for the intermediate-state exciton, the seed vector for final state is determined by an XES process that creates a valence hole v and depends on the outgoing photon. This valence-conduction seed vector is analogous to the one created in the valence-band absorption of an optical or UV photon, and the absorption spectrum as a function of energy loss $(\omega - \omega')$ is

solved for using the valence BSE code AI2NBSE.

5.3 Excitonic effects and interference

A full RIXS calculation using OCEAN combines equations 5.5 and 5.7, using the appropriate valence or core-level approximation to the BSE for each. Approximations can be made to either or both of these excited states. As a zeroth-order approximation, the interactions can be neglected for both steps, reducing the calculation to a crystal-momentum conserving convolution of the non-interacting valence and conduction states, projected onto the core hole. Due to the small photon momentum at soft x-ray edges, the electrons see very little change in their crystal momentum, and so RIXS is in turn a surrogate band-structure measurement. This assumption has been used to extract band structures based on experimentally measured RIXS [121]. We also expect excitonic effects in the final state to play a role in RIXS, allowing bound excitons below the non-interacting band gap. While the emitted spectra are sensitive to the inclusion of valence-band interaction terms, the overall trends of structure in the RIXS map are less so, allowing the time-saving step of replacing the valence Hamiltonian with $H_0^v \equiv E_c - E_v$.

The use of RIXS to extract information about the band structure relies on the relative importance of band-structure effects over core-hole interactions. The intermediate state exciton $|y(\omega)\rangle$ can be approximated by neglecting core-hole interactions and instead writing

$$|y(\omega)\rangle = \sum_{c\alpha} |c\alpha\rangle \frac{1}{\omega - (E_c - E_\alpha) + i\Gamma_\alpha} \langle c|d|\alpha, \omega\rangle, \tag{5.11}$$

which is now diagonal in the electron-hole basis. The interacting form of $|y(\omega)\rangle$ can be expanded giving

$$|y(\omega)\rangle = \sum_{c\alpha\, c'\alpha'} |c\alpha\rangle \frac{1}{\omega - (E_c - E_\alpha) + i\Gamma_\alpha} \langle c\alpha| \left[1 + (V_X + V_D) \frac{1}{\omega - H_{\mathrm{BSE}} + i\Gamma_\alpha} \right] |c'\alpha'\rangle \langle c'|d|\alpha', \omega\rangle, \tag{5.12}$$

where it should be noted that V_X and V_D are in general not diagonal. From the above form it can be seen that the interacting spectra becomes merely scaled with respect to the non-interacting so long as the bracketed term is diagonal in the electron-hole basis. This criterion can be fulfilled for sufficiently localized interactions or un-correlated wave functions, such as the continuum.

The sum of intermediate states in our expression for the cross section (eqn. 5.3) leads to the possibility of interference effects. Because the core hole does not exist in the final state, we must coherently include terms from all possible core holes. For unit cells with only a single atom of the species of interest, this summation over all possible intermediate states is automatically included through the conservation of momentum and the formulation of the core hole as a Bloch state (eqn. 3.16). However, in cells with multiple atoms of the same species (or other species with nearby core-level resonances) it is essential to include contributions from all core-hole sites in the sum defining $|y(\omega)\rangle$ and $|x\rangle$ (eqns. 5.5 & 5.8). Neglecting this interference allows for the RIXS process to be viewed as a convolution between XAS and XES spectra:

$$\tilde{\sigma}(\omega,\omega') \propto \sum_F \sum_N \frac{|\langle F|D'|N\rangle|^2 |\langle N|D|I\rangle|^2}{\omega + E_I - E_N + i\Gamma} \delta(E_F - E_I + \omega' - \omega). \tag{5.13}$$

This decoupling has been used in previous work [116, 122].

At high excitation energies the conduction states can be considered as a continuum, and the emission spectra are insensitive to the incident photon energy. This is often referred to as incoherent RIXS, a term we will also use here, but this is misleading since the process is still coherent. Moving past the edge, contributions from incoherent emission become more dominant, leading to spectra that are uniform with respect to incident energy. In OCEAN we make the distinction between incoherent RIXS and x-ray emission spectroscopy (XES). XES is a measurement of the occupied states only. The intermediate-state effects that play such an important role in RIXS no longer contribute, and XES can be considered a type of DOS measurement — one that has been projected onto the core hole. In OCEAN XES is calculated by restricting the core-valence overlap to occupied states below the Fermi level and neglecting the initial excitation process entirely. Additionally, the final state has no core hole, so there are no interaction terms and the Hamiltonian contains only single-particle valence and core terms. In principle, relaxation effects of the $N-1$ system should be taken into account, but this is presently not done.

The appearance of incoherent RIXS occurs at energies well below the threshold at which the conduction band becomes an uncorrelated continuum, and the division is instead empirical. Both intermediate-state interference and excitonic effects are destroyed by secondary excitations or decays, and therefore a more precise term for incoherent RIXS is **k**-unselective. The secondary

excitations such as coupling to phonons or secondary electron-hole excitations can scatter the photo-electron or valence hole. This scattering decouples the photo-electron crystal momentum from that of the core hole, and therefore the response is averaged over the Brillouin zone. For RIXS, we do not properly account for incoherence, leading to disagreement at higher energies where the experimental spectra already resemble the XES while the calculated spectra continue to change and evolve with energy.

The crossover from coherent to incoherent RIXS gives information about coupling of the valence-conduction exciton to phonon and secondary electron excitations. As a first-order approximation, we will neglect secondary electron excitations such as plasmons. The important time-scales are the competition between the core-hole decay rate $1/\Gamma_\alpha$ and the phonon scattering rate $1/\Gamma_{ph}$. The phonon scattering rate can be approximated as the Debye frequency ω_D. Coherent RIXS depends on $\Gamma_\alpha \gg \omega_D$ [118]. Following the work of Eisebitt and Eberhardt [121], we will assume that single scattering is sufficient to destroy the **k**-selectivity. The fraction of RIXS events resulting in the XES step before phonon or secondary electron scattering can be given by

$$f_{coh} = \frac{\Gamma_\alpha}{\Gamma_\alpha + \Gamma_c}. \tag{5.14}$$

The phonon scattering rate is a function of both energy and momentum, but we will approximate it as a constant.

In the next section all three of these effects, coherence, interference, and excitonic interactions, will be looked at in the context of the carbon K edge in diamond.

5.4 Diamond — C K edge

We investigated the carbon K edge of diamond as a prototype system for RIXS using the experimental lattice constant of 3.57 Å. RIXS at the carbon K edge in diamond has been the subject of numerous experimental and some theoretical studies [123, 125, 126]. For RIXS, the relative positioning of the valence and conduction bands is quite important, and so parameters were used to correct the band gap and dispersion. The XAS and XES of diamond are shown in figure 5.1. In the XAS experiment, a pre-edge excitation at 285 eV is located near the valence band maximum and could be due to impurity states. A scissor operator was used to correct the DFT band gap

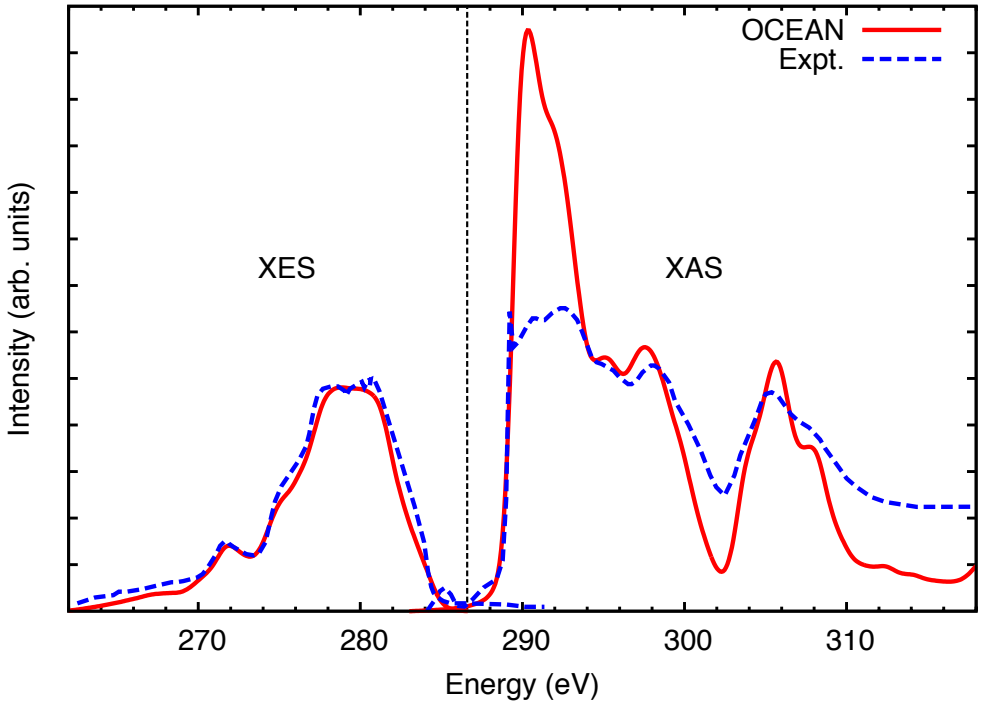

Figure 5.1: The near-edge XES and XAS of the carbon K edge in diamond compared to experiment [123]. The band gap is evident between the top of the XES at 284 eV and the onset of the XAS. The strong overestimation of the excitonic features in diamond (290-4 eV) are typical of BSE calculations [6, 124]. The conduction and valence band widths have been stretched to better match experiment, providing an *ad hoc* self-energy correction.

of 4.2 eV to the experimental value of 5.5 eV, and the valence and conduction band dispersions were stretched by 5% and 15% respectively to match the observed width and peak positions of the experimental XAS and XES. While this is inherently less satisfying than *ab initio* self-energy corrections, it helps to isolate shortcomings of the DFT from the rest of our RIXS calculations. With the simple stretching we see good agreement for peak positions, but the excitonic excitation in the XAS calculation is much too strong, as was found in previous BSE calculations [6, 124]. For the x-ray emission we find good agreement between OCEAN and experiment.

We calculated RIXS of diamond for a range of energies within the first 40 eV of the carbon K edge. The emission spectra in diamond is strongly dependent on the incident photon energy as can be seen in the RIXS maps (figs. 5.4 and 5.5). These maps were constructed by calculating the RIXS for incident energies in 0.1 eV steps. Computational work allows us to make a number

of non-physical changes to our spectra to help understand the origin of different features in the experimental data. Namely, we are interested in separating out excitonic and excited-state effects from those that arise from the band structure alone.

We have compared our calculations to experimental results for a number of different incident energies as shown in figure 5.2. The strong discrepancy between calculated and experimental spectral weight of the absorption near the edge (289-294 eV in fig. 5.1) necessitated an arbitrary scaling of the calculated results between energy points when comparing individual slices to experiment. The alignment of the calculated spectra was done as shown in the plots of the XAS and XES (fig. 5.1). We find reasonable agreement between theory and experiment, though the experimental data shows significant contributions from the incoherent or **k**-unselective RIXS. This is most obvious at the highest incident energy shown (317.2 eV) where the experimental spectrum shows good agreement with the calculated fully non-resonant XES (as in fig. 5.1) or the calculated RIXS at a higher energy (334.9 eV), but poorer agreement with the theoretical RIXS at the correct incident energy.

Figure 5.2 also shows the effects of the final-state, valence-band excitonic interactions. In general, the inclusion of interactions has a small effect on the calculated spectra, in contrast to optical/UV calculations using the same framework in which such interactions play a large role, see for instance reference 8. For most of the calculated incident energies, the inclusion of final-state interactions shifts weight slightly up in energy, reflecting a small electron-hole binding energy. Due to the small effect and high computational cost of calculating the interacting final state, the RIXS maps for diamond are calculated using the non-interacting H_0^v.

With a relatively long-lived core hole, we expect coupling to secondary excitations during the intermediate excited state. Neglecting these terms, the agreement between OCEAN and experiment is promising, but mediocre, especially at higher energies. Diamond has very strong phonon coupling, with a Debye temperature of 1860 K [127], giving a scattering rate of 0.16 eV. Based on our estimate of the phonon scattering rate, we approximate the coherent fraction as 45%. For comparison, an incoherent contribution of approximately 60% has been estimated from experiment [126]. Using the 334.9 eV incident energy calculation as representative of incoherent RIXS and taking care to control for the strength of the absorption, the coherent and incoherent RIXS can mixed as is shown in figure 5.3. The inclusion of **k**-unselective RIXS improves agreement

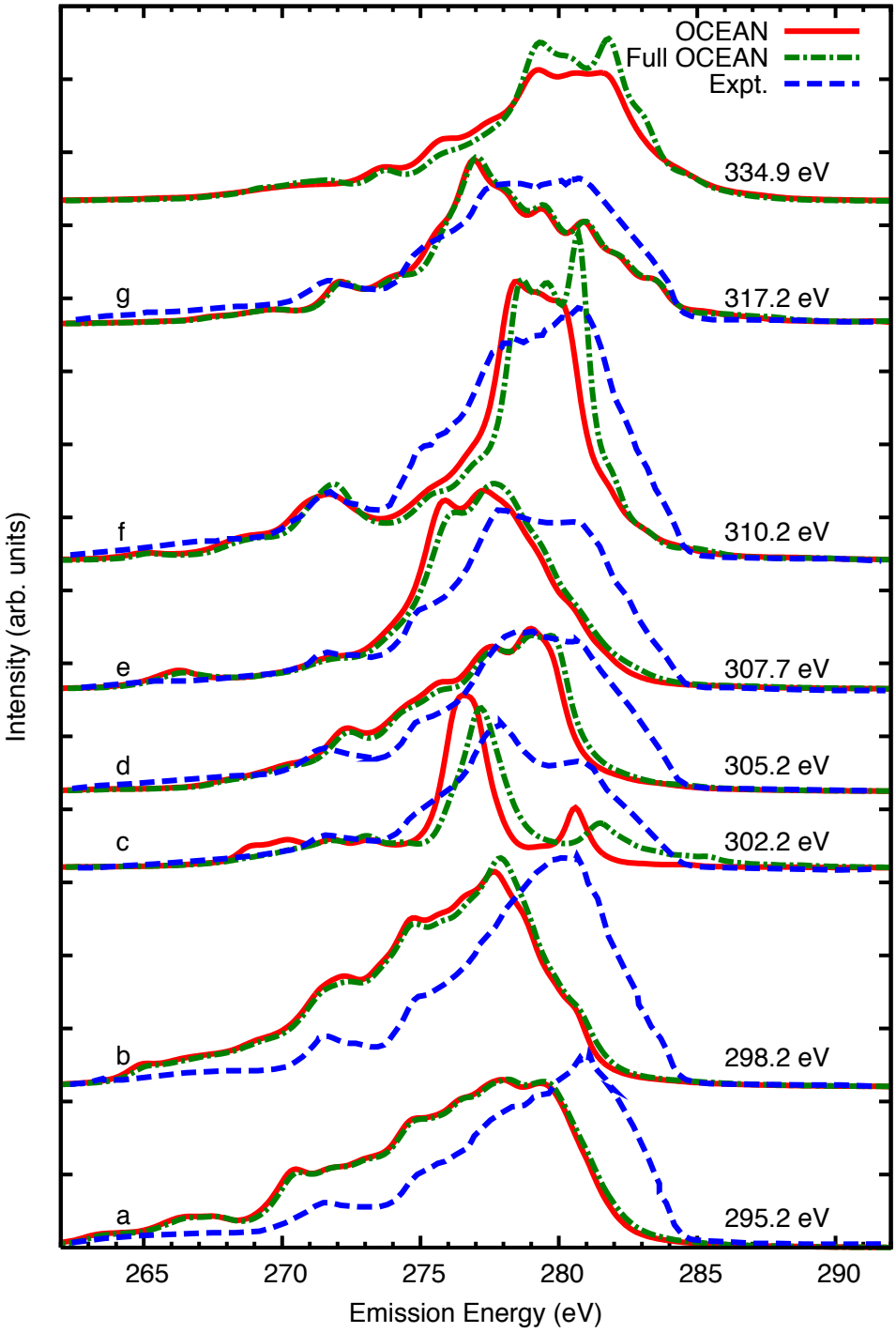

Figure 5.2: RIXS of diamond for several different incident energies compared with experiment [123]. The absolute energies of the incident x-ray photon were aligned by matching the XAS as in figure 5.1. Theoretical spectra are shown including both the intermediate and final state excitonic effects (Full OCEAN) as well as neglecting the final, valence-band exciton (OCEAN). For comparison the XAS is shown above on the facing plot.

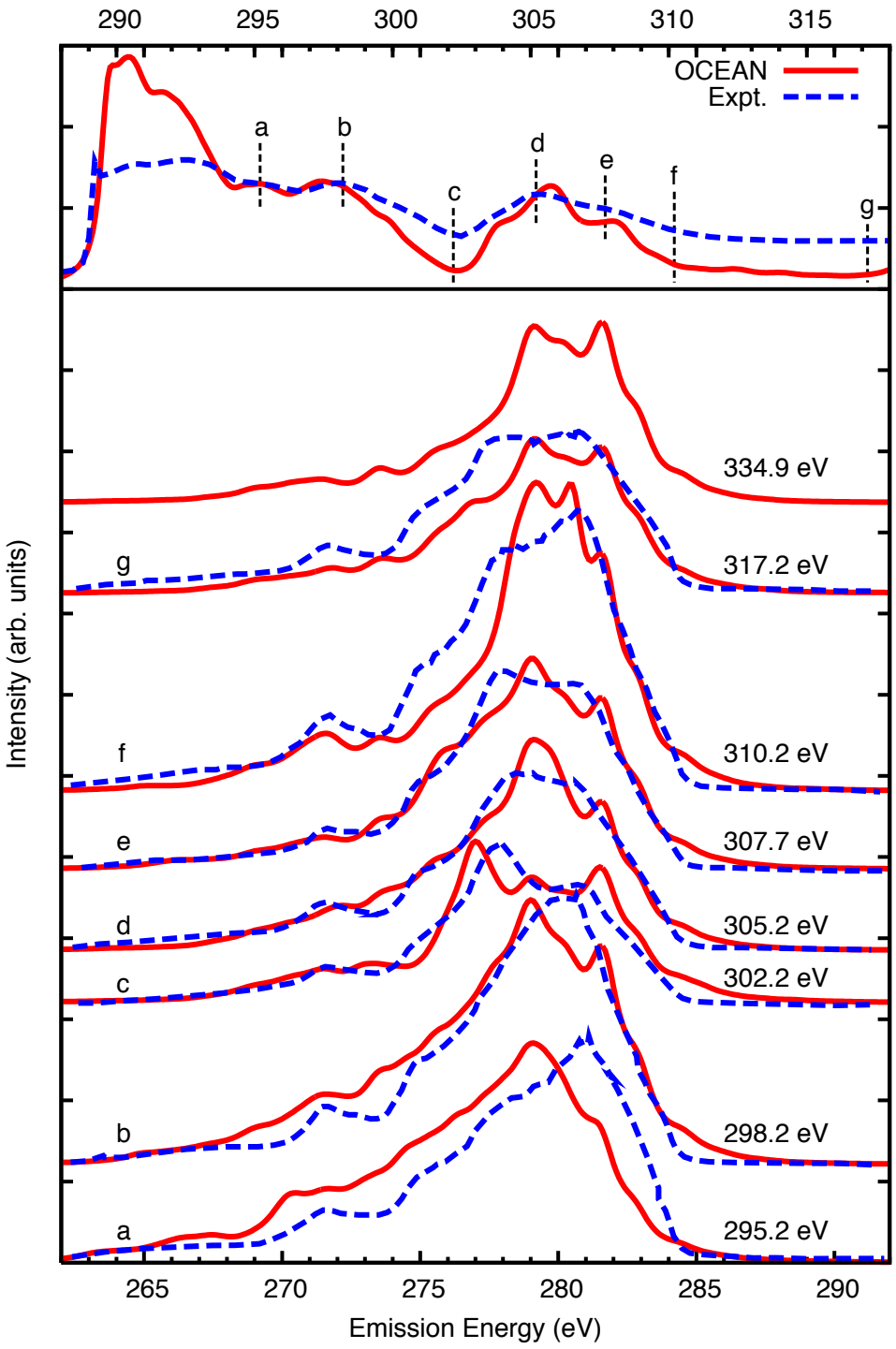

Figure 5.3: RIXS of diamond for several different incident energies including incoherent contributions compared with experiment [123]. The absolute energies of the incident x-ray photon were aligned by matching the XAS as in figure 5.1. The calculated spectra include both intermediate and final-state excitonic effects. In the top inset, the XAS of diamond is shown, marking the location of the RIXS slices.

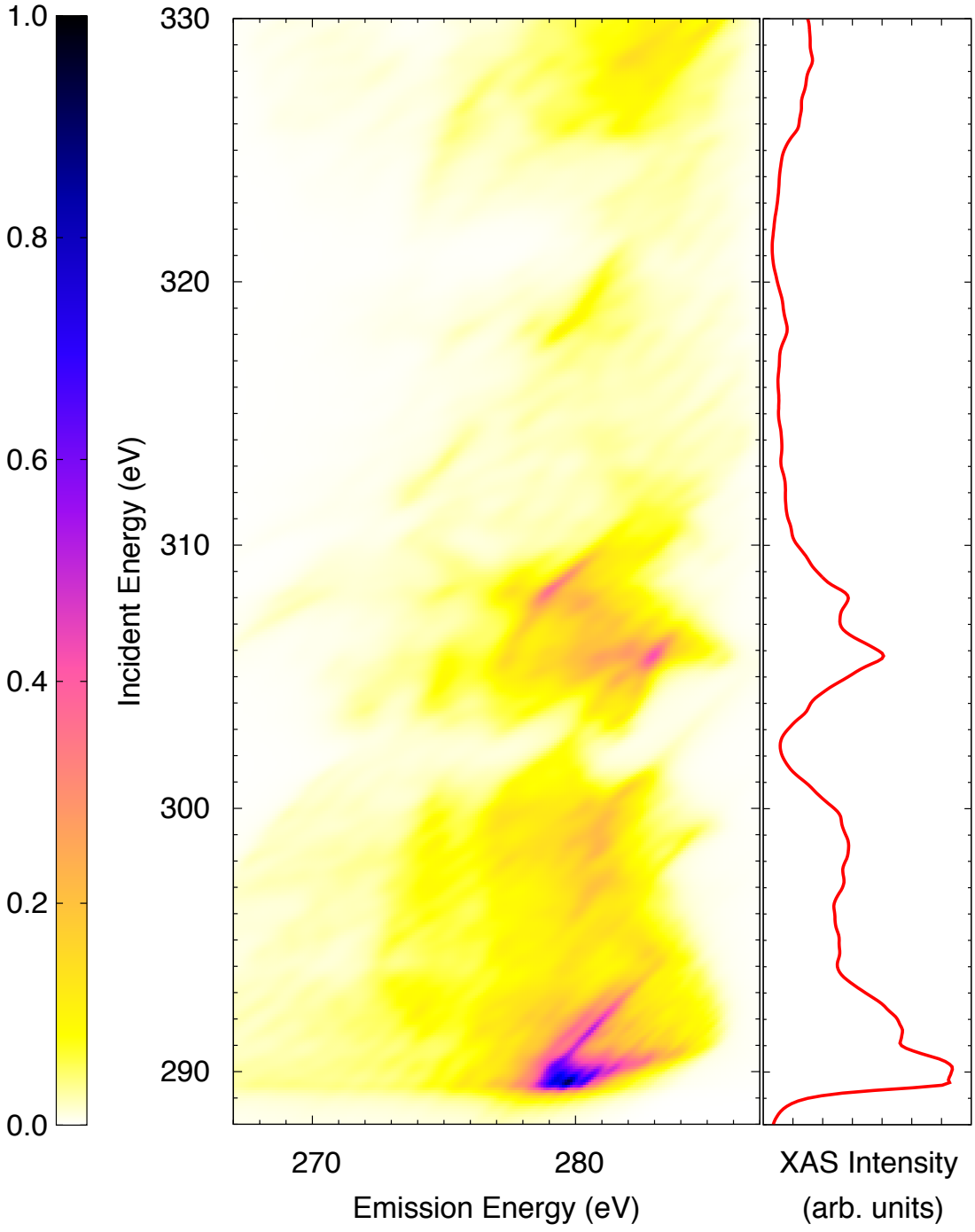

Figure 5.4: Calculated RIXS map of the carbon K edge in diamond, including interactions in the intermediate state. The z-axis shows the emitted photon intensity in arbitrary units according to the color scale on the left. On the right is the absorption determined by integrating over the emission energy.

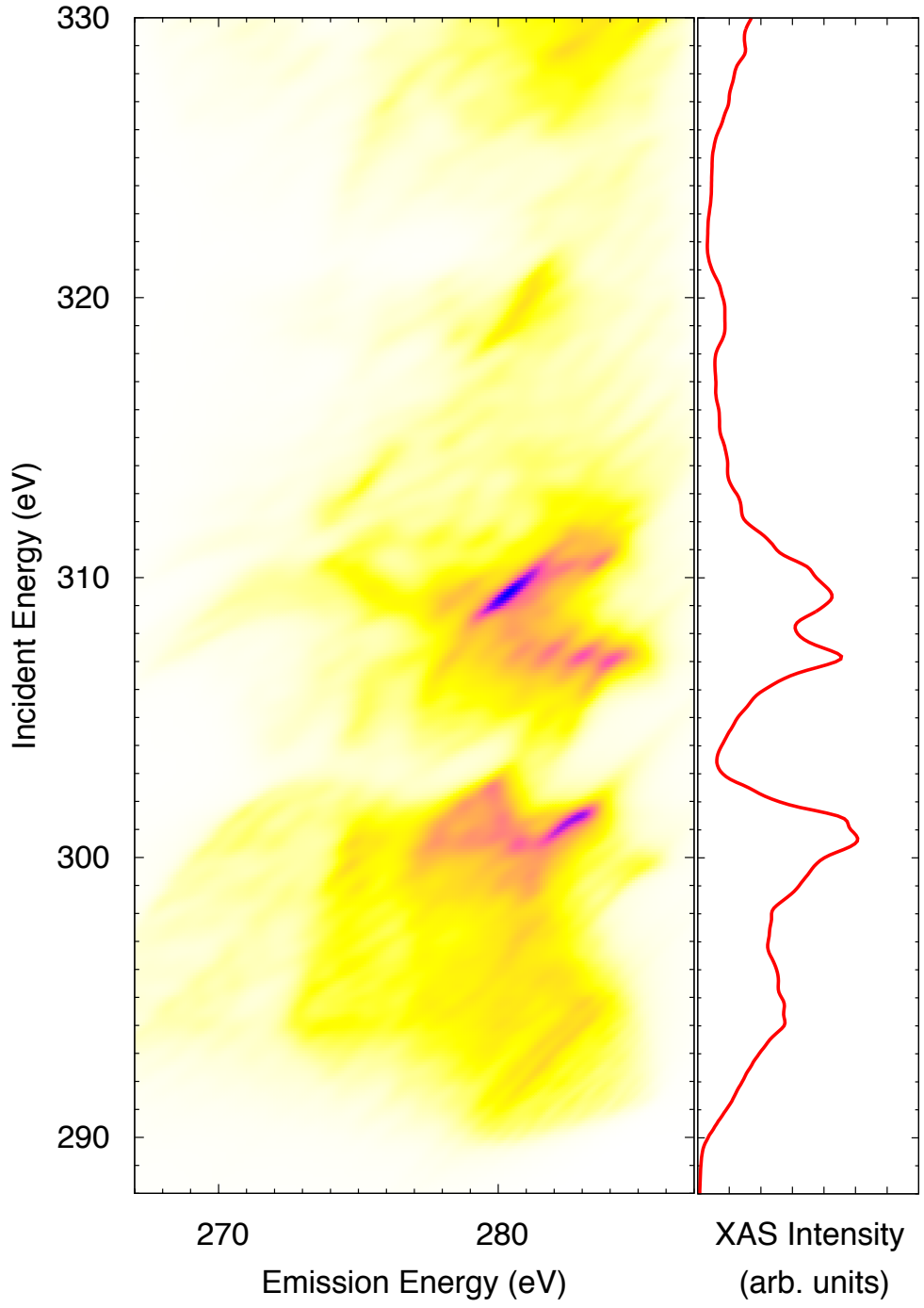

Figure 5.5: Calculated, non-interacting RIXS map of the carbon K edge in diamond. The intensity is on the same scale as the facing figure. Without intermediate-state interactions the absorption spectrum (shown on the right) shifts up in energy and shows no strong excitonic peak. Above ≈305 eV, however, the non-interacting and interacting spectra appear largely the same.

with experiment, though the model used to determine relative contributions is quite crude.

We also compare the results of our calculation including intermediate-state excitonic effects to that of a calculation done neglecting these effects as shown in figures 5.4 and 5.5 respectively. To simplify this discussion we have neglected valence-band excitonic effects in the final state, which in general shift weight towards a lower energy loss for a given incident energy. The inclusion of core-hole effects leads to the formation of a strong exciton at the edge, approximately 290 eV incident energy. We see that near the XAS edge the RIXS are strongly influenced by core-hole interactions, but that at higher energies, above 300 eV, the trends between interacting and non-interacting are quite similar. From this agreement, it seems reasonable to extract ground-state band structure from RIXS data, but caution is need at the near-edge where strong excitonic effects might hinder the analysis.

In figure 5.6 we see the effects of neglecting interference effects between the two carbon atoms in the diamond unit cell in our RIXS calculations. As can be seen, the interference effects are relatively large and lead to a shift of spectral weight, reducing the response at the near-edge below 300 eV and increasing the higher region between 300 and 310 eV. This is consistent with correcting the discrepancies seen between the OCEAN calculation of the XAS of diamond and experiment, pointing to a possible source of error in comparing fluorescence measurements of the absorption. The calculation of XAS within OCEAN treats the excited state with a core hole as the final state, and hence the precise core-hole site is measured and no interference is allowed. Though not shown, dipole limit NIXS studies of diamond give similar, though lower resolution, results to the fluorescence-determined XANES reproduced here [128]. Approaches that decouple the XAS and XES components of RIXS will fail to accurately account for the observed rearrangement of spectral weight in the near-edge region [122, 129, 130]. While the inclusion of before-mentioned decoherence effects will reduce the importance of the interference on the observed spectra, strong rearrangement of spectral weight is observed in the near-edge region and is expected to have a significant effect.

Diamond highlights the interplay between several effects in RIXS. The relatively long carbon 1*s* core-hole lifetime and strong electron-phonon coupling in diamond increases the importance of intermediate-state scattering events, which at present are only included in a very approximate fashion. An electron-phonon interaction term added to the Hamiltonian would allow for scatter-

ing of the intermediate state. In this way **k**-unselective RIXS would be mixed in by building in momentum transfer to a phonon bath. Interference effects between the two carbon sites have a strong influence on the calculated spectra, and should be included.

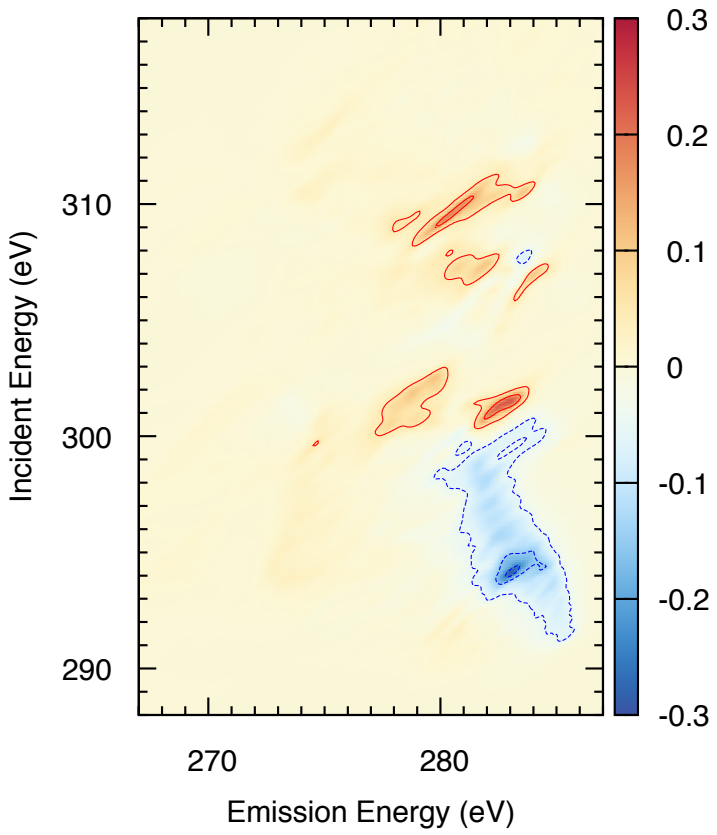

Figure 5.6: The effect of interference between the two carbon site in the RIXS of diamond. The plot shows the intensity map of correctly calculated RIXS for diamond minus a calculation done without interference effects in the intermediate state. The blue areas, almost entirely below excitations of 300 eV, designate areas where the inclusion of interference effects leads to a decrease in the strength of RIXS signal. The z-scale here has the same overall scaling as the previous RIXS maps of diamond, and hence the extreme contours of ± 0.25 are approximately 25% of the maximum intensity of the calculation. Solid contour lines are placed at 0.05, 0.15, and 0.25 while dashed contours are placed at the corresponding negatives.

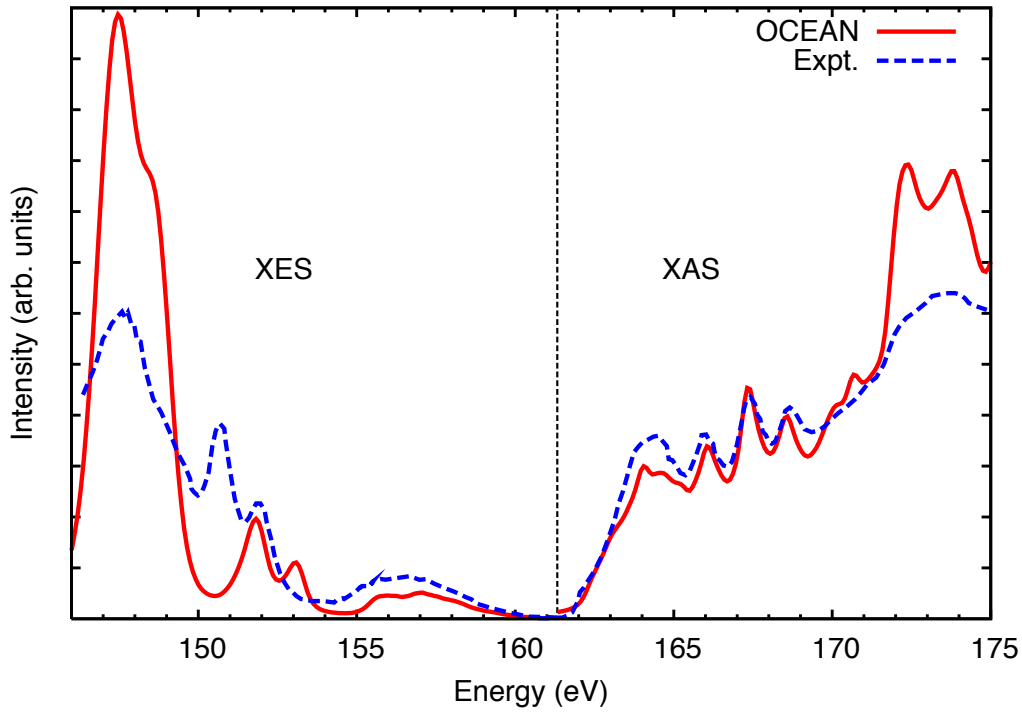

Figure 5.7: The near-edge XES and XAS of the sulfur $L_{2,3}$ edge in CdS compared to experiment [131]. In OCEAN the Cd *4d* states are too shallow by 1.5 eV. An *ad hoc* energy-dependent Gaussian broadening has been added to the calculated XES, though the broadening of the S *3s* states is still understated.

5.5 CdS — S $L_{2,3}$ edge

We have also calculated the resonant emission from the sulfur $L_{2,3}$ edge in wurtzite CdS. CdS has technological applications as a building block for light-emitting diodes [132] or photo-voltaic cells [133]. For both of these applications the alignment and structure of valence and low-lying conduction bands are determining factors of real-world device performance and efficiency. Emission from the sulfur *2p* core states has overlap with both *s*-type hybridized states in the valence band as well as the deeper-bound Cd *4d* and S *3s* states. Previous calculations of CdS RIXS have used a non-interacting formalism that neglects both intermediate-state interactions and interference effects [131, 134]. While band-structure effects are the dominate feature in RIXS, inherent in the matrix elements between the conduction or valence bands and the core hole, neglecting intermediate-state excitonic effects and core-hole dynamics fails to give quantitative agreement between theory and experiment.

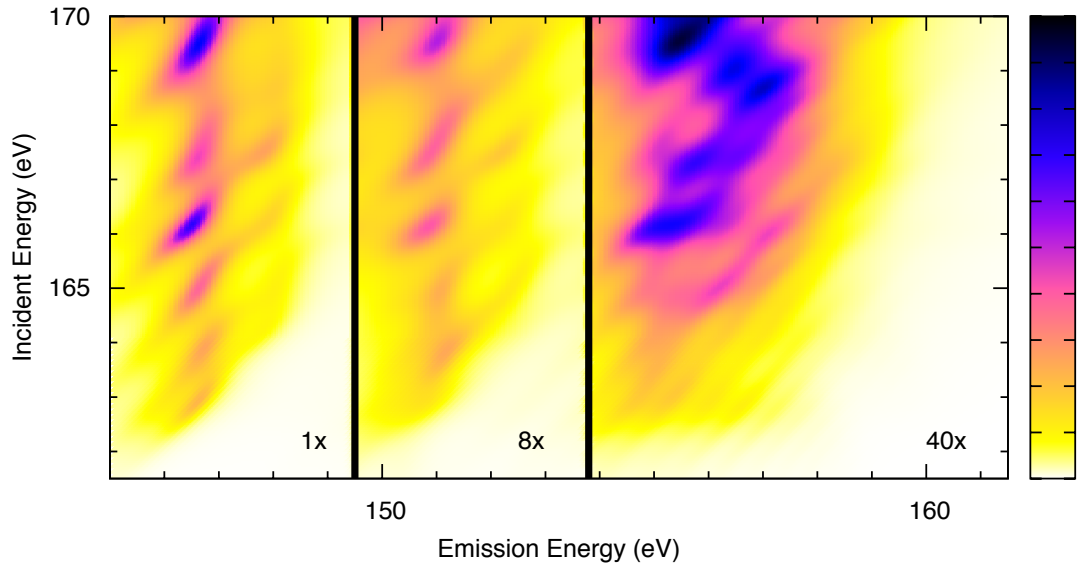

Figure 5.8: The calculated RIXS map of the sulfur $L_{2,3}$ edge in CdS. The spectrum has been rescaled to allow for the details of the valence-band RIXS to be seen.

For our calculation we used a **k**-space sampling of $12\times12\times8$ and a cadmium psuedopotential that included *4s* and *4p* states as valence. The semi-core pseudopotential necessitated an energy cutoff of 124 Ha. Previous DFT calculations of CdS have shown that the *4d* electrons are under bound within the LDA [131, 135, 136]. In the present work this is manifest by the Cd *4d* states appearing at approximately 152 eV in the emission spectra in contrast to their experimental position of 150.5 eV. At present no adjustment is made to correct for this, though self-energy corrections have been shown to improve agreement with experiment [137].

Calculations of the sulfur $L_{2,3}$ absorption and emission are shown in figure 5.7 with comparison to experiment. We see good agreement with experiment for the XAS for the alignment of features though some spectral weight is missing right at the edge. The XES shows three distinct contributions, all of which are doubled by the 1.2 eV spin-orbit splitting of the sulfur *2p* states; S *3s*, Cd *4d*, and valence states arising from hybridization of the Cd *5s* with the S *3p*. The beforementioned shift in the binding energy of the Cd *4d* is also quite evident in the calculation, as is a lack of broadening in the calculated S *3s* states arising from unaccounted for self-energy effects.

The strength of transition from the Cd *4d* is exaggerated in the experiment since both are sitting on the tail of the S *3s*.

The primary features of the CdS RIXS (fig. 5.8) are the constant emission lines from the S *3s* and Cd *4d* states. These show Stoke's shifts from the finite intermediate-state lifetime used in the calculation. This is not apparent in the experimental data due to final-state broadening effects. The experimental measurement of the valence band RIXS (emission between 154-160 eV), shows very little dispersion, pointing to a large contribution from the incoherent RIXS. Previous calculations show strong features missing in our calculation [134]. This most likely is due to difference in calculation method as previous work neglected excitonic effects of the core hole.

5.6 Conclusions

The calculation of direct RIXS is a straightforward extension of the OCEAN package, and, as for absorption or non-resonant scattering calculations, we are able to investigate the RIXS of systems with spin-orbit splitting in the core states. The partitioning of **k**-selective versus unselective contributions, however, needs improvement. Specifically, the phonon coupling can be sensitive to the nature of the photo-electron, and hence dependent on the initial excitation energy and symmetry of the intermediate-state exciton. The large fraction of measured spectra that appears to arising from incoherent RIXS precludes an honest assessment of agreement with experiment until a more quantitative and accurate estimation of the decoherence is calculated.

Chapter 6
CONCLUSIONS

We have demonstrated a method for calculating near-edge x-ray spectroscopy based on the Bethe-Salpeter Equation. Though the principles of using this approach for *ab initio* spectroscopy calculations have been well understood for many years [57], there is no widely available computational framework for such calculations. The strength of a DFT + GW + BSE method lies in its lack of free adjustable parameters. The creation of the OCEAN code relied heavily on previous work by Shirley and collaborators [3, 6, 38, 53, 72], but extends that work by including a complex self-energy and self-consistent *G*W calculations of electron wave functions and energies. The OCEAN package unifies atomic multiplet and extended-state effects into a single framework, allowing accurate calculations across a wide range of materials. Additionally, the code can be run using a unified input file, specifying only the physical parameters of the system in question, i.e., lattice constants, atomic positions, and the probe details. In this we hope to make BSE calculations more accessible to the broader scientific community.

In this dissertation I presented the OCEAN code which includes several extensions beyond previous work in the field. The first is the inclusion of *GW* self-energy effects within several different approximations, primarily the many-pole self-energy technique [46]. The effect of this term is to add energy dependent broadening and stretching to the final spectra, improving agreement with experiment as was shown in the fluorine K edge of LiF (fig. 4.1). We also showcased the effects of self-consistent *GW* calculations which provide a correction to the limitations of DFT. OCEAN allows for spin-dependence in the ground state, and we showed examples of ferromagnetic systems such as metallic iron, cobalt, and nickel.

There remain several short-term and long-term issues that should be addressed in future work. Along with a brief discussion some of these are listed below:

— With full spin-dependence there is the option of extending the x-ray absorption operator to the relativistic operator, allowing the calculation of x-ray magnetic circular dichromism

(XMCD). In XMCD the electron polarization with respect to its propagation leads to the preferential flip up or down of the excited electron's spin. By providing an external magnetic field to align the spin of ferromagnetic materials, XMCD can be used as a proxy measurement of the majority or minority spin states, especially at the $L_{2,3}$ edge.

— The extension of our screening calculation to higher-order multipole terms is straightforward. This is of importance to less uniform systems, such as layered geometries, surfaces, or molecular systems.

— The limitation of static screening remains poorly explored, as does the effect of only considering RPA level response in calculating χ^0. Dynamical screening effects would require an energy-dependent Hamiltonian, though such a system could easily be solved in a similar manner to the determination of excitonic states in RIXS calculations as outlined in chapter 5. While valence-band BSE-level calculations of the dielectric response are common, they are primarily done in the long wavelength limit, and such an endeavor would require the response at many different values of $\mathbf{q}$.

— Coupling to secondary excitations such as phonons or charge-transfer excitations can be added through the cumulant technique which efficiently treats non-interfering, bosonic excitations through their spectral functions. Methods to calculate phonon spectral functions are available, but charge-transfer excitations are still treated as fitted models.

The OCEAN code pushes the boundaries of *ab initio* near-edge x-ray calculations, providing quantitative agreement for a range of condensed matter systems. While its use requires some familiarity with DFT, the barrier to entry for OCEAN is reasonably small.

Appendix A
OCEAN DETAILS

A.1 OCEAN workflow

The OCEAN code runs in several stages, each in its own working directory. These are as follows:

1. *Setup and parsing stage.* The code creates a directory called `Common` and populates it with information from the input file. Any unspecified inputs are filled with available default values if appropriate.

2. *DFT or ABINIT stage.* Here three separate DFT runs are performed. All the information needed to perform the DFT calculations was parsed during the setup stage. Initially a self-consistent density is calculated, and then wave functions are calculated for both the BSE and screening.

3. *Preparation stage.* An intermediate step is performed between the DFT stage and all following steps. This is primarily to ensure that the code remains portable. New or alternative methods for calculating the wave functions can be inserted into OCEAN so long as a new DFT script is created to create an input from the information in the `Common` directory and the preparation stage is modified to parse the new output files.

4. *Atomic stage.* The atomic calculation calculates the core-hole wave function and spin-orbit splitting. It also creates the localized PAW basis and pre-tabulates the direct and exchange interactions between this basis and the core-hole wave function.

5. *Screening stage.* The screening step performs the RPA calculation and inverts the response function to calculate the core-hole screening. The sum over Kohn-Sham orbitals used in this calculation is done on a much sparser **k**-mesh than the later BSE calculations but requires a larger number of bands. For this reason a separate calculation of wave functions is done for the Screening and BSE stages.

6. *BSE stage.* The final stage solves for the spectrum by approximating the resolvent in equation 3.13.

In figure A.1 a flowchart of the OCEAN package is shown with calculated quantities referenced to appropriate equations.

A.2 Approximating the resolvent

For the absorption cross-section (eqn. 3.13) or the excitonic wave function (eqn. 5.5) a method of inverting the BSE Hamiltonian is necessary. In calculating the spectrum, the actual eigenvalues of the Hamiltonian are not of interest, and we want a method capable of quickly giving the whole, energy-dependent spectrum. For this the Haydock method [7, 138] is quite suitable, the the core-hole lifetime providing a convenient a physical broadening, preventing singularities. The Haydock method can be thought of as an Nth-order extension of the Sternheimer equation, which was developed to solve for the polarizability by expressing the perturbed, excited-state wave function to first order in the interaction [139]. At present the Haydock method is only suitable when the action of our approximate BSE Hamiltonian is strictly real, and for $L_{2,3}$ edges where the core-hole lifetime changes with edge only an average broadening can be included.

We are, however, dealing with an excited-state system whose lifetime is finite and varying with respect to the excitation energy. To capture this we can include quasi-particle lifetimes through the imaginary component of the self-energy correction as well as *ad hoc* core-hole lifetime terms. To solve this inversion problem with complex valued terms we instead use the GMRES method [120] for approximating the excitonic wave function $|y(\omega)\rangle$ as defined in equation 5.5. Inserting the definition of $|y(\omega)\rangle$ in to our expression for the cross-section from equation 3.13 we get

$$\sigma(\omega) \propto \mathfrak{Im}\left[\langle I|d|y(\omega)\rangle\right]. \tag{A.1}$$

The GMRES method is computationally more demanding, requiring a full calculation of the excitonic wave function for each energy point in the desired final spectrum. In practice both a single exciton calculation and the full Haydock calculation require approximately 100 iterations. Further work should expand the Haydock routine to support a tri-diagonal formalism that is compatible with complex-valued energies.

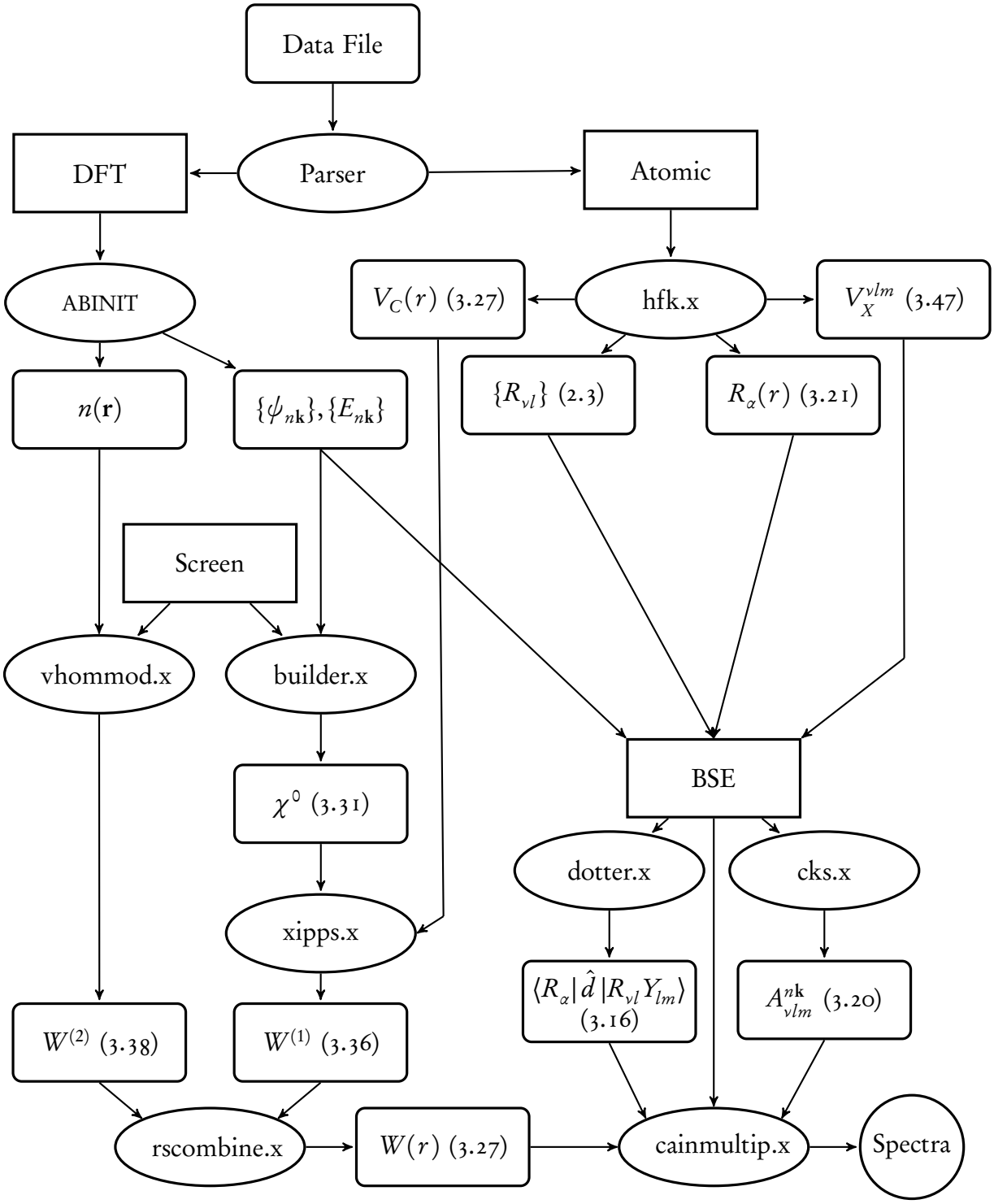

Figure A.1: Flowchart of the OCEAN package. Equations are cited for calculated quantities.

A.3 Sample Input

The required input for OCEAN is minimal, and can be divided into several sections; the physical cell, psuedopotentials, photon parameters, and convergence. In the following we will list and explain the important inputs for an OCEAN calculation of LiF. The unit cell for LiF is a rock salt structure with two atoms per unit cell. The physical parameters specify the unit cell dimensions and locations and types of atoms:

* acell { 7.597 7.597 7.597 } — The dimensions of the primitive lattice vectors in Bohr
* rprim { 0.0 0.5 0.5 0.5 0.0 0.5 0.5 0.5 0.0 } — The primitive lattice vectors, normalized by acell
* ntypat 2 — The number of unique elements in the system
* znucl { 3 9 } — The Z number of the elements
* natom 2 — The number of total atoms in the cell
* typat { 1 2 } — A list of all of the atoms in the system, referenced by ntypat
* xred { 0.5 0.5 0.5 0.0 0.0 0.0 } — The reduced coordinates of each element
* diemac 1.92 — The macroscopic dielectric constant ϵ_∞.

The details of the x-ray probe, including which site is the absorbing atom:

* nedges 1 — Run for only one edge
* edges { 2 1 0 } — This specifies $\{\alpha, n, l\}$, i.e., on which atom and which principle and angular momentum quantum number to put hole: F *1s*.

There is also a supplementing 'photon' file:

* quad — Include both E1 and M1 contributions. Other options include 'dipole' to only include E1 and 'NRIXS' to calculate non-resonant scattering

* cartesian 0 0 1 end — This specifies the polarization vector $\hat{\epsilon}$ in cartesian coordinates

* cartesian 0 1 0 end — The **q** vector of the incoming photon or the momentum transfer for NIXS

* 696 — The approximate edge energy in eV, which is used to calculate the magnitude of **q**.

The psuedopotential inputs include suitable psuedopotential files for the calculation as well as information for the PAW reconstruction:

* cnbse.rad 4.0

The 'paw.fill' file contains the following lines that govern the PAW construction:

* 2 — The maximum angular momentum of the PAW basis

* -0.30 2.00 0.0001 0.01 4 — The first two digits are the minimum and maximum energy range to test the fidelity of the PAW. The third determines the tolerance between the all-electron and PAW-reconstructed pseudo wave functions. The next determines the precision of the solution to the radial Schrödinger equation (eqn. 2.3). The fifth determines the number of test points for diagnostics

* 3.0 — Sets the PAW reconstruction radius

* 0.05 20 — Sets the spacing and q_{max} of the Fourier grid for determining the projectors (eqn. 2.4).

The 'paw.fill' file contains information about the pseudopotential:

* 9 — The Z of the atom of interest, in this case fluorine

* 1 0 0 0 — The number of occupied core levels for each l: s, p, d, and f

* scalar rel lda — The treatment of the relativistic corrections and the type of exchange-correlation potential

* 2.0 4.5 0.25 0.0 — The valence level occupation numbers for each l.

Finally, the input file also includes numerical convergence parameters:

* ecut 100 — The energy cutoff used by the plane wave DFT code

* nkpt { 10 10 10 } — The **k**-mesh used for calculating the wave functions for the BSE

* nband 80 — Number of bands to include in the BSE

* paw.nkpt { 2 2 2 } — The **k**-mesh used for calculating χ^0 (eqn. 3.31)

* paw.nbands 400 — The number of bands to include in the calculation of χ^0.

VITA

John Vinson spent most of his childhood in Tulsa, OK and graduated from Booker T. Washington high school in 2003. He earned a B.S. from Yale University in 2007 and entered immediately into the University of Washington where he earned his Ph.D. in Physics in 2012.

BIBLIOGRAPHY

[1] J. J. Rehr and R. C. Albers, Rev. Mod. Phys. **72**, 621 (2000).

[2] J. Vinson, J. J. Rehr, J. J. Kas, and E. L. Shirley, Phys. Rev. B **83**, 115106 (2011).

[3] E. L. Shirley, Ultramicroscopy **106**, 986 (2006).

[4] R. Laskowski and P. Blaha, Phys. Rev. B **82**, 205104 (2010).

[5] W. Olovsson, I. Tanaka, P. Puschnig, and C. Ambrosch-Draxl, J. Phys: Cond. Matter **21**, 104205 (2009).

[6] E. L. Shirley, Phys. Rev. Lett. **80**, 794 (1998).

[7] L. X. Benedict and E. L. Shirley, Phys. Rev. B **59**, 5441 (1999).

[8] H. M. Lawler, J. J. Rehr, F. Vila, S. D. Dalosto, E. L. Shirley, and Z. H. Levine, Phys. Rev. B **78**, 205108 (2008).

[9] J. J. Rehr, J. J. Kas, F. D. Vila, M. P. Prange, and K. Jorissen, Phys. Chem. Chem. Phys. **12**, 5503 (2010).

[10] M. Taillefumier, D. Cabaret, A.-M. Flank, and F. Mauri, Phys. Rev. B **66**, 195107 (2002).

[11] A. L. Ankudinov, A. I. Nesvizhskii, and J. J. Rehr, Phys. Rev. B **67**, 115120 (2003).

[12] A. L. Ankudinov, Y. Takimoto, and J. J. Rehr, Phys. Rev. B **71**, 165110 (2005).

[13] F. M. F. de Groot, Coord. Chem. Rev. **249**, 31 (2005).

[14] H. Ikeno, T. Mizoguchi, and I. Tanaka, Phys. Rev. B **83**, 155107 (2011).

[15] P. S. Miedema, H. Ikeno, and F. M. F. de Groot, J. Phys.: Condens. Matter **23**, 145501 (2011).

[16] K. Gottfried and T.-M. Yan, *Quantum Mechanics: Fundamentals* (Springer, 2004).

[17] P. Hohenberg and W. Kohn, Phys. Rev. **136**, B864 (1964).

[18] W. Kohn and L. J. Sham, Phys. Rev. **140**, A1133 (1965).

[19] E. Wigner, Phys. Rev. **46**, 1002 (1934).

[20] J. P. Perdew and Y. Wang, Phys. Rev. B **45**, 13244 (1992).

[21] J. P. Perdew and A. Zunger, Phys. Rev. B **23**, 5048 (1981).

[22] D. C. Langreth and M. J. Mehl, Phys. Rev. B **28**, 1809 (1983).

[23] A. D. Becke, Phys. Rev. A **38**, 3098 (1988).

[24] J. P. Perdew, J. A. Chevary, S. H. Vosko, K. A. Jackson, M. R. Pederson, D. J. Singh, and C. Fiolhais, Phys. Rev. B **46**, 6671 (1992).

[25] J. P. Perdew, K. Burke, and M. Ernzerhof, Phys. Rev. Lett. **77**, 3865 (1996).

[26] D. R. Bowler and T. Miyazaki, Rep. Prog. Phys. **75**, 036503 (2012).

[27] X. Gonze, G.-M. Rignanese, M. Verstraete, J.-M. Beuken, Y. Pouillon, R. Caracas, F. Jollet, M. Torrent, G. Zerah, M. Mikami, et al., Zeit. Kristallogr. **220**, 558 (2005).

[28] X. Gonze, B. Amadon, P.-M. Anglade, J.-M. Beuken, F. Bottin, P. Boulanger, F. Bruneval, D. Caliste, R. Caracas, M. Côté, et al., Comput. Phys. Commun. **180**, 2582 (2009).

[29] The ABINIT code is a common project of the Université Catholique de Louvain, Corning Incorporated, and other contributors (URL http://www.abinit.org).

[30] G. B. Bachelet, D. R. Hamann, and M. Schlüter, Phys. Rev. B **26**, 4199 (1982).

[31] D. R. Hamann, M. Schlüter, and C. Chiang, Phys. Rev. Lett. **43**, 1494 (1979).

[32] N. Troullier and J. L. Martins, Phys. Rev. B **43**, 1993 (1991).

[33] L. Kleinman and D. M. Bylander, Phys. Rev. Lett. **48**, 1425 (1982).

[34] E. Luppi, H.-C. Weissker, S. Bottaro, F. Sottile, V. Veniard, L. Reining, and G. Onida, Phys. Rev. B **78**, 245124 (2008).

[35] URL `http://opium.sourceforge.net`.

[36] P. E. Blöchl, Phys. Rev. B **50**, 17953 (1994).

[37] S. Kotochigova, Z. H. Levine, E. L. Shirley, M. D. Stiles, and C. W. Clark, Phys. Rev. A **55**, 191 (1997).

[38] E. L. Shirley, J. Electron Spectrosc. Rel. Phenom. **136**, 77 (2004).

[39] L. Hedin, Phys. Rev. **139**, A796 (1965).

[40] L. Hedin and S. Lundqvist, *Solid State Physics* (Academic, 1969), vol. 23.

[41] M. S. Hybertsen and S. G. Louie, Phys. Rev. B **34**, 5390 (1986).

[42] B. I. Lundqvist, Phys. Kondens. Mater. **6**, 206 (1967).

[43] G. Cappellini, R. Del Sole, L. Reining, and F. Bechstedt, Phys. Rev. B **47**, 9892 (1993).

[44] G. E. Engel and B. Farid, Phys. Rev. B **47**, 15931 (1993).

[45] W. von der Linden and P. Horsch, Phys. Rev. B **37**, 8351 (1988).

[46] J. J. Kas, A. P. Sorini, M. P. Prange, L. W. Cambell, J. A. Soininen, and J. J. Rehr, Phys. Rev. B **76**, 195116 (2007).

[47] E. E. Salpeter and H. A. Bethe, Phys. Rev. **84**, 1232 (1951).

[48] A. L. Fetter and J. D. Walecka, *Quantum theory of many-particle systems* (McGraw-Hill, 1971).

[49] S. L. Adler, Phys. Rev. **126**, 413 (1962).

[50] N. Wiser, Phys. Rev. **129**, 62 (1963).

[51] I. Sloan and R. Womersley, Adv. Comput. Math. **21**, 107 (2004).

[52] Z. H. Levine and S. G. Louie, Phys. Rev. B **25**, 6310 (1982).

[53] E. L. Shirley, J. A. Soininen, and J. J. Rehr, Physica Scripta **T115**, 31 (2005).

[54] J. J. Rehr, J. J. Kas, F. D. Vila, M. P. Prange, and K. Jorissen, Phys. Chem. Chem. Phys. **12**, 5503 (2010).

[55] E. U. Condon and G. H. Shortley, *The Theory of Atomic Spectra* (Cambridge University Press, 1963).

[56] K. Gilmore and E. L. Shirley, J. Phys.: Condens. Matter **22**, 315901 (2010).

[57] G. Onida, L. Reining, and A. Rubio, Rev. Mod. Phys. **74**, 601 (2002).

[58] R. J. Bartlett and M. Musiał, Rev. Mod. Phys. **79**, 291 (2007).

[59] E. Hudson, E. Moler, Y. Zheng, S. Kellar, P. Heimann, Z. Hussain, and D. A. Shirley, Phys. Rev. B **49**, 3701 (1994).

[60] K. Hämäläinen, S. Galambosi, J. A. Soininen, E. L. Shirley, J.-P. Rueff, and A. Shukla, Phys. Rev. B **65**, 155111 (2002).

[61] J. J. Rehr, J. A. Soininen, and E. L. Shirley, Physica Scripta **T115**, 207 (2005).

[62] U. von Barth and G. Grossmann, Phys. Rev. B **25**, 5150 (1982).

[63] A. A. Lavrentyev, B. V. Gabrelian, I. Y. Nikiforov, and J. J. Rehr, J. Phys. Chem. Solids **60**, 787 (1999).

[64] W. L. O'Brien, J. Jia, Q.-Y. Dong, T. A. Callcott, J.-E. Rubensson, D. L. Mueller, and D. L. Ederer, Phys. Rev. B **44**, 1013 (1991).

[65] R. D. Leapman and L. A. Grunes, Phys. Rev. Lett. **45**, 397 (1980).

[66] J. Schwitalla and H. Ebert, Phys. Rev. Lett. **80**, 4586 (1998).

[67] P. Krüger and C. R. Natoli, Phys. Rev. B **70**, 245120 (2004).

[68] P. Krüger, Phys. Rev. B **81**, 125121 (2010).

[69] R. W. G. Wyckoff, *The Structure of Crystals: Supplement for 1930-1934 to the Second Edition* (Reinhold, 1935).

[70] N. W. Ashcroft and N. D. Mermin, *Solid State Physics* (Brooks Cole, 1976).

[71] J. Fink, T. Müller-Heinzerling, B. Scheerer, W. Speier, F. U. Hillebrecht, J. C. Fuggle, J. Zaanen, and G. A. Sawatzky, Phys. Rev. B **32**, 4899 (1985).

[72] E. L. Shirley, J. Electron Spectrosc. Rel. Phenom. **144-147**, 1187 (2005).

[73] J. C. Woicik, E. L. Shirley, C. S. Hellberg, K. E. Andersen, S. Sambasivan, D. A. Fischer, B. D. Chapman, E. A. Stern, P. Ryan, D. L. Ederer, et al., Phys. Rev. B **75**, 140103 (2007).

[74] H. Ikeno, F. M. F. de Groot, E. Stavitski, and I. Tanaka, J. Phys.: Condens. Matter **21**, 104208 (2009).

[75] P. Krüger, Journal of Physics: Conference Series **190**, 012006 (2009).

[76] S. Tinte and E. L. Shirley, J. Phys.: Condens. Matter **20**, 365221 (2008).

[77] F. M. F. de Groot, J. Electron Spectrosc. Rel. Phenom. **67**, 529 (1994).

[78] M. Gatti, F. Bruneval, V. Olevano, and L. Reining, Phys. Rev. Lett. **99**, 266402 (2007).

[79] A. Scherz, *Spin-dependent X-ray Absorption Spectroscopy of 3d Transition Metals: Systematics and Applications* (Ph.D. thesis, Freie Universität Berlin, 2003).

[80] M. W. Haverkort, Z. Hu, A. Tanaka, W. Reichelt, S. V. Streltsov, M. A. Korotin, V. I. Anisimov, H. H. Hsieh, H.-J. Lin, C. T. Chen, et al., Phys. Rev. Lett. **95**, 196404 (2005).

[81] C. T. Chen, Y. U. Idzerda, H.-J. Lin, N. V. Smith, G. Meigs, E. Chaban, G. H. Ho, E. Pellegrin, and F. Sette, Phys. Rev. Lett. **75**, 152 (1995).

[82] C. T. Chen, N. V. Smith, and F. Sette, Phys. Rev. B **43**, 6785 (1991).

[83] A. Grechnev, I. Di Marco, M. I. Katsnelson, A. I. Lichtenstein, J. Wills, and O. Eriksson, Phys. Rev. B **76**, 035107 (2007).

[84] A. I. Nesvizhskii, A. L. Ankudinov, J. J. Rehr, and K. Baberschke, Phys. Rev. B **62**, 15295 (2000).

[85] F. Aryasetiawan, L. Hedin, and K. Karlsson, Phys. Rev. Lett. **77**, 2268 (1996).

[86] S. Kiyono, S. Chiba, Y. Hayasi, S, and S. Mochimaru, Jpn. J. Appl. Phys. **17S2**, 212 (1978).

[87] A. K. Soper, Pure Appl. Chem. **82**, 1855 (2010).

[88] M. Cavalleri, H. Ogasawara, L. Pettersson, and A. Nilsson, Chem. Phys. Lett. **364**, 363 (2002).

[89] S. Myneni, Y. Luo, L.-Å. Näslund, M. Cavalleri, L. Ojamäe, H. Ogasawara, A. Pelmenschikov, P. Wernet, P. Väterlein, C. Heske, et al., J. Phys.: Condens. Matter **14**, L213 (2002).

[90] U. Bergmann, P. Wernet, P. Glatzel, M. Cavalleri, L. G. M. Pettersson, A. Nilsson, and S. P. Cramer, Phys. Rev. B **66**, 092107 (2002).

[91] P. Wernet, D. Nordlund, U. Bergmann, M. Cavalleri, M. Odelius, H. Ogasawara, L.-Å. Näslund, T. K. Hirsch, L. Ojamäe, P. Glatzel, et al., Science **304**, 995 (2004).

[92] D. Prendergast and G. Galli, Phys. Rev. Lett. **96**, 215502 (2006).

[93] B. Hetényi, F. D. Angelis, P. Giannozzi, and R. Car, J. Chem. Phys. **120**, 8632 (2004).

[94] G. Brancato, N. Rega, and V. Barone, Phys. Rev. Lett. **100**, 107401 (2008).

[95] J. D. Smith, C. D. Cappa, K. R. Wilson, B. M. Messer, R. C. Cohen, and R. J. Saykally, Science **306**, 851 (2004).

[96] A. Nilsson, P. Wernet, D. Nordlund, U. Bergmann, M. Cavalleri, M. Odelius, H. Ogasawara, L.-Å. Näslund, T. K. Hirsch, L. Ojamäe, et al., Science **308**, 793 (2005).

[97] J. D. Smith, C. D. Cappa, B. M. Messer, R. C. Cohen, and R. J. Saykally, Science **308**, 793 (2005).

[98] M. Cavalleri, M. Odelius, D. Nordlund, A. Nilsson, and L. G. M. Pettersson, Phys. Chem. Chem. Phys. **7**, 2854 (2005).

[99] M. Odelius, M. Cavalleri, A. Nilsson, and L. G. M. Pettersson, Phys. Rev. B **73**, 024205 (2006).

[100] M. Iannuzzi, J. Chem. Phys. **128**, 204506 (2008).

[101] W. Chen, X. Wu, and R. Car, Phys. Rev. Lett. **105**, 017802 (2010).

[102] M. Leetmaa, M. Ljungberg, A. Lyubartsev, A. Nilsson, and L. Pettersson, J. Electron Spectrosc. Rel. Phenom. **177**, 135 (2010).

[103] T. T. Fister, K. P. Nagle, F. D. Vila, G. T. Seidler, C. Hamner, J. O. Cross, and J. J. Rehr, Phys. Rev. B **79**, 174117 (2009).

[104] J. Vinson, J. J. Kas, F. D. Vila, J. J. Rehr, and E. L. Shirley, Phys. Rev. B **85**, 045101 (2012).

[105] T. Pylkkänen, V. M. Giordano, J.-C. Chervin, A. Sakko, M. Hakala, J. A. Soininen, K. Hämäläinen, G. Monaco, and S. Huotari, J. Phys. Chem. B **114**, 3804 (2010).

[106] M. Seki, K. Kobayashi, and J. Nakahara, J. Phys. Soc. Japan **50**, 2643 (1981).

[107] W. F. Kuhs, J. L. Finney, C. Vettier, and D. V. Bliss, J. Chem. Phys. **81**, 3612 (1984).

[108] P. H. Hahn, W. G. Schmidt, K. Seino, M. Preuss, F. Bechstedt, and J. Bernholc, Phys. Rev. Lett. **94**, 037404 (2005).

[109] J. S. Tse, D. M. Shaw, D. D. Klug, S. Patchkovskii, G. Vankó, G. Monaco, and M. Krisch, Phys. Rev. Lett. **100**, 095502 (2008).

[110] D. M. Shaw and J. S. Tse, J. Phys.: Condens. Matter **19**, 425211 (2007).

[111] V. Garbuio, M. Cascella, L. Reining, R. D. Sole, and O. Pulci, Phys. Rev. Lett. **97**, 137402 (2006).

[112] Y. S. Badyal, M.-L. Saboungi, D. L. Price, S. D. Shastri, D. R. Haeffner, and A. K. Soper, J. Chem. Phys. **112**, 9206 (2000).

[113] J. J. M. Heller, R. N. Hamm, R. D. Birkhoff, and L. R. Painter, J. Chem. Phys. **60**, 3483 (1974).

[114] A. Nilsson, D. Nordlund, I. Waluyo, N. Huang, H. Ogasawara, S. Kaya, U. Bergmann, L.-Å. Näslund, H. Öström, P. Wernet, et al., J. Electron Spectrosc. Rel. Phenom. **177**, 99 (2010).

[115] C. D. Cappa, J. D. Smith, K. R. Wilson, and R. J. Saykally, J. Phys.: Condens. Matter **20**, 205105 (2008).

[116] P. Glatzel and U. Bergmann, Coordination Chemistry Reviews **249**, 65 (2005).

[117] L. J. P. Ament, M. van Veenendaal, T. P. Devereaux, J. P. Hill, and J. van den Brink, Rev. Mod. Phys. **83**, 705 (2011).

[118] Y. Ma, Phys. Rev. B **49**, 5799 (1994).

[119] F. de Groot, Chemical Reviews **101**, 1779 (2001).

[120] Y. Saad and M. Schultz, SIAM Journal on Scientific and Statistical Computing **7**, 856 (1986).

[121] S. Eisebitt and W. Eberhardt, J. Electron Spectrosc. Rel. Phenom. **110-111**, 335 (2000).

[122] J. J. Kas, J. J. Rehr, J. A. Soininen, and P. Glatzel, Phys. Rev. B **83**, 235114 (2011).

[123] A. V. Sokolov, E. Z. Kurmaev, S. Leitch, A. Moewes, J. Kortus, L. D. Finkelstein, N. A. Skorikov, C. Xiao, and A. Hirose, J. Phys.: Condens. Matter **15**, 2081 (2003).

[124] E. L. Shirley, J. Electron Spectrosc. Rel. Phenom. **110-111**, 305 (2000).

[125] J. A. Carlisle, E. L. Shirley, L. J. Terminello, J. J. Jia, T. A. Callcott, D. L. Ederer, R. C. C. Perera, and F. J. Himpsel, Phys. Rev. B **59**, 7433 (1999).

[126] Y. Ma, N. Wassdahl, P. Skytt, J. Guo, J. Nordgren, P. D. Johnson, J.-E. Rubensson, T. Boske, W. Eberhardt, and S. D. Kevan, Phys. Rev. Lett. **69**, 2598 (1992).

[127] J. de Launay, *Solid State Physics*, vol. 2 (Academic Press, New York, 1856).

[128] J. P. Rueff, Y. Joly, F. Bartolomé, M. Krisch, J. L. Hodeau, L. Marques, M. Mezouar, A. Kaprolat, M. Lorenzen, and F. Sette, J. Phys.: Condens. Matter **14**, 11635 (2002).

[129] J. Jiménez-Mier, J. van Ek, D. L. Ederer, T. A. Callcott, J. J. Jia, J. Carlisle, L. Terminello, A. Asfaw, and R. C. Perera, Phys. Rev. B **59**, 2649 (1999).

[130] P. Glatzel, J. Singh, K. O. Kvashnina, and J. A. van Bokhoven, J. Am. Chem. Soc. **132**, 2555 (2010).

[131] L. Weinhardt, O. Fuchs, E. Umbach, C. Heske, A. Fleszar, W. Hanke, and J. D. Denlinger, Phys. Rev. B **75**, 165207 (2007).

[132] M. Schmidt, M. Grün, S. Petillon, E. Kurtz, and C. Klingshirn, Appl. Phys. Lett. **77**, 85 (2000).

[133] M. Morkel, L. Weinhardt, B. Lohmüller, C. Heske, E. Umbach, W. Riedl, S. Zweigart, and F. Karg, Appl. Phys. Lett. **79**, 4482 (2001).

[134] L. Weinhardt, O. Fuchs, A. Fleszar, M. Bär, M. Blum, M. Weigand, J. D. Denlinger, W. Yang, W. Hanke, E. Umbach, et al., Phys. Rev. B **79**, 165305 (2009).

[135] S.-H. Wei and A. Zunger, Phys. Rev. B **37**, 8958 (1988).

[136] A. Fleszar and W. Hanke, Phys. Rev. B **56**, 12285 (1997).

[137] M. Rohlfing, P. Krüger, and J. Pollmann, Phys. Rev. Lett. **75**, 3489 (1995).

[138] R. Haydock, Comput. Phys. Commun. **20**, 11 (1980).

[139] R. M. Sternheimer, Phys. Rev. **96**, 951 (1954).